A Multi-Point Measurement Technique for the Enhancement of Force Measurement with Active Magnetic Bearings (AMB)

Jeremy T. Marshall

Thesis submitted to the Faculty of the
Virginia Polytechnic Institute and State University
in partial fulfillment of the requirements for the degree of

Master of Science
in
Mechanical Engineering

Dr. Mary Kasarda, Chairman

Dr. Gordon Kirk

Dr. Don Leo

May 8, 2001
Blacksburg, Virginia

Keywords: Multiple Point, Force Measurement, Active Magnetic Bearings

To my father

A Multi-Point Measurement Technique for the Enhancement of
Force Measurement with Active Magnetic Bearings (AMB)

Jeremy T. Marshall

(ABSTRACT)

Active magnetic bearings (AMBs) have the ability to act concurrently as support bearings and as load sensing measurement tools. Previous work in the area of AMB force measurement has relied upon basic magnetic equations requiring knowledge of coil currents and air gap lengths. Some researchers have utilized magnetic flux probes to eliminate the need for air gap measurements, but these are limited by physical size constraints and require complex hardware. This thesis presents a new method for measuring forces with AMBs that utilizes multiple current pairs with no gap measurement to provide accurate and precise force predictions.

Previous methods for force measurement with AMBs rely on the controlled environment of a laboratory setting for accurate measurements. The goal of this work is to develop a robust force measurement procedure for use in industrial and field applications, as well as the laboratory. The harsh environment of a factory floor makes air gap measurements difficult, which limits the use of current-based force equations. Additionally, the flexibility of AMB-equipped thrust measurement systems (TMSs) to measure many types of forces with little to no reconfiguration or calibration makes them appealing.

The multi-point method provides predictions of both shaft force and rotor position using only current pairs without air gap measurements. Static and dynamic load scenarios were investigated to determine the feasibility of this new approach to force measurement. For both, the effects of bearing load and rotor position within the bearing were analyzed. Under dynamic loading, different amounts of unbalance as well as various rotor speeds were used to provide multiple test cases. The multi-point predictions of rotor position were analyzed and compared with the measured rotor positions. It was shown that this new multiple-point method for measuring bearing loads with AMBs provides equivalent or better force predictions to analogous single-point methods for static loads while eliminating the need for measuring rotor position.

ACKNOWLEDGEMENTS

First and foremost, I would like to thank my advisor, Mary Kasarda. Her guidance and advice were irreplaceable during this trying journey. Always ready to make sure that I remained focused on the important details instead of the future problems, she helped me not only finish this degree, but provided several lessons on life as well. I sincerely thank her for all of her help.

To my committee members, I would like express my genuine appreciation for your help and support. Dr. Kirk is an invaluable resource with knowledge to spare and kindness enough to share it. Dr. Leo was always available for assistance when needed, whether for his classes or for equipment. The classes taught by the two of you are among some of the most interesting I have had, and I thank you.

I would also like to thank my mother who is always there for me. Though she often does not understand what it is that I do and kids me about the "piles of money" she feels I will be making, hers is the noblest of professions. The ability to not only save lives, but to brighten them as well is truly a gift.

I would like to thank several fellow and previous students. Hector Mendoza and Josh Clements provided knowledge and assistance when this research was beginning. Eric Blumber and Eric Stasiunas were able to give both fresh opinions and much-needed humor. P. A. Balaji wrote the original version of the program that was used in this research. I must also thank Philip Kedrowski, Ricardo Blackett, Mike Abbott, and the rest of Room 106 for offering a haven for irreverent conversations.

I wish to thank Revolve Magnetic Bearings, Inc. and Bently Nevada Corporation, manufacturers of the equipment used in this research, for their help and assistance.

I would like to acknowledge the National Science Foundation (NSF) for supporting the work presented in this paper under Grant No. DMI-9733124. I would also like to acknowledge NASA Stennis Space Center for their support on this project.

Finally, I would like to thank Heather Ringrose, the most beautiful woman that I know. Your support has made all the difference in the world, and I honestly do not know what I would have done without you. I cannot wait to begin our life together and I hope that as you pursue a graduate degree of your own, I can be half as supportive and amazing as you were for me.

Jeremy T. Marshall

Blacksburg, VA
May, 2001

TABLE OF CONTENTS

LIST OF FIGURES

LIST OF FIGURES

LIST OF FIGURES

LIST OF FIGURES

LIST OF TABLES

LIST OF TABLES

NOMENCLATURE

Symbol	Metric Units	Description
A_g	mm^2	Pole Face Area
b_{exp}	mm	Experimentally Determined Iron Path Length
b_{th}	mm	Equivalent Iron Length
F_{det}	N	Determined Bearing Load
F_{th}	N	Theoretical Force Prediction
g_0	mm	Nominal Radial Air Gap
g_1	mm	Top Air Gap
g_2	mm	Bottom Air Gap
I_1	A	Top Current
I_2	A	Bottom Current
k_{exp}	$N\text{-}mm^2/A^2$	Experimentally Determined Proportionality Constant
k_{th}	$N\text{-}mm^2/A^2$	Proportionality Constant
L_i	mm	Iron Path Length
N	-	Number of Coils
x	mm	Rotor Position
ε	-	Constant Derating Factor
θ_u	° (deg)	Unbalance location for Dynamic Tests
μ_0	H/m (N/A^2)	Magnetic Permeability of Air
μ_r	-	Relative Magnetic Permeability

Chapter 1

Introduction and Literature Review

1.1 General Overview

The Active Magnetic Bearing (AMB) is a device that supports a rotor or structure by levitating it within a magnetic field. There is no physical contact between the bearing and the target and its use in rotating machinery presents many new and attractive possibilities that are not realizable with other types of bearings. This thesis addresses one of the unique capabilities of AMBs that is to act as a support bearing and as a non-invasive shaft force sensor. The goal of this work is to advance the measurement capability of AMBs to facilitate their use in field applications such as in manufacturing equipment and other harsh environments.

Active magnetic bearings are electromagnetic devices requiring several hardware components to operate correctly as shown in Figure 1.1. Since an electromagnet can only produce attractive forces, AMBs are inherently unstable and require closed-loop control for stable operation. As shown in Figure 1.1, the controller monitors rotor position with a position sensor (proximity probe), and when the target position deviates from a desired position, changes in the coil currents are issued by the controller through a power amplifier to remedy the anomaly.

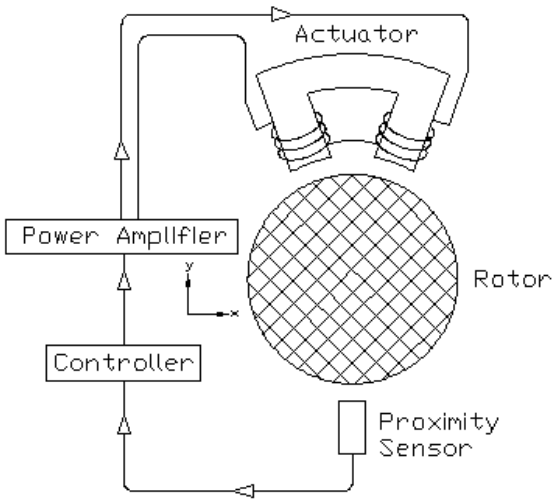

Figure 1.1: Required components for magnetic levitation

The feedback nature of AMBs creates opportunities for the machine designer that are unavailable with the use of conventional bearings. For example, active vibration control is also possible with AMBs. Hope, et. al. (1998) showed that by inducing a rotating magnetic field, vibrations could be reduced for either minimizing transmitted force, minimizing shaft vibration, or reducing control efforts. The no-lubrication requirement of AMBs also allow for their use as dampers or actuators in strategic locations along rotors in conjunction with conventional bearings to add additional damping or vibration control (Mendoza, 2000). Another advantage of the feedback nature of the AMB is that it can be used as both a bearing and shaft force sensor. The ability to use AMBs as force-sensing instruments comes from the physics behind their operation.

1.2 Motivation for Force Measurement

One of the most promising applications for AMB technology is their use as non-invasive load cells. Because they are actively controlled, the control currents can be monitored and interpreted to provide a measure of the supported load. This is a very powerful aspect of magnetic bearings and has been used in laboratory environments to measure forces from pump impellers, seals, and fluid-film bearings. A new application is a rocket thrust measurement system (TMS). By assembling an array of AMBs, a sled can

be constrained to measure the thrust from jet engines, rocket engines, or any other propulsion device. This type of device is discussed by Imlach, et. al. (2000). It provides a very flexible foundation that is free from many of the traditional problems associated with using mechanical load cells. These problems include friction and cross coupling between axes. The work presented here has been developed to support the design of a prototype rocket TMS by researchers in the rotor dynamics laboratory.

In addition to the TMS, this work has also been developed to facilitate the force measurement capability of AMBs in industrial applications such as manufacturing scenarios. Kasarda (1999) has addressed the benefits of using AMBs for improved process control. One advantage of this application is that improvements to Statistical Process Control (SPC) can be made by monitoring industrial processes in real-time. This is of particular importance for processes that are difficult to monitor, such as the manufacturing of micro-fibers. Similarly, by observing operating forces within machinery, improved diagnostic information is available for health monitoring purposes. Monitoring the health of machinery in this manner, maintenance can be performed when needed, instead of according to a schedule, resulting in longer and safer production runs.

1.3 Force Measurement

The current methods for using magnetic bearings in force measurement applications are based on magnetic circuit theory models. A common geometry used in AMBs is the actuator shown in Figure 1.2.

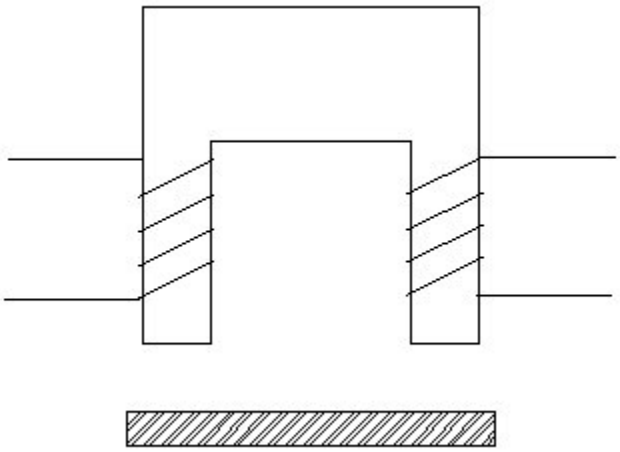

Figure 1.2: Magnetic actuator

By running current through the coils that are wrapped around the legs of the actuator, a magnetic flux is created within the actuator material. This flux is driven around the magnetic circuit that is completed by the target material. When the flux passes through the air gaps to the target material, an attractive force is generated. The magnitude of this force is given by Equation (1.1), and the details of the derivation are presented in Appendix A.

$$F = \frac{\mu_0 A (NI)^2}{4g^2} \tag{1.1}$$

A double-acting magnetic actuator is assembled by positioning two actuators of this type opposing each other on either side of a target, as shown in Figure 1.3. This type of actuator is very important, since it is the basis of most AMB systems. Many AMB systems are assembled with two axes of control that are located 90° apart. This allows the axes to be uncoupled and treated separately as a series of individual actuators. If the control axes are not 90° apart, then the actuators become coupled and the system must be analyzed as a whole instead of axis-by-axis.

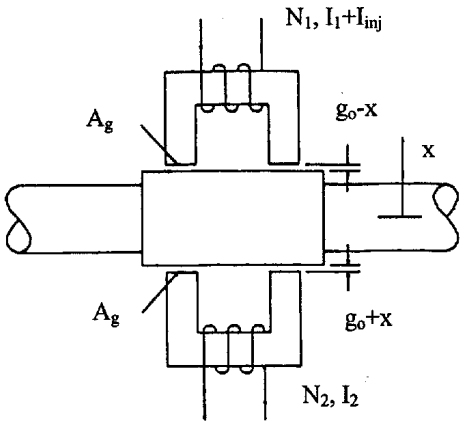

Figure 1.3: Double-acting magnetic actuator

The net force of a double-acting actuator is the difference between the forces produced by the top and bottom magnets. The magnetic flux in each air gap creates an attractive force that varies according to the flux density and the length of the air gap. The most common form of this equation includes an approximation of the magnetic flux based on coil currents, air gap width, and iron path length. Baun, et. al. (1996) present this form of the relationship between force, air gaps and current for a double-acting actuator as

$$F_{th} = \varepsilon \cdot k_{th}\left(\frac{i_1^{\,2}}{(2g_1 + b_{th})^2} - \frac{i_2^{\,2}}{(2g_2 + b_{th})^2}\right) \tag{1.2}$$

where ε is a derating factor, k_{th} is a proportionality constant, i is the coil current, g is the air gap, and b_{th} is the equivalent iron path length of the actuator. The proportionality constant, kth, can be calculated from geometry of the actuator and is given by

$$k_{th} = \mu_0 A_g N^2 \tag{1.3}$$

where μ_0 is the permeability of a vacuum ($4\pi*10^{-7}$ H/m), A_g is the area of a single pole face, and N is the number of coils per actuator. The equivalent iron path length is represented as

$$b_{th} = L_i / \mu_r \tag{1.4}$$

where L_i is an approximation of the mean distance the magnetic flux must travel through the actuator core, and μ_r is an approximation of the relative permeability of the magnetic material. Neither of these two quantities is known with great accuracy. The mean magnetic path length, L_i, is an assumption based on bearing geometry, because the true distance traveled by the magnetic flux cannot be measured. The permeability of the magnetic material, μ_r, is generally based on manufacturer's specifications. However, this material property is variable and dependent on several parameters such as temperature and flux density. In particular, if the saturation level of the material is reached, this value becomes invalid.

The current-based force calculation of Equation (1.2) is relatively simple to implement, but has several drawbacks. One problem stems from the overly simplified model that is used as the basis for this technique. While the idea of magnetic bearings is a straightforward one, there are complex phenomena occurring within them that are difficult to model. These include fringing, leakage, hysteresis, and saturation, all of which limit the accuracy of the measured force when using the magnetic circuit model.

The force relationship in Equation (1.2) is based on several important assumptions. The first of which is that all of the magnetic flux in the circuit flows through the air gaps perpendicular to the pole faces. In reality, the flux fringes out in the air gaps as shown in Figure 1.4. This is not always detrimental to the performance of the bearing; in some cases, higher load capacities have been reported because of this effect (Imlach, 2000). These increased force limits result from an effective increase in the pole face area of the actuator. Regardless, the assumption of uniformity in the flux field does not hold. Additionally, not all of the magnetic flux is passed through the pole faces into the rotor. A small portion can leak from one leg of the actuator to another as shown by the heavy dotted lines shown in Figure 1.5. This leakage is detrimental to the load

capacity of the bearing since it wastes energy that is not converted to magnetomotive force.

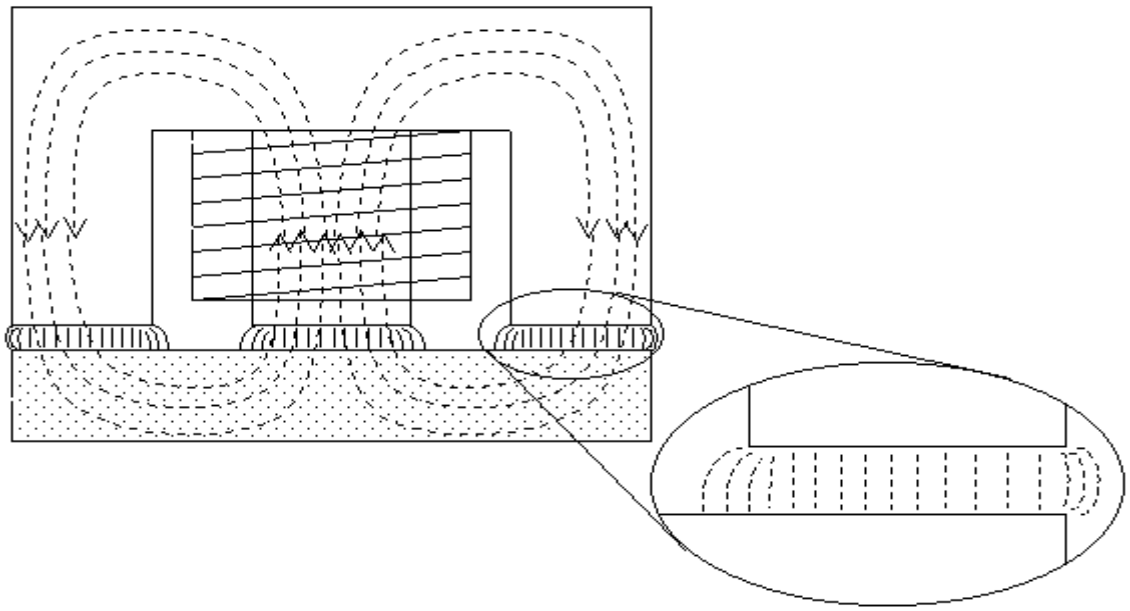

Figure 1.4: Fringing effects in magnetic bearings

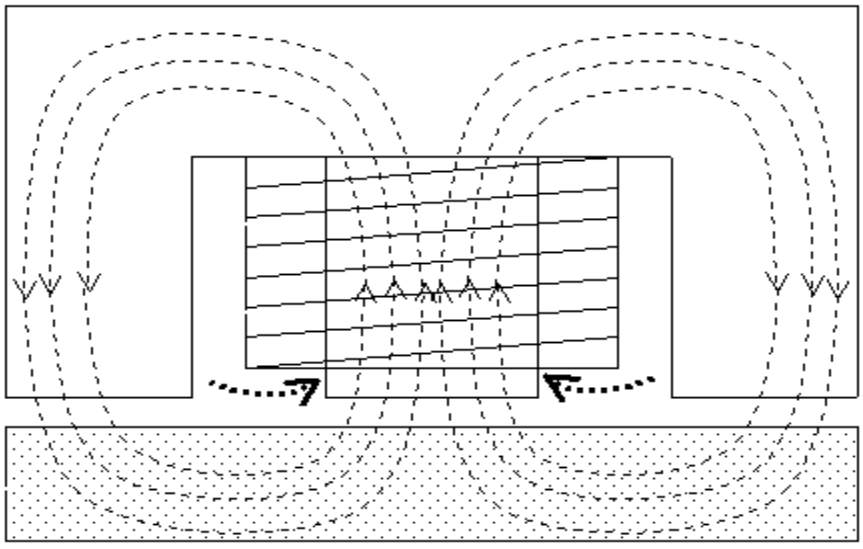

Figure 1.5: Leakage losses in magnetic bearings (heavy dotted lines)

Another effect that is not accounted for in basic applications of this technique is hysteresis. When a magnetic material is first exposed to a magnetic field, the level of

magnetization increases with field strength according to the material's "virgin curve." When the magnetic field is removed, the material will demagnetize along a different curve. If the magnetic field is cycled, a loop is created in the induction versus field strength plot. A typical hysteresis loop is shown in Figure 1.6.

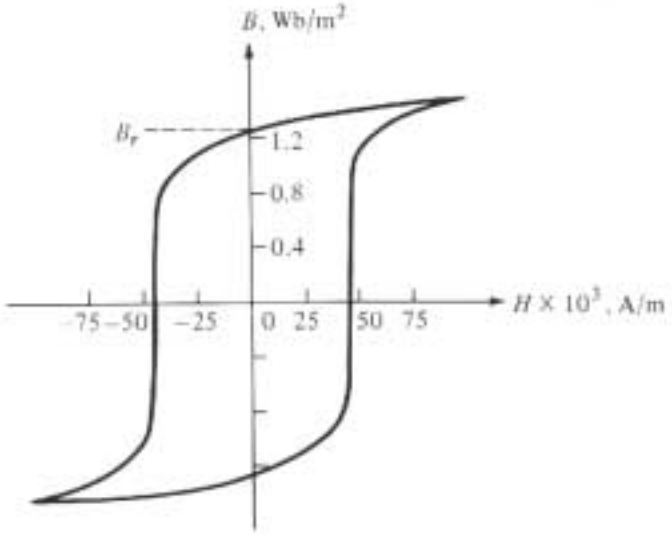

Figure 1.6: Typical hysteresis loop for magnetic material (Plonus, 1978)

There are two types of hysteresis experienced by AMBs that are caused by different conditions as flux changes with respect to time (Kasarda, 1996). The first form is dubbed alternating hysteresis. This occurs when the magnetic field changes cyclically in magnitude and sign. The orientation of the material being magnetized does not change with respect to the magnetic field. The other type is rotational hysteresis. This occurs when a material's orientation within a constant magnetic field is changing. These two types of hysteresis are illustrated in Figure 1.7. There have been models presented that claim to reproduce the hysteresis losses (Springer, 1989), but there is no universally accepted method for handing them at this time.

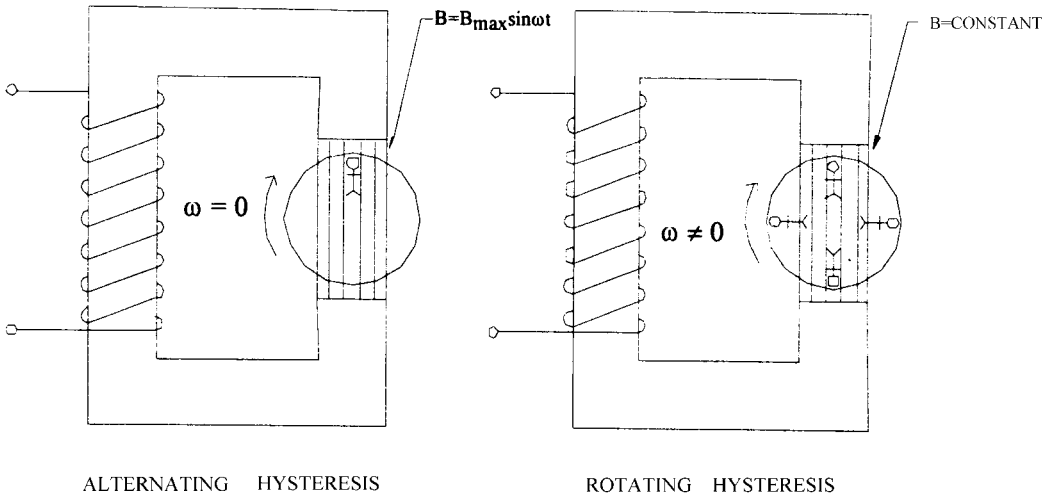

Figure 1.7: Two types of hysteresis: (a) alternating and (b) rotating (Kasarda, 1997)

Another large assumption in Equation (1.2) is the relationship between flux and coil current. Instead of measuring flux directly, a relationship between coil currents, air gap width, and iron path length is used to predict the amount of flux present in the circuit. As stated above, some flux is lost through fringing and leakage, but there is also an upper limit on the amount of possible flux due to saturation of the core material. When a magnetic material is exposed to a magnetic field, the induced level of magnetization increases linearly. However, above a certain point, the curve rolls off, and additional input does not result in as much induced magnetism. If the field is further increased, very little increase in the magnetic flux is achieved. Most AMB systems are designed to remain in the linear region of the B-H curve and not enter the non-linear portions.

Another non-linearity associated with magnetic bearings is due to eddy currents. The main effect of eddy currents is to shield the rotor material from the applied flux, resulting in a reduced flux level in the center of the lamination. This is called a skin effect and is usually seen at high rotational speeds. While these are a large problem in

solid-core actuators, the use of laminated cores and rotors in modern designs has significantly reduced the problem of eddy currents (Springer, 1989).

The derating factor, ε, is typically used as an all-purpose correction term. All of the previous uncertainties are lumped into this single factor and it is determined by calibration. However, many of the effects that it is accounting for are variable and a constant multiplier is insufficient.

Once values for ε, kth, and bth are chosen for the model in Equation (1.2), the only unknowns are the currents, i_1 and i_2; and the air gaps, g_1 and g_2. This is the most common method for measuring forces with AMBs. However, because the inside diameter of the bearing stator is known as well as the outside diameter of the rotor, a substitution can be made where the two unknown air gaps are replaced with Equations (1.5) and (1.6). The nominal radial clearance within the bearing is g_0 and x is the distance of the shaft center from the bearing centerline. If x is zero, the rotor, or target, is centered within the actuator.

$$g_1 = g_0 - x \tag{1.5}$$

$$g_2 = g_0 + x \tag{1.6}$$

After the substitution, Equation (1.2) can be rewritten as Equation (1.7).

$$F_{th} = \varepsilon \cdot k_{th}\left(\frac{{i_1}^2}{\left(2\left(g_0 - x\right) + b_{th}\right)^2} - \frac{{i_2}^2}{\left(2\left(g_0 + x\right) + b_{th}\right)^2} \right) \tag{1.7}$$

Equation (1.7) now gives the applied force of the bearing in terms of i_1, i_2, and x. If the bearing geometry is known, and the coil currents and shaft position are measured, an estimate of bearing force can be determined.

1.4 Literature Review

Considerable work has been performed in the area of force measurement with AMBs. The different techniques for achieving this have been applied for various applications, and with varying success.

Traditionally, AMBs have been used in laboratory settings to measure forces from propulsion devices, seals, and bearings. By monitoring the bearing forces due to a compressor impeller, important information on generated forces and flow characteristics can be obtained in regards to the operation of the impeller that is otherwise extremely difficult to acquire (Guinzburg and Buse, 1994, Guinzburg and Buse, 1995, Baun and Flack, 1999). Previous methods used either strain measurements or pressure taps in the compressor shroud.

Guizburg and Buse (1994, 1995) detail the use of magnetic bearings for the measurement of impeller loads on centrifugal pumps. The forces and moments due to hydrodynamic effects were analyzed by a test rig utilizing magnetic bearings (1994). The impeller was mounted on the rig's main shaft, which was levitated by three magnetic bearings, two for radial loads and one for axial loads. The steady loads from centrifugal pump impellers were then addressed via the same test rig (1995). The force predictions were generated by using a form of Equation (1.2) that is given by

$$F = \mu_0 c_g A_g N^2 \left[\left(\frac{i_A}{c_A} \right)^2 - \left(\frac{i_B}{c_B} \right)^2 \right] \tag{1.8}$$

where μ_0, Ag, and N follow the standard definitions, c_g is the geometric correction factor, i_A and i_B are the top and bottom actuator currents, and c_A and c_B are the top and bottom effective air gaps. The value used for the geometric correction factor was not given in the documentation. To test the accuracy of the bearings, Guinzburg (1995) used a static calibration test procedure that included a hysteresis test (increasing and decreasing quasi-static forces), and calibration errors of five to ten percent were found. This is a typical

application of a single-point technique for using magnetic bearings for force measurement. The authors acknowledge that non-collocation errors are present, but accounted for. The calibration procedure for this test is used to perform a bearing bias force correction and an offset calibration, and is performed at the beginning of each test. This type of calibration procedure would be difficult to implement in a field application where the application of known loads could prove difficult. The constant geometric correction factor cannot account for position-dependent effects such as fringing either.

Baun and Flack (1999) describe a similar test rig for measuring the radial and axial forces from a centrifugal pump impeller. The pump housing for Baun's test rig was constructed of Plexiglas to facilitate laser velocimetry measurements for flow visualization. The actual impeller rotor was suspended in three radial magnetic bearings with maximum load capacity of 89 N (20 lbf), and a single magnetic thrust bearing capable of providing 185 N (42 lbf). Baun and Flack used the magnetic force relationship presented earlier as Equation (1.2) for the axial thrust bearing. The derating factor used was 1.0. For the radial bearings, a matrix approach was used for the calculation of bearing loads. A description of this method is given by Fittro, et. al. (1997), which is summarized below.

$$F_{th} = \varepsilon \cdot k_{th}\left(\frac{{i_1}^2}{(2g_1 + b_{th})^2} - \frac{{i_2}^2}{(2g_2 + b_{th})^2} \right) \tag{1.2}$$

The theoretical values for k_{th} and b_{th} were determined using Equations (1.3) and (1.4), but a static calibration was performed on the test rig to determine the experimental values of k_{exp} and b_{exp}. The optimal values were those that minimized the root-mean-squared error between the predicted force and the actual force as measured by a load cell in the calibration assembly. The calibration was performed outside of the test rig, on a special calibration apparatus. For the axial thrust bearing, the root-mean-squared error was minimized to 2.31 N (0.52 lbf), and the calibration relationship was found to be linear for air gap variations of ±0.38 mm (±0.015 in) and for force levels of 291 N (65 lbf). For the radial bearings, the calibration relationship was linear for air gap variations

of 0.356 mm (0.014 in) and for force levels up to 57.8 N (13 lbf). The minimized root-mean-squared error was 0.756 N (0.17 lbf). A hysteresis analysis was performed to determine whether the loading and unloading of the actuators would affect the force predictions. For a force loop of ±33.4 N (±7.5 lbf), the net coercive force was found to be 0.34 N (0.075 lbf). This error was less than the static calibration error and neglected throughout the remainder of the test.

Fittro, et. al. (1997) detail the calibration of an 8-pole planar radial AMB. In particular, a new method for calculating bearing loads using a fully coupled matrix force model is presented. By forming magnetic circuit loop and node equations, as in electric circuit theory, the magnetic flux in the entire actuator can be represented by a matrix equation. The magnetic fluxes can then be approximated by another matrix equation in terms of currents and air gaps. The combination of the two equations provides a means to predict AMB shaft loads. This is a novel way of assembling the traditional single-point force equations such as Equation (1.2) to couple the entire set. The percent errors of a static calibration were normally distributed with a mean of 1.04% and a standard deviation of 3.69%. The root-mean-squared error between the experimental measurements and theoretical predictions was minimized to 0.17 lbf.

Wagner and Steff (1998) assembled a test rig to simulate a high-pressure turbo compressor in order to determine labyrinth seal stiffness and damping values. These coefficients are of vital importance when designing and analyzing industrial compressors as they influence the stability of the machinery. In order to accurately reproduce the operating conditions of an actual compressor, AMBs were employed. These allow eccentricities to be applied to the rotor, as well as vibrations of any frequency or amplitude. The magnetic bearings also enable the rotor forces to be measured directly, instead of using indirect measurements from bearing stators. The test stand consisted of a gear-driven compressor supported on AMBs. Labyrinth seals of different varieties were used to analyze the effects caused by these differences.

The shaft forces were measured by the AMBs using Equation (1.1). A complex linearization was performed about an equilibrium operating point resulting in Equation (1.9), where F_0, k_s, and k_q are calculated constants, and x' and i' are displaced values from the static equilibrium state. After several conversions, a second-order differential equation remains, which is where the labyrinth seal coefficients are introduced. By analyzing frequency plots of the real and imaginary components of the differential equation's complex variable, the labyrinth seal stiffness and damping coefficients can be determined by a linear regression. No comparative data was given to quantify the accuracy of this technique, but the expected trends were observed for the various types of seals. This is an application for AMB technology that would not be possible without the ability to generate realistic operating conditions and concurrently measure the rotor response.

$$F = \frac{\mu_0 A (NI)^2}{4g^2} \tag{1.1}$$

$$F = F_0 + k_s x' + k_q i' \tag{1.9}$$

Several papers have been written outlining improvements to the force equation's derating factor. The derating factor is simply a scale multiplier for the force relationship in Equation (1.2). The purpose of using these factors is to try and account for the many different effects that cause force measurement errors. Historically, the value of the correction factor has been determined by means of laboratory calibration procedures. Baun, et. al. (1996) provides documentation on the calibration of a double-acting magnetic thrust bearing. By using a specialized fixture outside of the testing apparatus, the AMB and rotor are suspended in a fashion that allows the rotor forces to be measured. By varying the magnetic flux and measuring the force created, a large data set was created. Using this data set, the model of Equation (1.2) can be fit to the data to determine k_{exp} and b_{exp}. The correction factor, ε, can then be found using Equation (1.10).

$$F_{th} = \varepsilon \cdot k_{th} \left(\frac{{i_1}^2}{(2g_1 + b_{th})^2} - \frac{{i_2}^2}{(2g_2 + b_{th})^2} \right) \tag{1.2}$$

$$\varepsilon = \frac{k_{\exp}}{k_{th}} \tag{1.10}$$

The observed value of b_{exp} can be used to gain information on the true permeability of the core material. The percent errors that were observed with this test rig were normally distributed with a mean of –0.226%, and a standard deviation of 7.8%.

While this method works well in a laboratory environment, there are problems that limit its usefulness in an industrial scenario. By removing the bearing for calibration outside of the original machinery, several inconsistencies can arise. The most detrimental would be problems with reassembly after the calibration. If there were geometry changes due to assembly procedures, such as misalignments, when the AMB is replaced in the machine, the calibration is potentially no longer valid. A second difference that could arise between a laboratory calibration and reinstallation is a change in ambient conditions. It is unlikely that the controlled environment of a laboratory could be maintained in a factory setting. Temperature changes may invalidate the calibration procedures and cannot be accounted for with a constant correction factor.

Another problem associated with the constant correction factor is its inability to account for position-variant effects. Imlach (2000) presents a fringing model that relates a variable correction factor to the ratio of bearing air gaps and actuator width for a planar "E-core" magnetic bearing. As the target moves relative to the magnetic actuator, the amount of fringing as shown in Figure 1.3 changes, resulting in varying correction factors. The function used to describe the position dependency of the derating factor is a compound exponential, with three parameters used to tune the model. The factor calculated by this model is representative of ε, the derating factor, in Equation (1.2). This technique has been verified using Magnetic Finite Element Analysis (MFEA) and works very well. This validation was performed by two groups of researchers. One group

performed the MFEA analysis using various loads and air gaps. The coil currents generated in the MFEA analysis were then given to the second group of researchers who used them with an AMB model that included the fringing model to predict the forces and displacements used originally. Percent errors of less than 0.1% were observed for both the predicted forces and displacements. More details of this procedure may be found in Section 2.3. Experimental results are not yet available to further validate this technique.

Another area of research involves the use of flux sensors. As explained above, using an approximation to predict flux levels within a magnetic bearing is difficult at best. Equation (1.1) shows the force equation for a single magnetic actuator when using current measurements. In addition to a current measurement, an accurate measurement of the air gap is required. This is difficult because due to space constraints, it is extremely difficult to collocate the proximity probes and actuator, which can lead to non-collocation errors. A single plane of proximity probes is also insufficient to determine rotor misalignment, which can become problematic with small, flexible rotors. The combination of the air gap measurements typically being very small and being squared in the denominator of Equation (1.1) means that small position measurement errors can lead to large force errors.

$$F = \frac{\mu_0 A (NI)^2}{4g^2} \tag{1.1}$$

By using Hall-effect flux probes, the force equation can be simplified greatly. Using Equation (1.11), only the magnetic flux measurement and the pole face area is required to predict the actuator force.

$$F = \frac{\phi^2}{\mu_0 A_g} \tag{1.11}$$

Another benefit is that by measuring the flux directly, non-linearities such as saturation (in the amplifiers and magnetic material) are avoided. Material saturation

results when the linear region of the hysteresis curve is exceeded. Amplifier saturation can be avoided by choosing suitable electronics, but by using the flux probes, this potential problem is eliminated.

This is the approach taken by Knopf and Nordmann (1998) in their magnetically levitated test rig to measure the dynamic effect of fluid-film bearings. Their test rig utilized an eight-pole radial bearing with two poles per quadrant. Under each pole leg, a Hall-effect flux sensor was positioned to directly measure the magnetic flux passing through the pole leg. Equation (1.12) gives the new force relationship for the F_0 axis when flux probes are used. By implementing Hall effect probes in the air gap of each AMB to measure the magnetic flux, errors on the order of 1% were reported. For comparison, calibration errors in Guinzburg and Buse's (1995) test rig were on the order of 5-10%.

$$F_0 = \frac{1}{\mu_0 A_g} \cdot \begin{bmatrix} \cos \pi/8 \cdot \left(\phi_{0pN}^2 + \phi_{0pS}^2 - \phi_{0nN}^2 - \phi_{0nS}^2 \right) + \\ \sin \pi/8 \cdot \left(\phi_{1pN}^2 - \phi_{1pS}^2 - \phi_{1nN}^2 + \phi_{1nS}^2 \right) \end{bmatrix} \tag{1.12}$$

Unfortunately, this approach also has its associated problems. Most importantly, the flux probes themselves are extremely delicate and difficult to install and maintain in this application. Because they are placed in the actuator air gaps, the physical size of the Hall sensors must be very small. The air gaps may also have to be increased to accommodate the probes in order to maintain a minimum clearance, which lowers the maximum force capability of a given bearing geometry. Additionally, each probe requires a dedicated circuit in order to operate. Unlike most sensors, such as proximity and velocity probes that require a voltage source, flux probes are current-driven devices. Presently, canned circuitry for flux probes is not readily available. The problem of fringing and leakage is not accounted for with this technique either. Fringing causes a change in the effective pole face area, which would necessitate a derating factor to maintain the accuracy of the force predictions. Leakage would further reduce the amount of flux that passes through the target and is used for levitation.

1.5 Multi-Point Method

The previous sections described the state of the art applications and techniques for using AMBs for force measurement. The subject of this project is the development of a new method for measuring force with magnetic bearings. This technique is a modification of the previously mentioned forms and utilizes the AMB feedback system to perturb the rotor for additional system information to improve force measurement techniques. A series of current sets (multiple points) are recorded and analyzed to arrive at a prediction of the bearing loads. The derivation of the method is presented in this thesis as well as the theoretical and experimental validation of the technique. The developed multi-point method is a robust force measurement technique, particularly useful for harsh environments and field applications with less controllable environments than laboratory scenarios. It allows for prediction of both shaft forces and rotor position with information from coil currents only.

Chapter 2

The Multi-Point Methodology

2.1 Introduction

Researchers have made significant contributions to improving the force measurement capabilities of magnetic bearings as described in Chapter 1. However, limitations with utilizing AMBs for force measurement still exist, particularly reliable air gap estimations and system calibration. This is particularly true for scenarios outside of the laboratory where equipment and environments are not easily controlled and/or monitored, such as in manufacturing and other field applications. To facilitate the use of AMBs for force measurements in these types of scenarios as well as in the laboratory, a new methodology has been developed which takes advantage of the AMB feedback system to keep a rotor in a fixed inertial location under varying conditions. This methodology, referred to as the multi-point method, is loosely based on rotor balancing techniques and was developed as a means for on-line calibration of a magnetic bearing used for force measurement. The method has also proven useful for taking actual force measurements. It determines a rotor position and shaft force by examining the system's response to multiple force perturbations achieved by applying incremental current increases to one side of a bearing actuator.

2.2 Procedure

The calibration routine of interest was believed to be analogous to traditional system identification of rotating machinery. A common method for characterizing the dynamic state of rotating machinery systems is the influence coefficient technique, which is often used in balancing. It entails measuring a desired quantity, such as vibration

amplitude and phase, under normal operating conditions. After creating a small force perturbation by adding a balance weight to the rotor, an additional measurement of vibration amplitude and phase is taken. By comparing the two values and observing the difference due to the perturbation, a coefficient can be assigned to the perturbation that quantifies the influence of a given balance weight on the dynamic response of the rotor.

This approach was extended in order to identify the variable characteristics of AMBs for use in force measurement equations. However, instead of using balance weights, perturbation currents are used to perturb the system in the AMB calibration scenario. By analyzing how the control algorithm responds in order to maintain the rotor's position, the true force being applied to the rotor as well as the rotor position can be calculated. This ideally allows the user to determine system parameters in the actual system at any time in order to perform accurate force measurements.

The procedure for perturbing the system consists of a series of current injections, followed by a measurement of the system response. Based on the initial settings of gains and bias currents, the controller will levitate the target or rotor at a fixed inertial location in space with distinct top and bottom currents. These are recorded as the first current pair. If the current in the top actuator is modified by the addition of an injected current, I_{inj}, the controller will increase the current in the lower actuator to balance the additional force created by the extra current, which creates a second current pair. The multi-point method was developed for a single-axis double-acting magnetic actuator, as shown in Figure 2.1. It also shows the injected current into one actuator and the different current in the opposing actuator that results from the injection. The ability of AMBs to maintain rotor position is exploited in this operation to keep the rotor at a single location while generating the current pairs. In other words, this new current pair is different from the original, but the bearing is supporting the same load in the same inertial position. This procedure can be repeated several times to obtain a set of current pairs. The set of generated current pairs is then used in an algorithm that determines rotor location and the supported force as described in the next section.

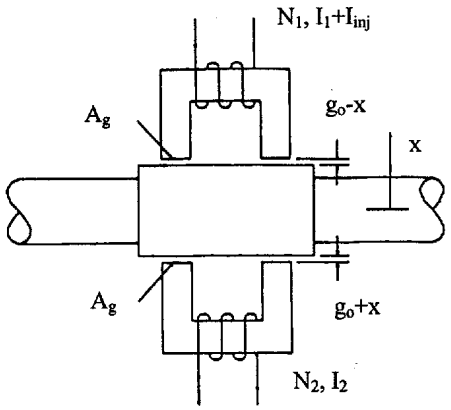

Figure 2.1: Double-acting magnetic actuator

2.2.1 Multi-Point Algorithm

The recorded current pairs are utilized in the multi-point algorithm to generate a matrix of possible forces. The first step in the algorithm is to form a vector of potential rotor locations. There is a limited range of positions that the rotor can occupy because it is bounded physically by the actuator stators. The vector entries are defined as displacements from the true bearing centerline, so that the extremes of these movements are $\pm g_0$. The quantity g_0 is the radial clearance of the bearing, or half of the difference between the stator inner diameter and the rotor outer diameter. The rotor can only physically move this distance, g_0, before it contacts one or the other actuators. This total range of possible displacements is broken down into discrete steps, defined by the step size, Δx. The vector is of the form

$$\mathbf{x} = \begin{bmatrix} -g_o \\ -g_o + \Delta x \\ -g_o + 2\Delta x \\ \vdots \\ -g_o + (m-1)\Delta x \\ -g_o + m\Delta x \end{bmatrix} = \begin{bmatrix} -g_o \\ -g_o + \Delta x \\ -g_o + 2\Delta x \\ \vdots \\ g_o - \Delta x \\ g_o \end{bmatrix} \tag{2.1}$$

where m is defined by the relationship

$$m = \frac{2g_0}{\Delta x} \tag{2.2}$$

and where

$$-g_0 + \frac{m}{2}\Delta x = -g_0 + \frac{g_0}{\Delta x}\Delta x = 0 \tag{2.3}$$

represents the "centered" rotor position. Either the number of discrete rotor locations (m+1) or the size of the increments (Δx) can be specified, but the two are related by Equation (2.2). This step defines a vector of discrete potential physical locations of the rotor in the range of $\pm g_0$.

Once the potential location vector, **x**, is determined, the matrix of forces is assembled. This matrix represents the force associated with a given current pair at each potential rotor location, as listed in the vector **x**. For each current pair, a force is calculated at each of the possible rotor locations listed in **x** based on Equation (1.7).

$$F_{th} = \varepsilon \cdot k_{th}\left(\frac{i_1^{\,2}}{(2(g_0 - x) + b_{th})^2} - \frac{i_2^{\,2}}{(2(g_0 + x) + b_{th})^2}\right) \tag{1.7}$$

The force matrix, F, is of the form shown in Equation (2.4).

$$F_{x,I1,I2} = \begin{bmatrix} F(-g_0; I_{10}, I_{20}) & \dots & F(-g_0; I_{1n}, I_{2n}) \\ F(-g_0 + \Delta x; I_{10}, I_{20}) & \dots & F(-g_0 + \Delta x; I_{1n}, I_{2n}) \\ \vdots & \ddots & \vdots \\ F(-g_0 + m\Delta x; I_{10}, I_{20}) & \dots & F(-g_0 + m\Delta x; I_{1n}, I_{2n}) \end{bmatrix} \tag{2.4}$$

The force matrix will have the same number of columns as current pairs, and the rows will correspond to the rows in **x**, the vector of possible displacements. This matrix,

physically, defines the possible forces due to the measured current pairs at the chosen possible rotor positions within the bearing. The next step of the procedure is to analyze these possible bearing loads and determine which corresponds to the actual force.

After the force matrix, Equation 2.4, has been generated, the final step is to determine which of the calculated forces the bearing is actually experiencing. Since each row of the matrix represents a discrete physical rotor displacement, a row-by-row comparison is conducted to determine which is the actual force. Theoretically, the row where the forces exactly match across all of the current pair cases represents the physically actual rotor position and the actual shaft force. Since only a finite number of locations are used, it is likely the calculated forces will only agree within a certain amount. If the standard deviation of each row is calculated, this will report the amount of spread in the predicted forces. The row with the minimum standard deviation provides the closest match and represents the actual bearing force. The corresponding row in the vector of locations, **x**, represents the actual rotor position. By increasing the size of this vector (reducing the step size), the accuracy of this procedure can be increased. These are the predictions for bearing force and rotor position that are calculated by the multi-point method.

The development of the procedure into a workable computer code was completed by two other researchers, M. Kasarda and P. A. Balaji, and further refined by the author. The source code used for the calculations was developed in MATLAB and is presented in Appendix B.

To summarize, the procedure is as follows:

- The magnetic actuator is perturbed with an injection current, and several current pairs are generated and recorded,
- The vector of possible rotor locations within the mechanical limits of the stator are determined (as the size of this vector increases, more discrete locations are possible and the accuracy of this method increases),

- Possible forces are calculated for each discrete rotor location and current pair to generate the force matrix,
- The force matrix is analyzed to find the discrete rotor location with minimum variation in the predicted forces to determine the physically realizable system.

2.3 Magnetic FEA Validation

The multi-point methodology for force measurement was initially verified using Magnetic Finite Element Analysis (MFEA). The MFEA validation work was completed by J. Imlach of Imlach Consulting Engineering as presented in Imlach (2000). A MFEA model was used to generate different loading and target location scenarios to test the multi-point algorithm's ability to predict accurate force and gap values. The MFEA model used in the validation was a double-acting actuator of the "E-core" variety as seen in Figure 2.2. The bearing was of the planar thrust type, and was used as a first step at checking the validity of the calibration procedure. This geometry also represents the actuators used on another parallel project at Virginia Tech to develop a rocket thrust measurement system.

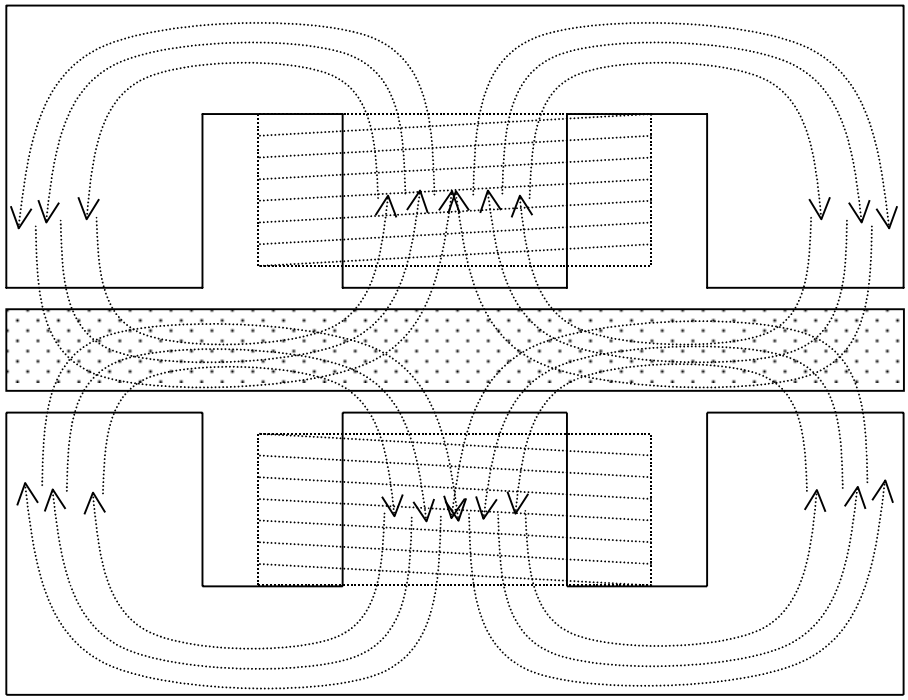

Figure 2.2: AMB with E-Core Geometry

In order to test the multi-point technique, several data points were generated with MFEA where both the air gap in the actuator and the applied force were varied. The applied loads were purely static and dynamic effects were not investigated. For each set of force and target location, current "injections" were simulated in the MFEA models to generate sets of current pairs for each combination. Because of the purely theoretical nature of this MFEA validation, the geometry of the bearing and the magnetic permeability of the rotor and stator material were known exactly. Additionally, there was no misalignment between the rotor and stator. The elimination of uncertainties such as this allowed Equation (1.7) to be used with considerable confidence because all of the variables were known. Once the MFEA force and position combinations were completed along with current pairs for each case, the multi-point algorithm was employed in an attempt to predict the original MFEA conditions. Equation (1.7) was used in the algorithm to calculate the bearing forces. The derating factor, ε, which was used in Equation (1.7) for the MFEA validation tests was not a constant value. The fringing model developed by Imlach (2000) and described in Section 1.4 was used for the derating factor.

$$F_{th} = \varepsilon \cdot k_{th}\left(\frac{i_1^{\,2}}{\left(2(g_0 - x) + b_{th}\right)^2} - \frac{i_2^{\,2}}{\left(2(g_0 + x) + b_{th}\right)^2} \right) \tag{1.7}$$

Results of the MFEA validation tests are shown in Table 2.1. Column one gives the test number of each case, while the nominal gap measurement is given in column two. The forces and rotor locations used in the MFEA generation are shown in the third and fourth columns of Table 2.1. The actual gaps for the MFEA trials can be found by adding and subtracting the target position, x, from the nominal gap, g_0 ($g_1=g_0+x$, $g_2=g_0-x$). The fifth and sixth columns present the algorithm-predicted values for force and target location. The multi-point predicted target locations are relative to the true bearing centerline, or the position where all of the actuator air gaps are equal. This is assumed in the definition of the gaps, as shown in Equation (1.5) and (1.6). The final two columns show the percent errors between the predicted and the actual values. Using only bearing

geometry and coil currents, the multi-point algorithm was able to predict the applied force and target displacement with percent errors less then 0.1%. The maximum percentage errors for the force and displacement predictions were -0.07% and 0.08%, respectively.

Table 2.1: Comparison of MFEA Generated Data and Algorithm-Predicted Values

	g_0	MFEA Data		Predicted Data		% Error	
Set #	(mm)	Force (N)	x (mm)	Force (N)	x (mm)	Force	x
1	10.0	0.00	2.00	1.24	1.992	0.03	-0.08
2	10.0	-300.00	2.08	-301.10	2.084	-0.02	0.04
3	10.0	215.00	-5.05	217.34	-5.052	0.05	-0.02
4	4.0	-50.00	0.05	-53.50	0.051	-0.07	0.03
5	4.0	10.00	-1.00	10.63	-1.000	0.01	0.00

The percentage error values are based on full-scale actuator force and displacement, 5000 N and 10.0 mm, respectively, for sets 1-3, and 5000 N and 4.0 mm, respectively, for sets 4 and 5. Basing percent errors on full-scale values is the accepted method for rocket thrust measurement systems.

Although the multi-point method uses only bearing geometry and the current pairs, these good results were potentially due to the well-defined nature of MFEA. As stated above, there were minimum uncertainties in any part of this test. All physical and magnetic properties were known, and effects such as fringing and leakage followed the theoretical models built into the MFEA code. The results demonstrated that for a simple actuator geometry, the multi-point calibration method performs very well. The next step was to conduct experimental tests to determine if it would perform as well with actual actuators.

Chapter 3

Experimental Description

3.1 General Components

Once the MFEA validation was completed, the experimental tests were planned and conducted. Three rotor configurations were used to test the capabilities of the multi-point approach to force measurement. Two of the configurations produced only static loads, and the third generated dynamic forces. All three configurations used the same instrumentation and support hardware despite the differences in rotor arrangement. The common equipment can be arranged into four categories: the rotor kit, magnetic actuators and control, data acquisition, and post-processing.

3.1.1 Rotor Assembly

The basic components of the rotor assembly that were used in all of the configurations are a shaft, disk masses, motor with speed control (disconnected for first two static tests), proximity measurement probes and their associated conditioners. The shaft measures 9.525 mm (3/8 in) in diameter and is constructed of steel. The length of the shaft measures 457.2 mm (18.0 in) long. The disk masses are made of steel, and have varying weights. Each of them has 16 tapped holes equally spaced along its perimeter for balancing purposes. The motor used in the dynamic testing was rated at 1/10 hp and for speeds up to 10000 RPM. A motor controller regulated the motor's speed and also included ramp rate control (how fast the motor accelerated). An RK 4 Proximitor Assembly powers the eddy current proximity probes, which then send the signals to a TK 21 Oscilloscope Interface to AC-couple the signals. The output of the TK 21 was directed to the data acquisition I/O board discussed below.

3.1.2 Magnetic Actuators and Control

Revolve Magnetic Bearings, Inc manufactured the magnetic bearings, controller, interface software, and associated hardware and marketed the package as MBRetro. The AMBs used in the experiment utilized an 8-pole radial heteropolar design. A picture of one of the radial magnetic bearings is given in Figure 3.1 and the design specifications are given in Table 3.1. Each bearing provides actuation in two perpendicular axes, which are rotated 45° from vertical as shown in Figure 3.2. The AMBs required the use of bearing rotors that clamp securely onto the rotor kit shaft. Each of the rotors weighed 262 g (0.578 lbf).

Figure 3.1: Picture of radial AMB

Table 3.1: Design specifications for radial magnetic bearings

Bearing Specification	**Metric Units**	**English Units**
Static Load Capacity	53 N	12 lbf
Saturation Current	3.0 A	
Number of Poles per Quadrant	2	
Stator Stack Length	12.700 mm	0.500 in
Stator OD	70.822 mm	2.788 in
Stator ID	35.052 mm	1.380 in
Rotor OD	34.290 mm	1.350 in
Nominal Air Gap	0.381 mm	0.015 in
Pole Face Area	66.019 mm^2	0.10267 in^2
Pole Centerline Angle	0.394 rad	22.5°
Stator Material Grade	M-19, C-5	
Rotor Material Grade	Arnon 5, C-5	
Relative Magnetic Permeability, μ_r	3000	
Proportionality Constant, k_{th}	4.313 N mm^2/A^2	0.001502 lbf in^2/A^2
Equivalent Iron Path Length, b_{th}	0.02709 mm	0.001067 in

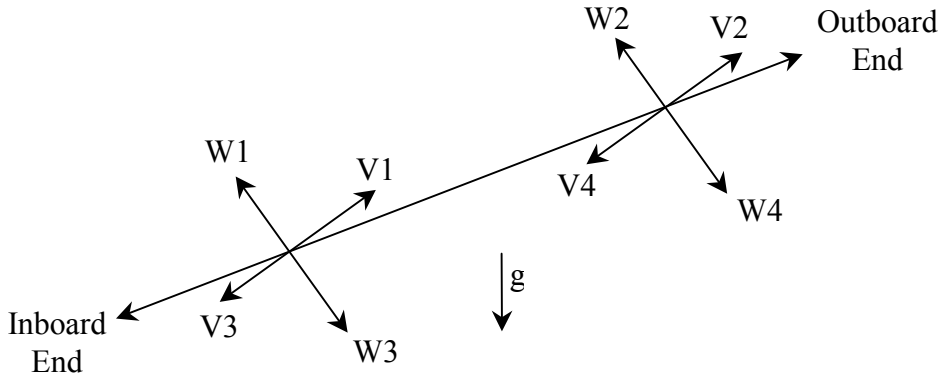

Figure 3.2: Orientation of AMB axes

Position feedback to the controller was provided by variable reluctance proximity probes that are mounted within the bearing housing along the same axes as the actuators. The position information from these probes was used only for control purposes and was not recorded.

The Revolve MB350 controller was used with MBScope software and the optional MBResearch BNC breakout box. The MB350 controller provides five axes of control, two for each radial bearing and one for the optional thrust bearing. The thrust

option was not exercised in this investigation. The controller type is digital Proportional-Integral-Derivative (PID) with a sampling frequency of 10 kHz. The PID control algorithm adds stiffness to the system through the proportional component, damping with the derivative term, and the integral term allows for accurate position control.

The MBScope software suite consists of several programs that communicate directly with the controller for monitoring and modifying values and parameters. The SISOTune program allows for axis-by-axis changes to each of the controller gains (proportional, integral, derivative, and overall), bias currents (top and bottom per axis), position offsets, and assorted filters in order to tune the system. Injection signals are also coordinated with this program. Figure 3.3 shows a screen shot of the SISOTune program and its variables. The Snapshot program displays various controller variables in real-time for visual monitoring. An example of the Snapshot program in use is shown in Figure 3.4. The Parameter Loader allows for the controller settings to be saved and loaded for later use. Other programs perform functions such as setting controller alarm limits and calibration exercises.

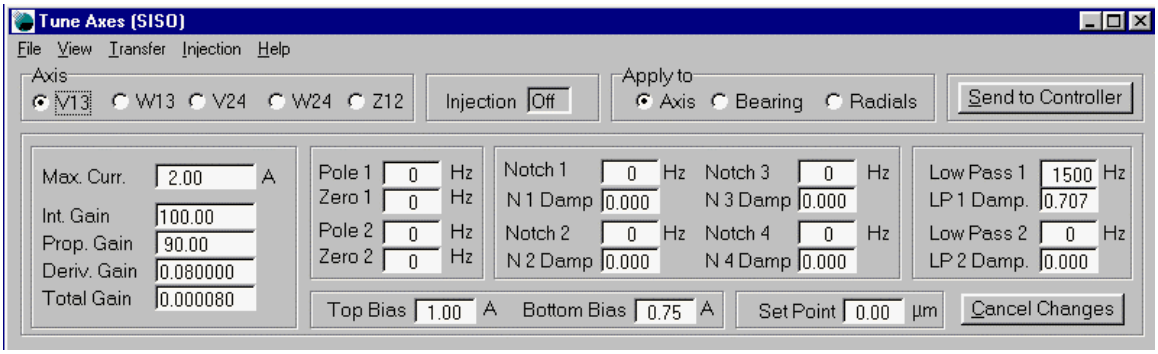

Figure 3.3: Screen capture of SISOTune program

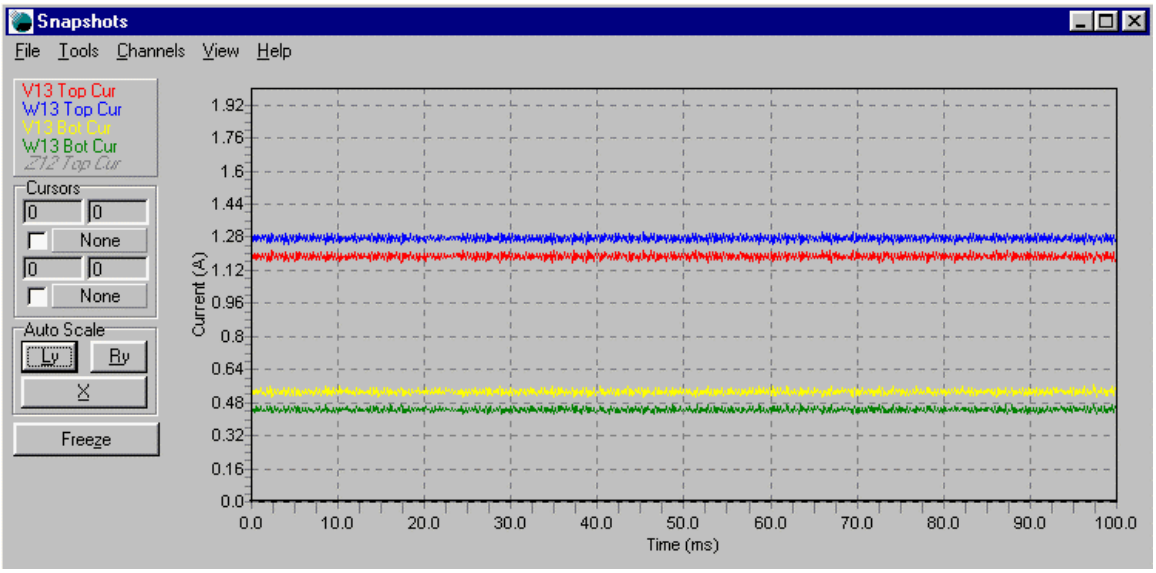

Figure 3.4: Screen capture of Snapshot Program

The MBResearch breakout box interfaces with the controller and provides BNC connections for monitoring any of the controller variables, or for injecting external signals. Although the breakout attachment allowed for easy access to the control currents, position measurements, and a variety of other variables, it was used only for current measurements.

3.1.3 Data Acquisition

For data logging, a National Instruments data acquisition board converted the eight current signals (four current signals per bearing) and the two external proximity probe readings from analog to digital data. LabVIEW software controlled the data acquisition and allowed for different settings according to the particular test being run. LabVIEW also allowed for the recording of the data streams into a file for use by the post-processing programs.

3.1.4 Post-Processing

After LabVIEW saved the data files, the multi-point algorithm was used to analyze them to determine the predicted force and displacements. The multi-point code

was written using MATLAB (presented in Appendix B), and was able to directly import the data files output by LabVIEW.

3.2 Rotor Configurations

For both types of loads, a different rotor setup was required. An external motor was coupled with the shaft to drive the dynamic load case. The two setups for the static cases were non-rotating. The different arrangements also required the use of different controller parameters. The MB350 controller allows for the user to modify the control gains for optimal performance. A description of each rotor setup is given below.

3.2.1 Static Test Setup #1

The first test that was performed consisted of an overhung static load supported on a single magnetic actuator. This arrangement was chosen to isolate one of the bearings and eliminate the difficulty of monitoring both sets of actuators.

In order to isolate a single bearing for study, one bearing was pinned and an overhung loading was used, as shown in Figure 3.5. By using a thin ring of material to shim the rotor within the disabled bearing, an approximate pin joint was created. By summing moments about this pin joint, the bearing load at AMB 13 was calculated. Adding, subtracting, or moving the overhung weights relative to the pivot could generate different loads, which were required to fully test the multi-point theory. Figure 3.6 shows a schematic of the rotor layout. The bearing span between where the 2-4 bearing was shimmed and the center of the 13 bearing was 226.7 mm (10.5 inch). Several combinations of masses were loaded onto the overhung end of the shaft in order to load the bearings in differing amounts from 16.73 N (3.76 lbf) up to 48.49 N (10.90 lbf). This configuration tested a wide range of the AMB's capabilities (31.73 N (7.14 lbf) out of a maximum range of 53.4 N (12.00 lbf)). These masses were steel disks that weighed 623 g (1.374 lbf), 805 g (1.775 lbf), and 816 g (1.780 lbf).

Figure 3.5: Picture of static test rig #1

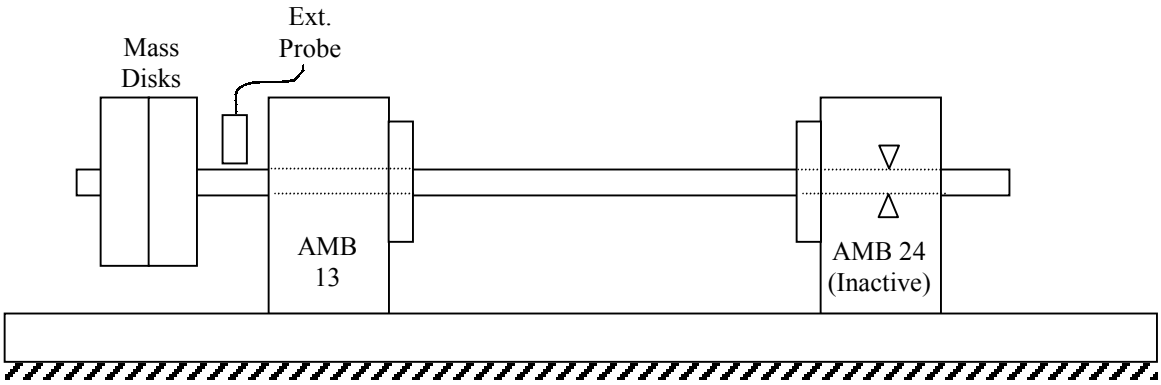

Figure 3.6: Schematic of static test rig #1

However, the method by which the bearing loads were calculated induced a higher level of uncertainty than was preferred. The overhung layout worked well to isolate one bearing and allow for high bearing loads, but the pinned end within the disabled bearing proved difficult to characterize. The layout of the components made it difficult to get accurate measurements of the moment arms from the pinned joint. Additionally, the force applied by the magnetic actuator is done so over the pole face area, and assuming a point location for the moment calculations was difficult. Any type of misalignment or inconsistency in the flux field would shift the effective point of application. The maximum calculated uncertainty was 0.77%.

Because only one of the bearings was used, the controller settings had to be modified in order to provide satisfactory results. The 2-4 bearing was completely turned off and the control settings for the 1-3 bearing are listed in Appendix C.

3.2.2 Static Test Setup #2

After completing the first set of static tests, it was desired to repeat the test with a different rotor configuration to reduce the bearing load uncertainty. As noted in section 3.2.1, the overhung arrangement induced a high level of uncertainty at 0.77%. Fully levitating the rotor with the AMBs avoids the problem of needing accurate moment arm measurements. The shaft was supported by both bearings, with two disk masses inboard of them. The bearing span for this configuration was 184.15 mm (7.25 in). Additional masses were added to the overhung ends outboard of the bearings. Figure 3.7 shows a picture of the modified static test rig. Figure 3.8 shows a schematic of static test #2. Making these changes required modification of the multi-point code and effectively doubled the number of calculations it performs since only one bearing was being used before, but this alteration of the computer code had already been recognized as necessary for the dynamic force tests. A reduction in the individual bearing loads also accompanied the move to a fully supported rotor, since instead of isolating the weight onto one bearing, the load was divided between the two. Several more disk masses were obtained and used in order to counter that loss and maintain the ability to test a wide range of operating conditions. Matching the individual bearing loads of the previous static test proved difficult, but tests were conducted using a total rotor weight range of 47.5 N (10.68 lbf) out of a maximum range of 106.8 N (24 lbf). These tests provided bearing loads from 10.9 N (2.44 lbf) up to 34.6 N (7.78 lbf). Appendix C contains the controller settings for the second static test.

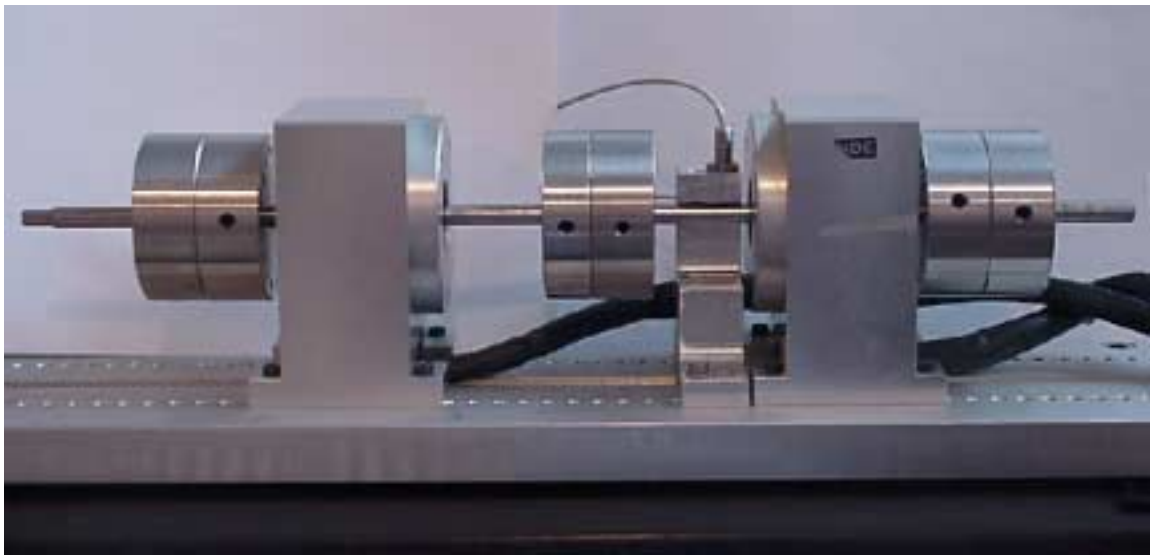

Figure 3.7: Photograph of static test rig #2

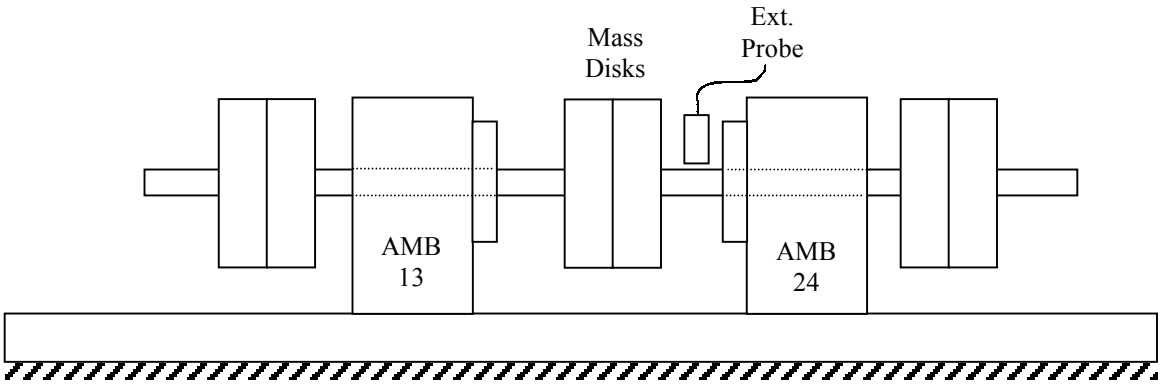

Figure 3.8: Schematic of static test rig #2

3.2.3 Dynamic Setup

The next logical step after completing the static testing was to determine if the multi-point approach would perform as well under a dynamic load. In order to test this, a third setup was configured. As with the previous test, it was desired for the setup to remain as simple as possible to eliminate unnecessary uncertainty. The dynamic test rig consisted of two AMBs that supported a shaft, which was connected to a motor with a flexible, rubber coupling. A mass was positioned on the shaft between the two bearings to provide for the addition of unbalance in further tests. The mass that was used at midspan was a steel disc of weight 816 g (1.780 lbf) and the total weight of the rotor components was measured as 15.63 N (3.51 lbf). The bearing span was 241.3 mm (9.5

in). A picture of the dynamic setup is shown in Figure 3.9 as well as a schematic in Figure 3.10. The control settings are listed in Appendix C.

Figure 3.9: Picture of dynamic test rig

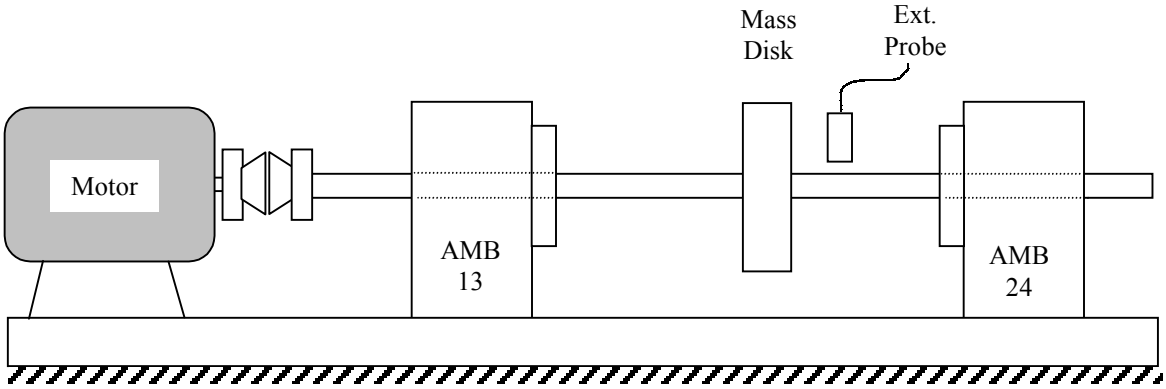

Figure 3.10: Schematic of dynamic load test rig

3.2.3.1 Rotor Dynamics

Because of the dynamic nature of the third test, it was necessary to understand the dynamics of the rotor system. This is because when a rotor is operated near its critical speeds, large amplitude and phase differences can be caused by small speed differences and small changes in bearing characteristics. This is important because the multi-point procedure assumes that the rotor is in the same position and under the same load when each current pair is recorded. The critical speeds of the rotor were found by performing a run-up test, accelerating the rotor from zero to 6000 RPM. Another potential problem is rotor mode shapes. Since the operation of the multi-point code (as shown in Appendix B) assumes the same rotor displacement for both bearings, any mode shape other than

cylindrical will generate unexpected results. This test was also conducted to ensure that the test speeds did not cross the first critical, and begin experiencing the higher modes.

Since the rotor was fully supported in AMBs, the nuances of their operation must be fully understood. It was mentioned earlier that when operating near a critical speed that small changes in bearing characteristics could result in large changes in rotor behavior. The stiffness of an AMB is not constant and is dependent on several factors, including the number of coils, pole face area, bias current, and air gap length. Since the bias current is being changed to obtain the required current pairs, the bearing stiffness is also changing. For this reason, it is important not to operate near the critical speeds of the rotor. The total stiffness of an AMB can be divided into two parts, position stiffness and current stiffness, and can be derived from Equation (3.1), the linearized force equation for a double-acting actuator (full derivation presented in Appendix B).

$$F_{th} = k_{th}\left(\frac{g i_b i_p - i_b^2 \Delta y}{g^3}\right) \tag{3.1}$$

The position stiffness is defined as the change in applied force per unit change in rotor position. The relationship governing position stiffness is given by Equation (3.2). The current stiffness is similarly defined as the change in applied force per change in coil current as is given by Equation (3.3). It is clear that a change in the bias current will affect both the current stiffness and position stiffness, which could lead to changes in critical speeds and vibration levels.

$$K_y = \left.\frac{\partial F}{\partial \Delta y}\right|_{ip=0} = \frac{-\mu_0 N^2 A_g i_b^2}{g^3} \tag{3.2}$$

$$K_i = \left.\frac{\partial F}{\partial i_p}\right|_{\Delta y=0} = \frac{\mu_0 N^2 A_g i_b}{g^2} \tag{3.3}$$

To test whether the shaft orbits were changing as the bias currents were modified, a proximity probe was positioned adjacent to the midspan disk to monitor shaft movement, which was then processed by Bently-Nevada's ADRE System. The ADRE system analyzes the proximity probe output and produces a variety of graphical presentations of that data, including waterfall plots, cascade plots, orbits, signal spectrums, and Bode plots.

For the test, 1.0 grams of unbalance was added to the disk mass at the 90° location. A slow sweep from 0-6000 RPM was performed with the top bias in the bearings set to 1.0 A. The Bode plots of the vertical and horizontal sensors are shown in Figures 3.11 and 3.12, respectively. The plots show a different critical between the vertical and horizontal directions. The first natural frequency of the vertical direction is around 3100 RPM, while the same for the horizontal direction is approximately 3600 RPM. The amplitude of the vertical peak is also higher than that of the horizontal probe (0.014 in,p-p vs. 0.012 in,p-p).

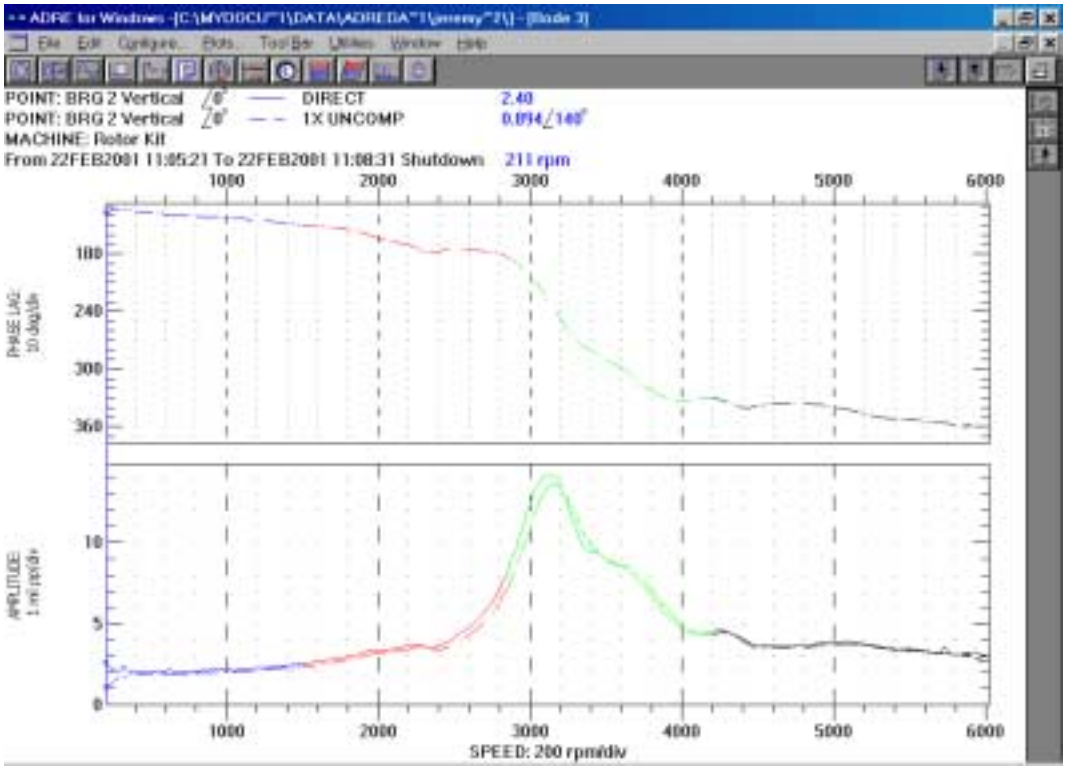

Figure 3.11: Bode plot of vertical probe with 1.0 g unbalance at 90° and 1.0 A top bias

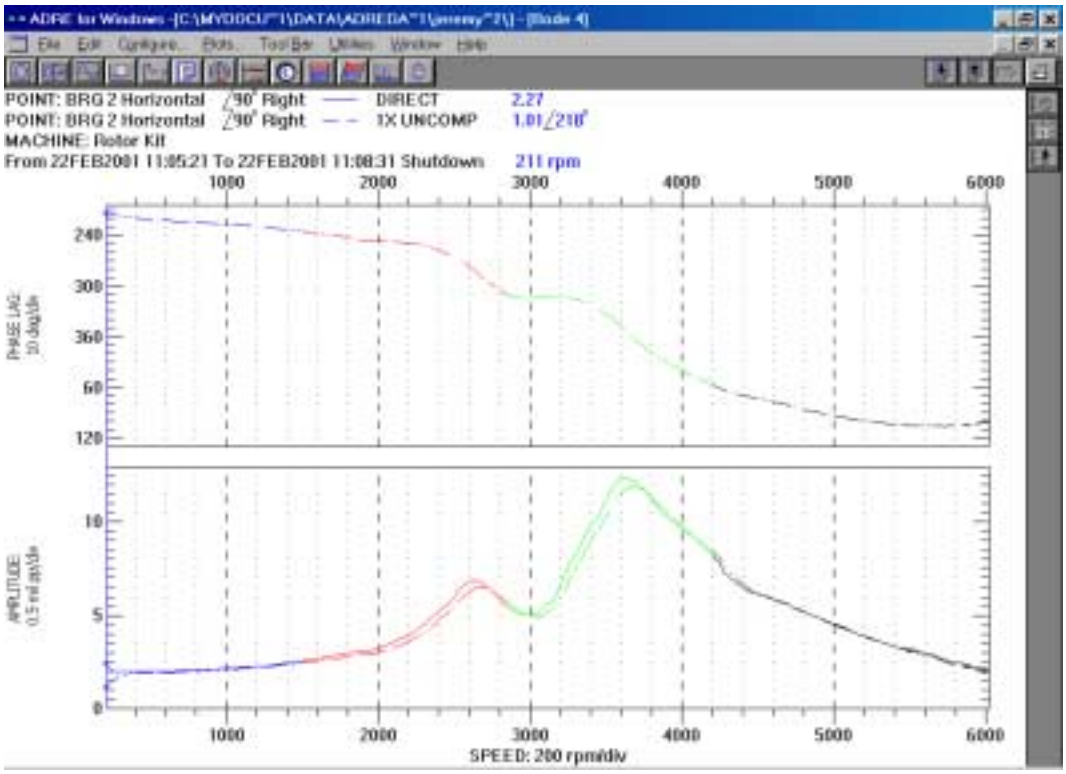

Figure 3.12: Bode plot of horizontal probe with 1.0 g unbalance at 90° and 1.0 A top bias

In order to determine if there was variation in the orbits due to the bias current changes, the same test was repeated, except the top bias current was changed to 2.0 A. The Bode plots for the second test are presented in Figures 3.13 and 3.14 for the vertical and horizontal probes, respectively. A direct comparison between the previous test case and this test with a different upper bias current is difficult due to the reduced speed range of the second set. Around 3600 RPM, the rotor began contacting its backup bearings, causing the degradation of the proximity signal past that point, as shown in Figure 3.14. It is difficult to determine where the first critical is for the vertical plot; it appears to peak around 3200 RPM, but it is not possible to tell whether it would have continued to climb had the bearing not touched down. The same can be said for the horizontal plot. However, for the range of speeds of interest, direct comparisons are possible.

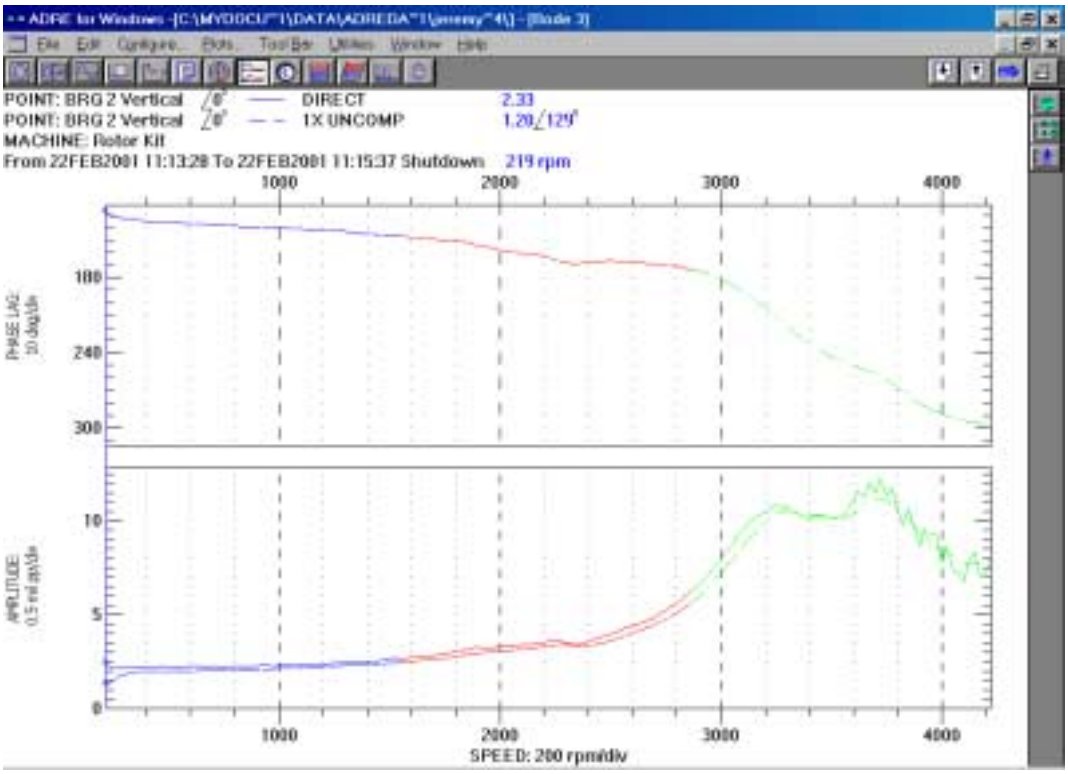

Figure 3.13: Bode plot of vertical probe with 1.0 g unbalance at 90° and 2.0 A top bias

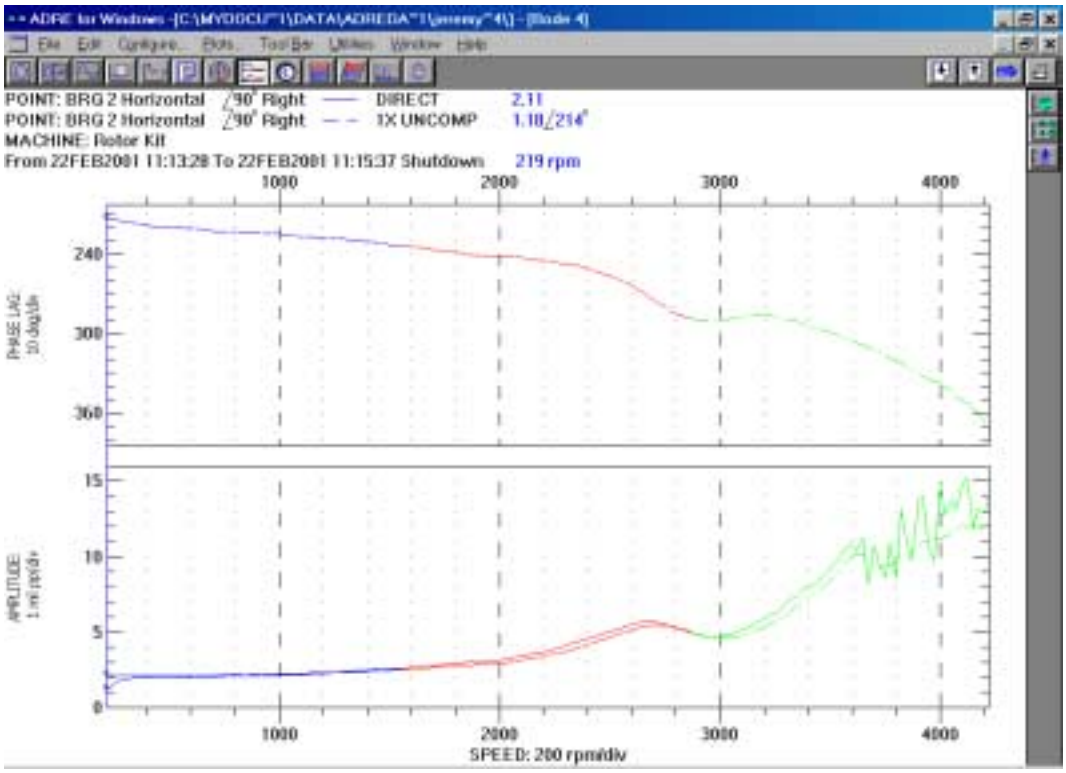

Figure 3.14: Bode plot of horizontal probe with 1.0 g unbalance at 90° and 2.0 A top bias

Table 3.2 summarizes the test speeds and amplitude levels for each. From Table 3.2, it is clear that the vibration levels in the vertical and horizontal directions are very similar when operated at 1.0 A and 2.0 A for the top bias current. Those are the lower and upper limits used for the top bias, and the differences between them are the largest that would be encountered. The largest difference is when operating at a speed of 2400; the horizontal vibration level decreased 12.7% (0.00062 in,p-p) when the top bias current is increased to 2.0 A. Except for that case, the largest change was in the vertical slow-roll condition, where vibrations increased by 7.1% (0.00015 in,p-p) when the top bias current is increased to 2.0 A.

Table 3.2: Amplitude levels for test speeds (mils)

Dir. & Bias / Speed	**Vertical Probe**		**Horizontal Probe**	
	1.0 A	**2.0 A**	**1.0 A**	**2.0 A**
485	2.05	2.20	2.00	2.12
1200	2.26	2.36	2.25	2.32
1800	2.99	3.01	2.97	2.92
2400	3.62	3.57	5.20	4.58

An interesting feature of both horizontal Bode plots is the peak at 2600 RPM. It appears only in the horizontal probe plots, and does not change frequency when the bias current changes. Because of these reasons, the peak is likely due to a structural resonance. The test rig was mounted on a cart with pneumatic tires that allowed the cart to rock, producing horizontal motion on the test surface. This base motion is the cause of the second peak and why it does not appear in the vertical plots.

While the Bode plots show that the experimental setup contains structural resonances within the maximum operating range of the motor/bearing system, the system was not operated within the problematic regions. However, at the test speeds there are still small variations in the orbits that will diminish the accuracy of the dynamic force predictions. Future work is necessary in order to minimize the errors associated with this problem. Additionally, the computer code should be modified so that calculations can be

performed on the individual bearings to account for different rotor behavior at each bearing, as found in higher mode shapes.

Chapter 4

Static Load Experimental Testing

4.1 Static Testing Introduction

After the successful MFEA validation, experimental tests were performed to continue the validation of the multi-point method. Two tests were used that utilized static loading. Static test #1 was configured in an overhung manner and used only one AMB for load support. The controller deactivated the other bearing and it was mechanically shimmed to provide an approximate pin support. Static test #2 used both AMBs to fully support the rotor. These tests were conducted to evaluate whether the multi-point method would produce accurate force and rotor location predictions regardless of rotor position or the magnitude of the load being measured.

4.2 Static Test Configuration #1

As described in Section 3.2.1, the first static test utilized an overhung configuration. A picture of the test rig is shown in Figure 4.1. The bearing on the right of Figure 4.1 was disabled and shimmed to provide an approximate pin joint. The left bearing was used to support the overhung load. In order to evaluate the multi-point method's response to different variables, tests were run with different shaft loads as well as with the rotor levitated at different locations within the bearing stator.

Figure 4.1: Picture of static test rig #1

Four load combinations were generated by the application of various combinations of disk masses onto the overhung end of the rotor, as shown on the left side of Figure 4.1. The four load cases evaluated were 16.73 N, 26.82 N, 37.94 N, and 48.49 N (3.76 lbf, 6.03 lbf, 8.53 lbf, and 10.90 lbf). These bearing loads were calculated by performing a moment balance about the pinned bearing. Figure 4.2 shows a schematic of the rotor and the required dimensions for determining the bearing force. The maximum static load capacity of the bearing is 53.4 N (12 lbf). The bearing span was 226.7 mm (10.5 inch).

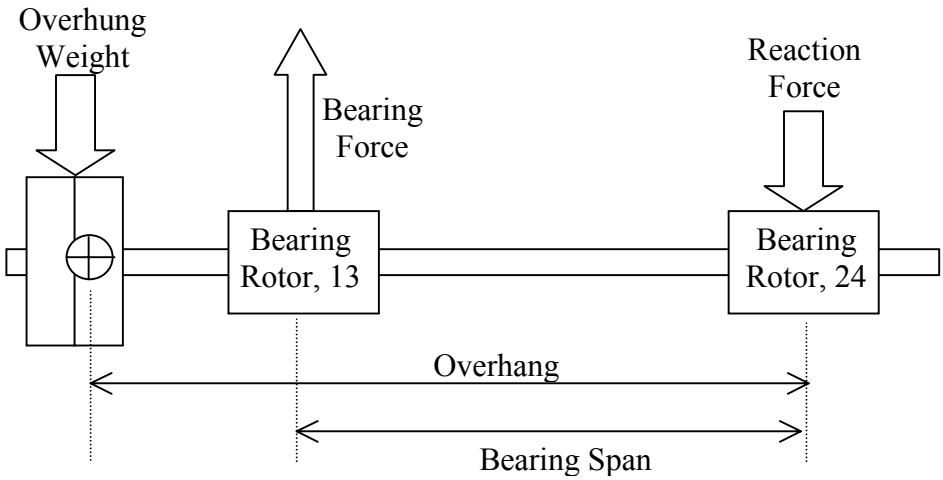

Figure 4.2: Static calculation of bearing force

Table 4.1: Summary of overhung weights and moment arms

Load Case #	Overhung Weight, N (lbf)	Overhang Moment Arm, mm (in)
1	8.01 (1.80)	400.1 (15.75)
2	14.10 (3.17)	412.8 (16.25)
3	22.02 (4.95)	404.1 (15.91)
4	29.89 (6.72)	391.2 (15.40)

The bearing loads were calculated using a moment balance about the mechanically shimmed bearing. The calculation consists of the overhung load multiplied by its moment arm added with the bare rotor weight multiplied by its moment arm, and the sum divided by the bearing span. For load case #1, the calculation is shown in Equation (4.1). The bearing span remained constant despite the different shaft loads. The weight of the bare rotor also did not change. The bare rotor consisted of the shaft and a bearing rotor and weighed 5.06 N (1.14 lbf) with a moment arm of 247.9 mm (9.0 in) from the pivot.

$$F_{\text{det}} = \frac{(8.01)(400.1) + (5.06)(247.9)}{266.7} = 16.72N \tag{4.1}$$

For each load case, five different rotor positions in the vertical direction were tested. By varying the rotor position, different air gap lengths were created to see if this variable affected the multi-point force or displacement predictions. The rotor is assumed to lie along the bearing centerline when it is levitated to the controller's "zero" position. The rotor locations were then referenced from this bearing centerline. The positive direction was defined as up, and in this way, "-0.127" is 0.127 mm below the bearing's controller-determined centerline. The horizontal position of the rotor was monitored during these vertical moves to ensure that the rotor was moving only in the vertical plane. In general, for a change in the vertical position of the rotor, the horizontal displacement was two orders of magnitude smaller than the vertical displacement. For the single-point force predictions, this small horizontal movement resulted in a change of less than 0.001 lbf (0.004 N) and was neglected. This range of tests produced 20 different combinations of shaft loads and rotor locations with which to test the multi-point algorithm.

For each combination of shaft load and rotor position, five sets of current pairs were recorded for use in the multi-point algorithm. For all of the combinations, a bias current of 0.75 A was used in the bottom halves of the double-acting actuators for each axis. However, the upper bias current sets were not consistent between load cases, because for the higher shaft loads increased upper bias levels were required for levitation of the additional weight.

The sets of current pairs were generated by cycling through a series of upper bias current settings, instead of technically injecting a perturbation current. At each bias value, the system was allowed to "settle" for a few seconds, and then the data was recorded. Although the effective rate of change of the bias current is very low (on the order of 1 A/min), there was a cyclic pattern and hysteresis was considered. Even though hysteresis was not directly accounted for in the experiment, steps were taken to minimize any problems associated with it. Since the control currents were predominantly non-alternating signals, the only source for hysteresis was from cycling the bias currents to collect the current pairs. Therefore, the pairs were collected by starting at the lowest bias setting and stepping through to the highest setting, so that each set was taken consistently. This ensured that the conditions were similar for each case (increasing bias current) and that the hysteresis effects were minimized. Additional evaluation of hysteresis effects is beyond the scope of this work.

4.2.1 Rotor Position Issues

In order to measure the accuracy of the displacement predictions, the actual rotor position must be known. As described in Chapter 3, and shown in Figure 3.3, the AMBs used in this experiment each have two axes of actuation. These axes are orthogonal and rotated 45° from the vertical and horizontal planes. The bearing controller allows for changing the position of the rotor with a set point parameter for each of the axes. If the set point is zero, the rotor is assumed to levitate at the bearing centerline. By changing the set point to a non-zero value, the neutral position of the rotor can be moved along the particular axis of interest. Since different rotor locations were desired along a vertical

plane, a combination of rotor offsets had to be entered to achieve these positions. For static test #1, the position offsets used were –80, –40, 0, 40, and 80 μm. For each location, the particular value was entered into the position offset control for both axes of interest. Because the radius of the bearing rotor is very large in comparison to the position sensor air gap, the two individual axis moves can be treated separately as vectors and added together to arrive at the total vertical rotor position. If an offset is input into the two axes, the resulting vertical displacement of the rotor is 1.414 (the reciprocal of sin(45°)) times the axis offset. While rotor position is easy to measure, the actual parameter of interest is the air gap associated with a particular location. For each rotor location, the top and bottom actuator air gaps can be calculated. Table 4.2 gives several offset values, the associated calculated vertical position of the rotor, and the approximate air gaps for each rotor position.

Table 4.2: Example offset values, vertical rotor positions, and approximate air gaps

Requested Control Position per Axis, μm (mils)	Equivalent Vertical Position, mm (mils)	Approx. Top Gaps, mm (mils)	Approx. Bottom Gaps, mm (mils)
-80 (-3.15)	-0.1131 (-4.45)	0.460 (18.1)	0.302 (11.9)
-40 (-1.57)	-0.0566 (2.23)	0.422 (16.6)	0.340 (13.4)
0 (0.00)	0.0000 (0.00)	0.381 (15.0)	0.381 (15.0)
40 (1.57)	0.0566 (2.23)	0.340 (13.4)	0.422 (16.6)
80 (3.15)	0.1131 (4.45)	0.302 (11.9)	0.460 (18.1)

To determine if the rotor was responding to the control inputs as expected, an eddy-current proximity probe was used to measure the rotor position. As shown in Figure 4.1, the proximity probe was positioned outboard of the active (left-hand) bearing. The position data observed with the eddy-current probe from several tests provided some confusion upon inspection, as it did not appear to correlate well with the controller-dictated position readings as the loading changed. In an attempt to explain this anomaly, a dial indicator was positioned on the rotor adjacent to the probe to provide a physical measurement of position. This further complicated matters, as it did not agree with either the controller or sensor reading. The cause of this dilemma was finally attributed to shaft bow as shown in Figure 4.3. The small diameter and long span of the shaft allowed significant flex as it was loaded. Even though the rotor was being supported at the

desired position at the AMB, the curve of the shaft due to the loading caused the sensor to show a different displacement. Additionally, since the dial indicator had to be positioned adjacent to the probe, it measured a different location and showed a different reading. After realizing this oversight, the dial indicator was applied directly adjacent to the bearing rotor, which did verify the controller's ability to maintain the centered position despite different loadings.

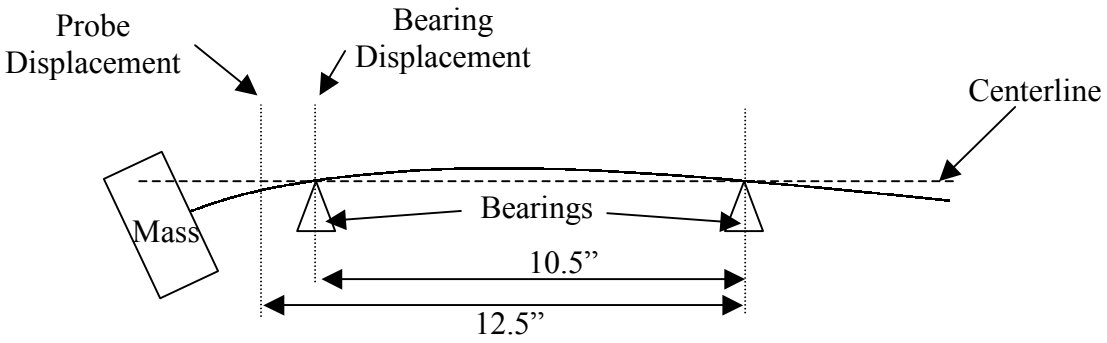

Figure 4.3: Effect of shaft flex on rotor position measurements, static test #1

The load effect is in essence a DC offset, since it is a constant error for each distinct load case. In order to eliminate this effect, the DC offset was removed from the eddy-current sensor readings to account for the shaft flex. This was performed on each of the separate load cases since the amount of flex would vary accordingly. Table 4.3 shows an example of this correction for load case #1.

Table 4.3: Example of eddy-current load correction

Equivalent Vertical Position, mm (mils)	E.C. Probe Reading, mm (mils)	E.C. Probe Reading After Correction, mm (mils)
-0.1131 (-4.45)	-0.177 (-6.97)	-0.106 (-4.20)
-0.0566 (2.23)	-0.164 (-6.45)	-0.053 (-2.10)
0.0000 (0.00)	-0.151 (-5.93)	0.000 (0.00)
0.0566 (2.23)	-0.138 (-5.42)	0.052 (2.06)
0.1131 (4.45)	-0.125 (-4.92)	0.103 (4.07)

Another problem regarding the proximity measurements is a geometric effect. Since one of the bearings is pinned and the other is used to for support and position

control, there is an induced lateral rotation as shown in Figure 4.4. Because the probe is positioned outboard of the AMB, it will observe larger displacements than the bearing rotor is experiencing. If it were inboard of the AMB, it would observe smaller displacements. To account for this non-collocation effect, a geometric correction factor was applied to all position measurements. This factor was calculated by measuring the distance from the pinned bearing to the active bearing and the proximity probe. The factor can then be determined using similar triangles. For static test #1, the correction factor was 0.81. That is, if the eddy-current probe reads 1.0 mils from the zero position, the bearing displacement is 0.81 mils.

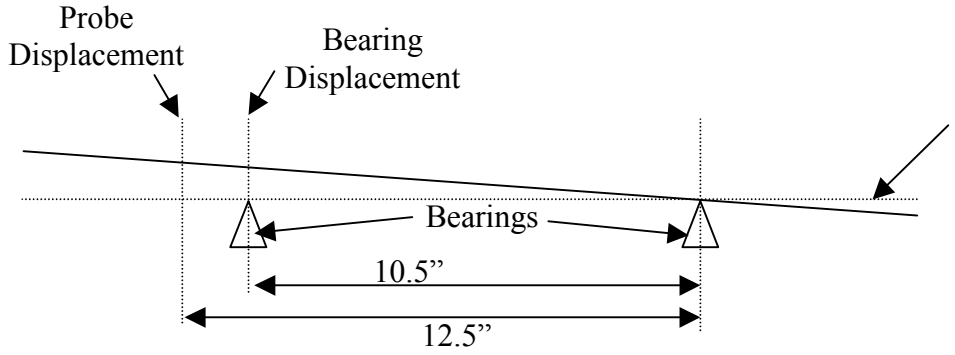

Figure 4.4: Geometric effect on proximity probe measurements (not to scale)

These two corrections, a shift for load effects and a linear multiplier for geometric effects, condition the position signals to provide a better representative measure of the displacement of the rotor within the bearing stator. Table 4.4 shows a sample of the controller inputs to the bearing axes, the calculated vertical displacement of the rotor, and measured values after each of the corrections.

Table 4.4: Sensor shift example, mm

Requested Control Position per Axis	Equivalent Vertical Position	Measured with Load-Effect Corr.	Measured with Load-Effect and Geometric Corr.
-0.08	-0.1131	-0.1319	-0.1068
-0.04	-0.0566	-0.0660	-0.0534
0.00	0.0000	0.0000	0.0000
0.04	0.0566	0.0646	0.0524
0.08	0.1131	0.1278	0.1035

Figure 4.5 shows the measured rotor positions after both corrections, plotted against the equivalent vertical rotor location for the controller inputs. This purpose of this plot is to graphically show the input/output relationship between requested position and measured position. A least squares regression analysis shows a slope of 0.9308 mm/mm and a y-intercept of -0.0347 mm. The r^2-value for the data is 0.9999. The ideal slope for this plot would be unity, meaning that the rotor is responding exactly to what is being requested of the controller. However, the value of 0.93 could mean that the geometric correction factor was slightly off. By changing it from 0.81 to 0.87, the slope becomes 0.9998 with essentially the same intercept and r^2-values. Conversely, the controller could be undershooting the desired location. The controller's positioning ability will be shown later to be sufficient, leaving the geometric correction factor the likely culprit. The eddy-current sensors also have an associated uncertainty that was analyzed by Clements (2000). A set of eleven probes yielded percent errors ranging from 0.45% to 2.33%. However, the linearity of the measurements instills confidence in their performance.

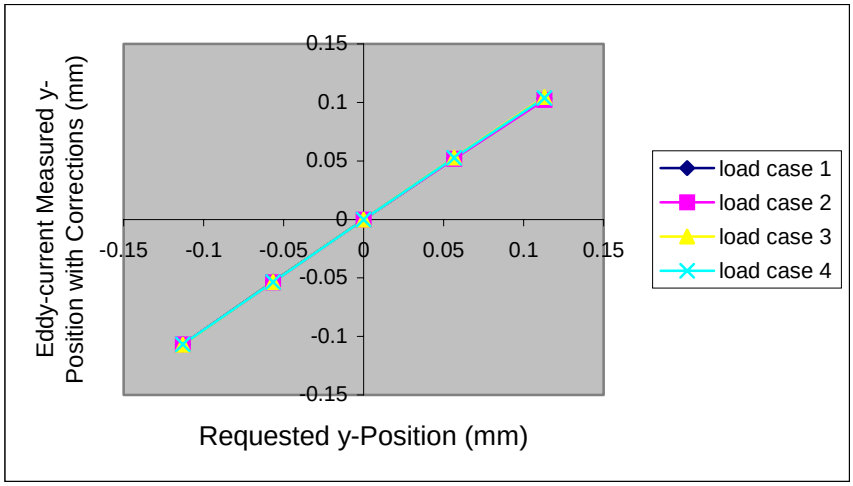

Figure 4.5: Controller-specified rotor position vs. measured position

4.2.2 Single-Point Predictions

To measure the accuracy of the multi-point force measurement technique, analogous single-point predictions were made so that the two methods could be directly compared. Most recent force predictions using magnetic bearings are performed using a single-point method that utilizes either Hall-effect sensors or current measurements as described in Chapter 1. In the following single-point force calculations, a form of Equation (1.7) is used along with measured coil currents and rotor displacements, as measured by an eddy-current probe and corrected according to the descriptions above, to estimate the force being applied by the bearing. So that a direct comparison may be made, this is the same force equation that is used in the multi-point algorithm. While the multi-point algorithm developed here requires that multiple current pairs be recorded for each combination of shaft load and rotor position while only one current pair is needed in addition to the air gap estimates for the single-point method. In order to calculate the single-point prediction, the first current pair of each set was used. The first pair was chosen to provide consistency between the different calculations. The variables of Equation (1.7) are i_1 and i_2, the current pair as measured from the controller, and x, the eddy-current probe measured and corrected rotor displacement.

$$F_{th} = \varepsilon \cdot k_{th}\left(\frac{{i_1}^2}{\left(2(g_0 - x) + b_{th}\right)^2} - \frac{{i_2}^2}{\left(2(g_0 + x) + b_{th}\right)^2} \right) \tag{1.7}$$

As defined in Chapter 1, k_{th} and b_{th} are calculated constants that are dependent on bearing properties. Equation (1.3) defines k_{th}, as well as the parameters for the bearings used in these tests. The pole face area of the actuator is 66.24 mm^2 (0.10267 in^2) and there are 228 coil windings around the poles. The permeability of a vacuum, μ_0, is $4\pi*10^{-7}$ H/m (1 H/m is equivalent to 1 N/A^2).

$$k_{th} = \mu_0 A_g N^2 \tag{1.3}$$

Similarly, the definition for bth and the assumed values used to calculate it are given in Equation (1.4). The equivalent iron path length is estimated to be 81.28 mm (3.2 in), and the relative permeability of the stator material is reported as 3000 by the manufacturer's specifications.

$$b_{th} = {L_i}/{\mu_r} \tag{1.4}$$

Table 4.5 gives the calculated values for k_{th} and b_{th} for the magnetic bearings used in this test. These are determined by bearing properties only and will not change with variations in rotor configuration.

Table 4.5: Calculated values for k_{th} and b_{th}

	Metric	English
k_{th}	$4.3266*10^{-4}$ N-mm^2/A^2	$1.5077*10^{-7}$ lbf-in^2/A^2
b_{th}	0.02718 mm	0.00107 in

4.2.3 Comparison Metrics

In order to quantify the results of the static testing, two metrics were defined that provide a means to measure the ability of the multi-point methodology and the

conventional single-point method to predict bearings loads at various rotor locations. These metrics were applied to each of the load cases, and each load case was tested at five different rotor positions. For each load case, the force predictions may be different for each rotor location, and these comparison metrics will provide a way to quantify these variations. The first measure is percent spread and is defined as

$$\%Spread = \left(\frac{\Delta F_{\max-\min}^{calc}}{F_{\det}} \right) \cdot 100\% \tag{4.2}$$

The term $\Delta F_{\max-\min}^{calc}$ is the minimum calculated force prediction subtracted from the maximum calculated force prediction. The term F_{det} is the mechanically calculated bearing load as described in Section 4.2. This percentage tells how much the calculated force values differ over the range of spatial locations.

The next measure to quantify the quality of the force predictions is percent error. This is simply defined as

$$\%Error = \left(\frac{F_{avg} - F_{\det}}{F_{\det}} \right) \cdot 100\% \tag{4.3}$$

where F_{avg} is the average value of the predicted forces across the spatial variations and F_{det} is the mechanical bearing load. Equation (4.3) gives a measure of how closely the measurement methods predict the nominal predetermined force. For both of these metrics, a low value is desired, with 0% being the ideal case.

4.2.4 Uncertainty Limitations

The performance metrics that are calculated with Equations (4.2) and (4.3) are based on mechanically determined bearing loads. For static test #1, these bearing loads were calculated as described in Section 4.2 instead of directly measured due to the overhung configuration of the rotor. Because of this, there is increased uncertainty in the F_{det} value. The worst-case percent uncertainty for this configuration is 0.77%, or 0.37 N,

and was for the heaviest load of 48.49 N. The load uncertainties vary from 0.70% to 0.77% across the different load cases and are summarized in Table 4.6. This load uncertainty is the lowest percent error that can be claimed for the multi-point method since the actual bearing load is only known to this accuracy. The details of the bearing load uncertainty calculations can be found in Appendix D.

Table 4.6: Static test #1 bearing load uncertainties

Load Case	Bearing Load (N)	% Uncertainty
1	16.73	0.72%
2	26.82	0.70%
3	37.94	0.75%
4	48.49	0.77%

The mechanical load uncertainties for static test #1 result from uncertainties associated with parameters used in the calculation of the bearing load. Figure 4.6 shows a schematic of the rotor. It was necessary to use a moment balance to calculate the bearing load in the overhung configuration. Errors arose in this procedure because several of the quantities are not known exactly. The exact location of the pin joint at bearing 24 was difficult to determine because it was located within the bearing housing. This created uncertainties in the measurement of the distance from the pin joint to the support AMB and to the distance to the overhung masses. Additionally, this joint could have provided a small amount of moment support, which was not modeled and could have introduced some error. The magnetic force applied by bearing 13 was a potential source of error as well. The force is actually applied over the entire pole face area of the actuator, but for the mechanical load calculation, it was necessary to determine a point location. The force was assumed to act at the center of the actuator, but this may not have been the case due to misalignment and non-uniform flux fields.

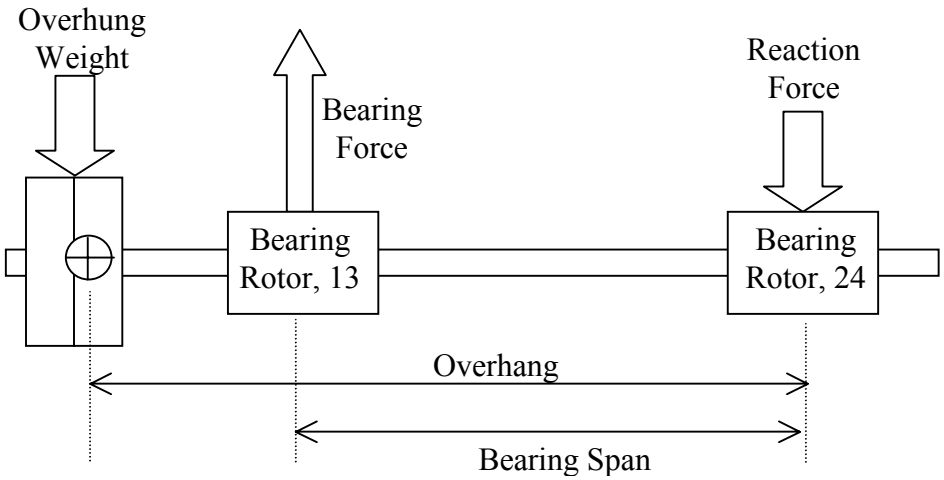

Figure 4.6: Static calculation of bearing force

4.2.5 Derating Factors

The derating factor used to generate the multi-point and both single-point force predictions for static test #1 were calculated empirically. The same procedure was performed on each method in order to determine the best value for the three different approaches. For the first load case tested (load case #1), the force prediction when the rotor was centered along the controller-determined centerline was used to calculate the derating factor. The experimental derating factor was calculated by dividing the mechanically determined bearing load by the predicted force, as shown in Equation (4.4) with the corrected single-point values. The multi-point derating factor was calculated as 0.869, the corrected single-point value was 0.970, and the non-corrected single-point factor was 0.972. These constant derating factors were then used across all of the shaft load and rotor position combinations for this rotor configuration.

$$\varepsilon = \frac{F_{\text{det}}}{F_{pred}} = \frac{16.73}{17.21} = 0.972 \tag{4.4}$$

4.2.6 Experimental Results – Static Test #1

The results of static test #1 are presented in Tables 4.7-4.10. Each table represents a different load case, and the mechanically determined bearing load is given in

the table heading. The multi-point predictions of bearing load and rotor position are given for each of the rotor test locations. The rotor locations given represent the equivalent vertical position of the rotor resulting from the input to the controller. The controller position inputs are for the axes of control, which do not align with the vertical direction, and must be converted to give a vertical displacement. Along with the multi-point predictions, two single-point force predictions are presented. The first of these uses the non-corrected position measurements as measured by the eddy-current probe. This calculation is included to show the errors that are possible when non-collocation errors are not accounted for and represents a realistic field scenario where misalignment and actual gaps are unknown. The other single-point prediction uses the corrected rotor position measurements. The values for percent error and percent spread for the predicted loads are given below the double line for the multi-point and both single-point predictions. Additionally, below each data table is a plot showing the multi-point and single-point predictions against the vertical rotor location as well as a line showing the mechanically determined bearing load.

Table 4.7 presents the results from the first load trial. The mechanically determined bearing load was 16.73 N. The multi-point algorithm was able to predict the bearing forces in this case very accurately. The percent error was –0.12%, and the percent spread was 1.53%. A common trend can be observed in the results of this load case that will appear in the rest of the data. As the rotor was moved from its lowest position, -0.1131 mm, to its highest, 0.1131 mm, the predicted forces for all of the methods increased. The magnitude of this increase is reflected in the percent spread values, where the multi-point method is much lower than either of the single-point methods. The percent spread for the non-corrected predictions is 25.85% and 6.06% for the corrected predictions.

Table 4.7: Data table for Case 1, F_{det} = 16.73 N (3.76 lbf)

Vertical Position	Multi-Point Algorithm Predicted Values		Single-Point Non-Corrected	Single-Point Corrected
mm (mils)	X, mm (mils)	F, N (lbf)	F, N (lbf)	F, N (lbf)
0.1131 (4.454)	0.118 (4.638)	16.52 (3.71)	19.36 (4.35)	17.21 (3.87)
0.0566 (2.227)	0.075 (2.946)	16.78 (3.77)	17.91 (4.03)	16.99 (3.82)
0 (0)	0.030 (1.170)	16.74 (3.76)	16.69 (3.75)	16.69 (3.75)
-0.0566 (-2.227)	-0.015 (-0.612)	16.78 (3.77)	15.80 (3.55)	16.48 (3.70)
-0.1131 (-4.454)	-0.060 (-2.382)	16.74 (3.76)	15.04 (3.38)	16.20 (3.64)
Percent Spread		**1.53**	**25.85**	**6.06**
Percent Error		**-0.12**	**-1.37**	**-0.10**

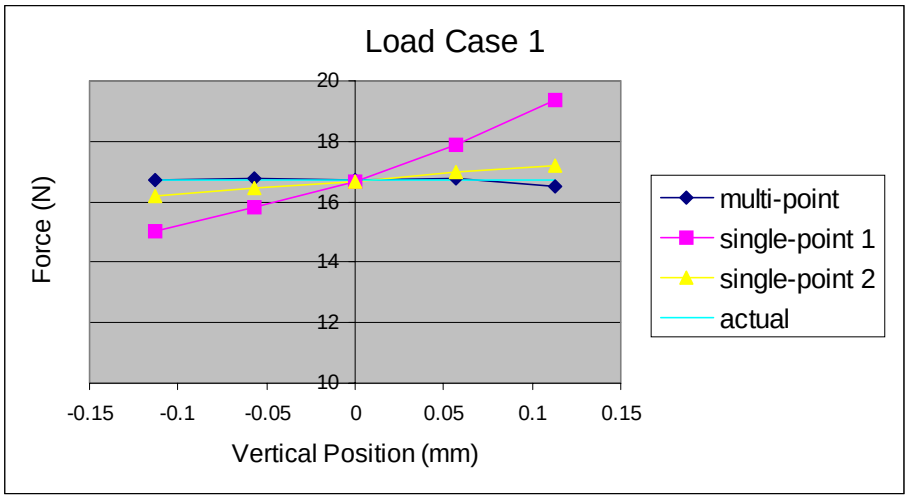

Figure 4.7: Load case 1 data plot, F_{det} = 16.73 N (3.76 lbf)

The results from the second load case are presented in Table 4.8. The same general trends from the first load case can be seen for this trial. One interesting feature of this load case is that the percent spread value for the corrected single-point predictions is lower than the multi-point force predictions value. This is a result of the force prediction corresponding to the bottommost rotor location, -0.1131 mm. The multi-point force prediction for that case is 25.69 N, which is more than a Newton lower than the other multi-point predictions for this load case. If this data point is exempted, the percent spread drops to 3.28%, which is similar to the multi-point percent spread values for the other load cases.

Table 4.8: Data table for Case 2, F_{det} = 26.82 N (6.03 lbf)

Vertical Position	Multi-Point Algorithm Predicted Values		Single-Point Non-Corrected	Single-Point Corrected
mm (mils)	X, mm (mils)	F, N (lbf)	F, N (lbf)	F, N (lbf)
0.1131 (4.454)	0.135 (5.322)	27.85 (6.26)	29.81 (6.70)	26.86 (6.04)
0.0566 (2.227)	0.086 (3.390)	27.19 (6.11)	27.81 (6.25)	26.55 (5.97)
0 (0)	0.039 (1.548)	26.97 (6.06)	26.26 (5.90)	26.26 (5.90)
-0.0566 (-2.227)	-0.038 (-1.500)	27.06 (6.08)	24.83 (5.58)	25.79 (5.80)
-0.1131 (-4.454)	-0.063 (-2.484)	25.69 (5.78)	23.56 (5.30)	25.25 (5.68)
Percent Spread		**8.03**	**23.32**	**6.02**
Percent Error		**0.49**	**-1.37**	**-2.53**

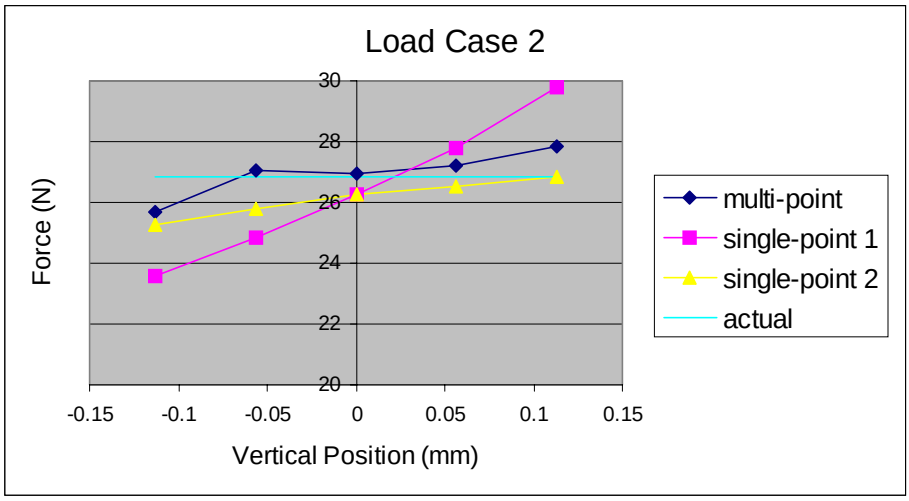

Figure 4.8: Load case 2 data plot, F_{det} = 26.82 N (6.03 lbf)

The force and location predictions for the third load case are shown in Table 4.9. The percent spread values for the multi-point and corrected single-point force predictions are very similar (3.12% as opposed to 2.06%, respectively). The non-corrected single-point predictions exhibit significantly more spread than the other two methods (19.01%). The multi-point predictions are slightly more accurate than the single-point force predictions as well, as evidenced by the percent error values.

Table 4.9: Data table for Case 3, F_{det} = 37.94 N (8.53 lbf)

Vertical Position	Multi-Point Algorithm Predicted Values		Single-Point Non-Corrected	Single-Point Corrected
mm (mils)	X, mm (mils)	F, N (lbf)	F, N (lbf)	F, N (lbf)
0.1131 (4.454)	0.136 (5.370)	37.16 (8.35)	40.08 (9.01)	35.90 (8.07)
0.0566 (2.227)	0.092 (3.624)	37.73 (8.48)	37.81 (8.50)	36.02 (8.10)
0 (0)	0.045 (1.758)	37.64 (8.46)	35.86 (8.06)	35.86 (8.06)
-0.0566 (-2.227)	-0.004 (-0.168)	37.25 (8.37)	34.21 (7.69)	35.54 (7.99)
-0.1131 (-4.454)	-0.057 (-2.244)	36.55 (8.22)	32.87 (7.39)	35.24 (7.92)
Percent Spread		**3.12**	**19.01**	**2.06**
Percent Error		**-1.78**	**-4.67**	**-5.88**

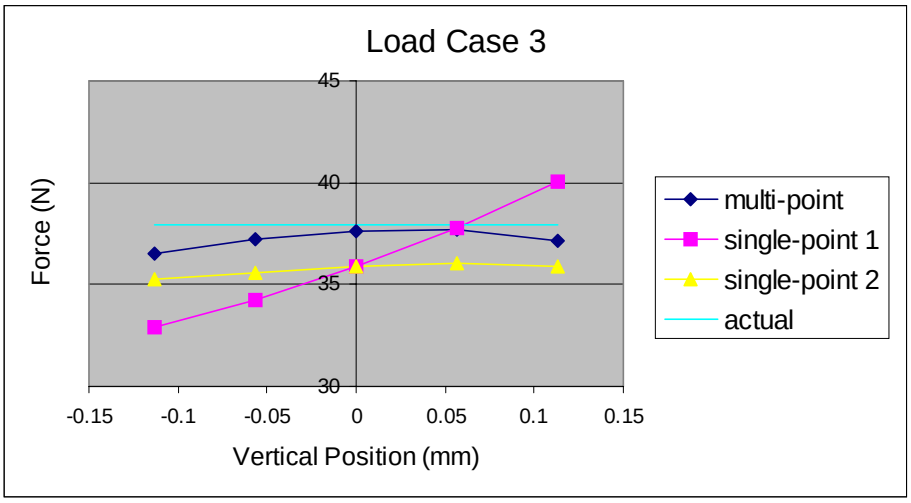

Figure 4.9: Load case 3 data plot, F_{det} = 37.94 N (8.53 lbf)

The fourth load case shows very similar results as load case three. In this case, the percent spread value for the corrected single-point force predictions is slightly lower than the multi-point predictions, and both are much lower than the non-corrected single-point percent spread value. All three methods appear to underpredict the bearing load for this load case, but the multi-point predictions show almost half the percent error of the two single-point predictions.

Table 4.10: Data table for Case 4, F_{det} = 48.49 N (10.90 lbf)

Vertical Position	Multi-Point Algorithm Predicted Values		Single-Point Non-Corrected	Single-Point Corrected
mm (mils)	X, mm (mils)	F, N (lbf)	F, N (lbf)	F, N (lbf)
0.1131 (4.454)	0.132 (5.208)	46.13 (10.37)	50.45 (11.34)	44.92 (10.10)
0.0566 (2.227)	0.088 (3.450)	46.69 (10.50)	47.39 (10.65)	45.02 (10.12)
0 (0)	0.044 (1.704)	47.44 (10.66)	45.07 (10.13)	45.07 (10.13)
-0.0566 (-2.227)	-0.006 (-0.223)	46.96 (10.56)	43.02 (9.67)	44.78 (10.07)
-0.1131 (-4.454)	-0.053 (-2.094)	46.83 (10.53)	41.52 (9.33)	44.58 (10.02)
Percent Spread		**2.71**	**18.41**	**1.02**
Percent Error		**-3.47**	**-6.19**	**-7.46**

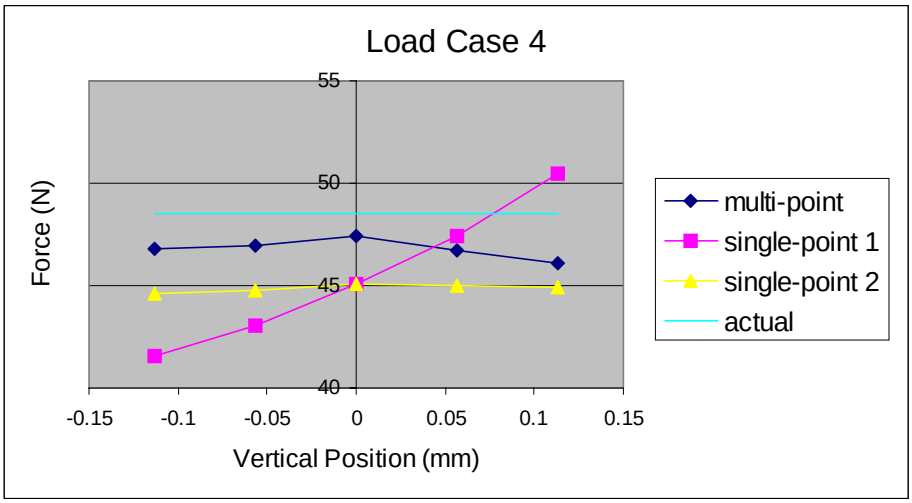

Figure 4.10: Load case 4 data plot, F_{det} = 48.49 N (10.90 lbf)

The maximum percent error observed in the multi-point predictions was –3.47%, as compared with –6.19% for the non-corrected single-point method and –7.46% for the corrected single-point predictions. The maximum percent spread value for the multi-point method is 8.03%. However, this is due to a questionable data point in the second load case. The force prediction for the bottommost rotor location is not consistent with the predictions for the other locations. If this one prediction is exempted, the maximum spread drops to 3.23%. The maximum percent spread value for the corrected single-point predictions is 6.06%, and 25.85% for the non-corrected predictions. On average, the multi-point method is able to provide an improved percent accuracy of 2.8% over the corrected single-point predictions. The percent spread values are almost equal on

average for the multi-point and corrected single-point predictions. It is notably improved (on average the percent error is better by 2.2% and percent spread by 17.8%) over the single-point predictions when non-collocation errors are unavoidable. A significant advantage of the multi-point method is that only current measurements are used to arrive at the force prediction. The single-point method required current measurements and position measurements as well as knowledge of other rotor information, such as non-collocation effects for accurate predictions. Therefore, the reduced input parameter requirements of the multi-point technique make it very attractive over single-point force measurement. In scenarios such as a fully AMB-levitated rocket thrust measurement system, many proximity probes would be required to fully monitor all six degrees of freedom. These probes would require additional hardware, computing power, and would have to be calibrated. Non-collocation errors could cause significant errors, and because of the multiple degrees-of-freedom, a simple correction factor as used in this work would not apply. In addition, the actual assembled gaps may not be well known and subject to thermal effects.

As shown in Table 4.11, the multi-point code also gives a prediction for the displacement of the rotor. While there is a discrepancy between the predicted displacements and the measured rotor position, the multi-point calculated values are not necessarily erroneous. The algorithm-predicted rotor displacements are relative to the true bearing centerline, where all of the air gaps are equal. If the controller does not levitate the rotor to that true centerline when it is centered, then there will be differences between the controller-specified rotor locations and the predicted locations. Additionally, the force relationship used in the multi-point code, Equation (1.7), is based on a simplified magnetic circuit approach, and does not address any of the known uncertainties in an experimental test, such as geometry uncertainties, rotor-stator alignment, material properties, or magnetic field effects (mainly fringing and leakage). It is possible that the displacement determined by the multi-point method actually defines an “effective gap” that may inherently account for the uncertainties mentioned above. Further investigation into this possibility is beyond the scope of this project.

Table 4.11: Multi-point predicted rotor displacements for static test #1

Equivalent Vertical Location	Load Case 1 16.73 N	Load Case 2 26.82 N	Load Case 3 37.94 N	Load Case 4 48.49 N
mm (mils)	X, mm (mils)	X, mm (mils)	X, mm (mils)	X, mm (mils)
0.1131 (4.454)	0.118 (4.638)	0.135 (5.322)	0.136 (5.370)	0.132 (5.208)
0.0566 (2.227)	0.075 (2.946)	0.086 (3.390)	0.092 (3.624)	0.088 (3.450)
0 (0)	0.030 (1.170)	0.039 (1.548)	0.045 (1.758)	0.044 (1.704)
-0.0566 (-2.227)	-0.015 (-0.612)	-0.038 (-1.500)	-0.004 (-0.168)	-0.006 (-0.223)
-0.1131 (-4.454)	-0.060 (-2.382)	-0.063 (-2.484)	-0.057 (-2.244)	-0.053 (-2.094)

Figure 4.11 shows the multi-point predicted displacements plotted against the controller-specified equivalent displacement (as defined in Section 4.2) for the four load cases. A linear least squares regression on the data shown produces an average slope of 0.8465 mm/mm and a y-intercept of 0.0361 mm (the r^2-value is 0.9846). The ideal fit would have a slope of unity and a zero intercept and would potentially indicate that the simple force equation (1.7) is sufficient and that there are no variations from the theoretical case. While discrepancies between the controller-dictated rotor location and the multi-point predicted rotor locations may be due to deficiencies in the multi-point methodology, the differences may also be an indication of inadequacies with the simplified force model of Equation (1.7). For example, the slope value of 0.85 may indicate that there is an unmodeled variable that is a function of rotor position, such as fringing. If the program is capable of accounting for fringing by predicting a different rotor location, then as the severity of the fringing increases, the amount of "correction" should increase as well. Since fringing is primarily a function of gap width (Imlach, 2000), the different rotor locations will cause varying levels of fringing, and the predicted displacement plot would be skewed. The non-zero intercept may mean that the equivalent iron path length is not accurate, the magnetic properties of the metal are not fully known, or that some other constant value is in error. It may also indicate that the controller centerline is not the true bearing centerline.

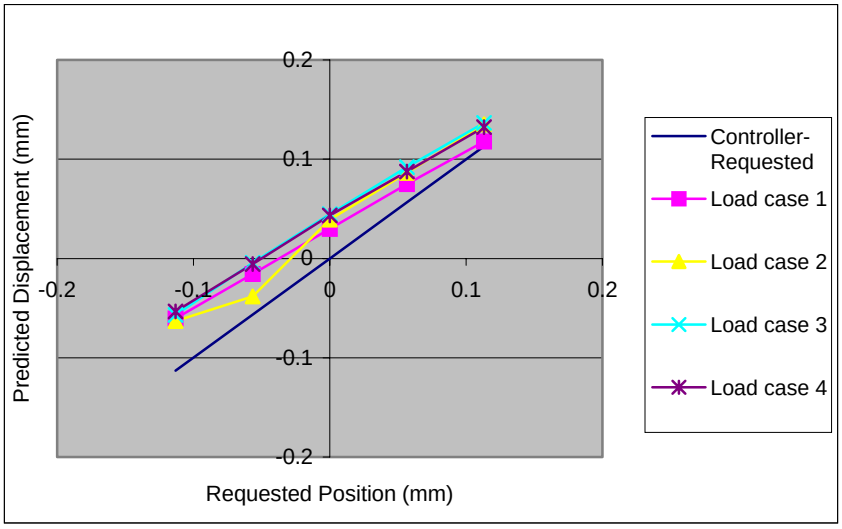

Figure 4.11: Multi-point predicted displacement vs. requested displacement

4.2.7 Conclusions – Static Test #1

The multi-point methodology proved to be a viable AMB force measurement technique over a wide range of applied forces and rotor positions in the static, overhung configuration utilizing a single bearing. Without using any position measurements, the multi-point method predicted the bearings loads with equal or better results than the single-point method that used position measurements in addition to current measurements. The multi-point method is ideal for situations where complex position measurements are unavailable or inaccurate. The maximum percent errors in the multi-point force predictions for this single-bearing overhung arrangement were on average 2.8% better than the corrected single-point predictions and 2.2% better than the non-corrected values. The percent spread for the multi-point method was on average 17.8% better than the non-corrected single-point prediction and almost equal for the corrected single-point predictions. The maximum percent spread for the multi-point predictions was 8.03%, but if a questionable point is not included this value drops to 3.23%. The single-point predictions with geometric corrections had maximum percent error of –7.46% and percent spread of 6.06%. If the position measurements are used without the geometric correction, which is the more realistic field scenario, the maximum percent error is –6.19% and the percent spread rises to 25.85%.

Graphical representations of the results from static test #1 are presented in Figures 4.12-4.14. In each graph, the average predicted bearing forces for the various methods are shown plotted against the number of disk masses used. The error bars represent the maximum and minimum force predictions for each load case. The line in each plot shows the mechanically determined bearing load for reference. Figure 4.12 shows the results for the multi-point method. The error bars are small for all load cases, and the average predictions do not vary far from the "actual" load line.

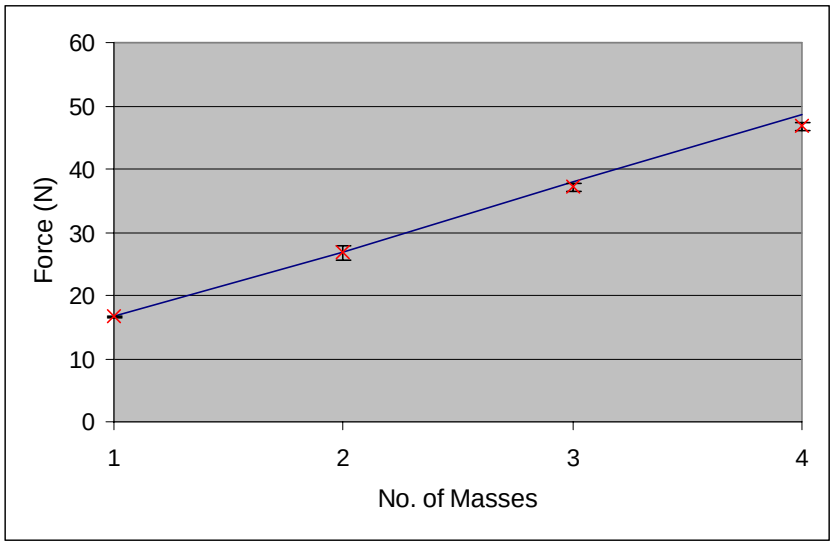

Figure 4.12: Multi-point max-min-average plot (static test #1)

The non-corrected single-point results are shown in Figure 4.13. The error bars for this prediction method are very large, which was noted in the percent spread values presented in Tables 4.7-4.10. The accuracy of the non-corrected single-point predictions begins to decline at the higher shaft load conditions.

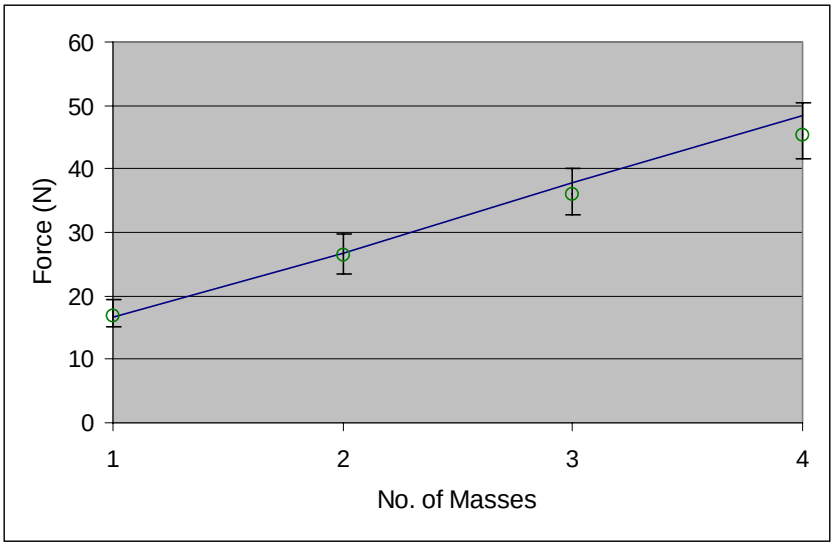

Figure 4.13: Non-corrected single-point max-min-average plot (static test #1)

The corrected single-point results are shown in Figure 4.14. The accuracy of this method is similar to the non-corrected single-point predictions, but the error bars are considerably smaller. The spread shown in the corrected single-point predictions is approximately equal to the multi-point predictions, but required rotor position measurements and knowledge of the non-collocation errors. The multi-point method achieved better accuracy than the corrected single-point method and similar spread in the data and required only a set of current pairs.

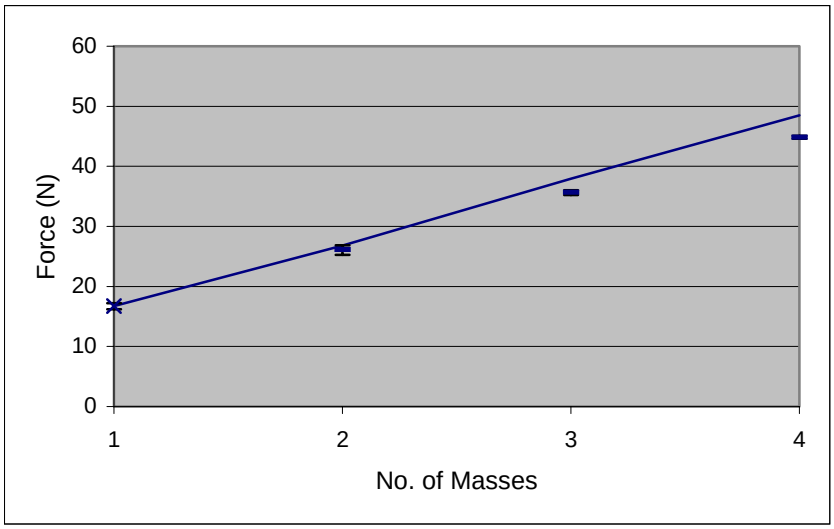

Figure 4.14: Corrected single-point max-min-average plot (static test #1)

In addition to bearing loads, the multi-point algorithm produces rotor displacement predictions. Since rotor position was varied in these tests, the accuracies of these predictions were analyzed as well. A linear regression was performed on the predicted displacements and showed an average slope of 0.85. Ideally, this would be unity, but the algorithm is possibly accounting for position varying effects, such as fringing, by reporting different displacements. The complexities of the flux fields are not modeled, but the multi-point procedure may be lumping these unknowns into the reported displacement value. The force equation used in the program is based on simple magnetic circuit theory, and the displacements that the algorithm generates correspond to the correct force. An analysis into the reason for these discrepancies is beyond the scope of this project.

4.3 Static Test Configuration #2

After the encouraging results from the first static test configuration, a second test was performed in an attempt to reduce mechanical measurement uncertainty and provide further verification of the merit of the multi-point technique. As described in Section 3.2.2, this configuration fully supported the rotor with two magnetic bearings. A picture of the second static test configuration is shown in Figure 4.15.

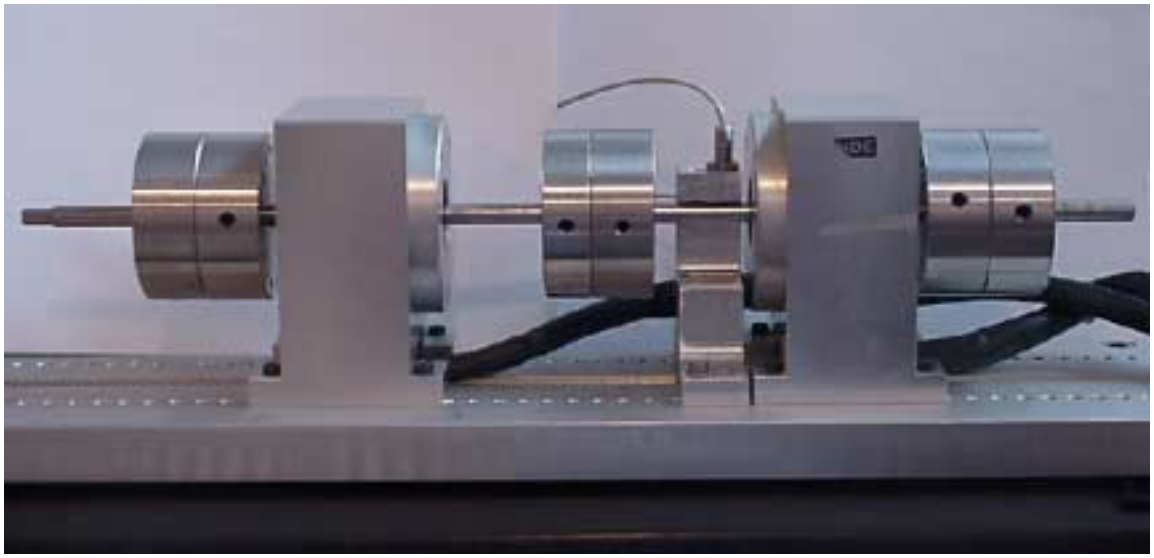

Figure 4.15: Picture of static test rig #2

The procedure used for testing this static set up was similar to that used in the first test. Different loads were applied to the rotor by attaching combinations of disk masses. The four load cases examined were 21.73 N, 37.69 N, 53.46 N, and 69.23 N (4.885 lbf, 8.474 lbf, 12.018 lbf, and 15.563 lbf). These weights represent the total weight of the rotor and the total load levitated by the two bearings. The maximum combined load capacity of the two bearings is 106.8 N (24.0 lbf). The bearing span for this configuration was 184.15 mm (7.25 in).

For each load case, the rotor was positioned in five different vertical locations to test whether the multi-point predictions were affected. The same procedure for measuring the rotor position was used for the second test as with the first static test. Since the different load cases induced varying amounts of shaft flex, the eddy-current position measurements were offset to align the sensor zero point with the bearing zero point. Figure 4.16 shows the effect of shaft flex due to the addition of disk masses. The geometric correction was not necessary in this configuration because as the location of the rotor was changed, both ends were displaced. This prevented the rotor from being pivoted and did not induce the non-collocation errors. Table 4.12 shows several examples of controller position inputs, the equivalent vertical rotor position, and the average measured vertical rotor position for the different load cases. The measured values were determined by the eddy-current probe positioned adjacent to one of the bearings.

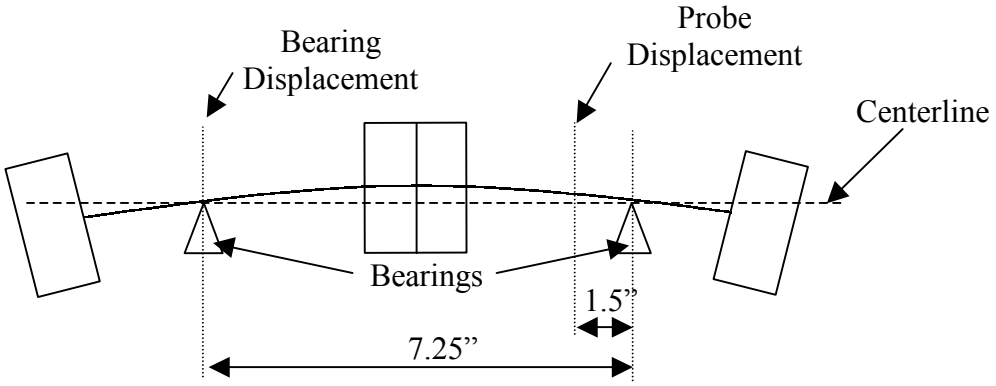

Figure 4.16: Effect of shaft flex on rotor position measurements, static test #2

Table 4.12: Sensor shift example, second static test (mm)

Requested Control Position per Axis	Equivalent Vertical Position	Sensor Measurement
-0.10	-0.1414	-0.1404
-0.05	-0.0707	-0.0700
0.00	0.0000	0.0000
0.05	0.0707	0.0684
0.10	0.1414	0.1327

This test assumes that the rotor is aligned within the bearing stators with no misalignment and that the displacement of the rotor is equal in both AMBs. Figure 4.17 shows the relationship between the controller-specified rotor position and the rotor position as measured by the eddy-current probe. The ideal relationship would show a one-to-one correlation between the requested and measured positions. The curve fit is linear with a slope of 0.9736 and an intercept of -0.0014 mm. This is very close to the ideal case, which indicates that the controller was performing as expected. The r^2-value for the linear curve fit was 0.9987.

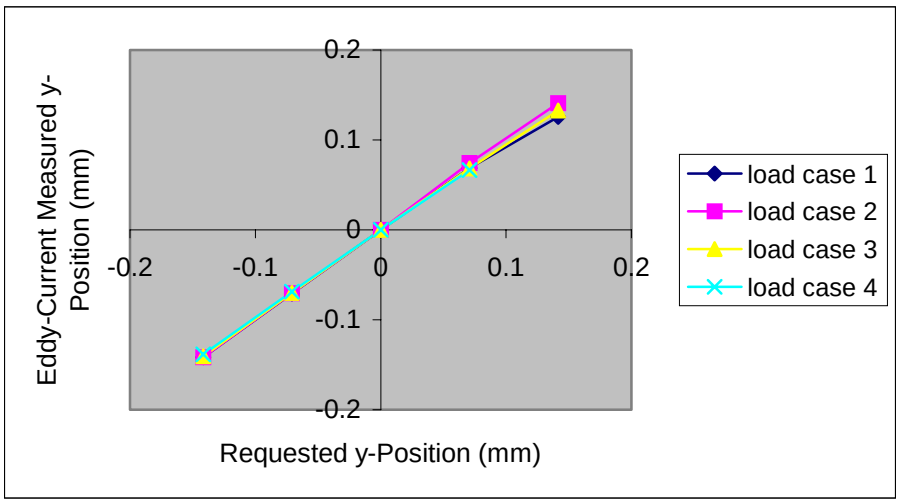

Figure 4.17: Requested vertical rotor position vs. measured rotor position

For each combination of shaft load and rotor position, a set of three current pairs was recorded for use in the multi-point algorithm. Five current pairs were used for each case in static test #1, but only three were used in this configuration to determine whether

there was any degradation in the quality of the force or position predictions. For all of the combinations, a bias current of 0.75 A was used in the bottom actuators. For each particular shaft load, the same series of upper bias currents were applied for all rotor position variations. However, the upper bias current sets were not consistent between load cases, because for the higher shaft loads higher upper bias levels were required for levitation. Concerns regarding hysteresis due to cycling of the bias currents exist in this configuration as in the first test. The same precautions were taken to guard against hysteresis as described in Section 4.2.

4.3.1 Uncertainty Limitations

For this configuration, the entire rotor is supported with AMBs and the total bearing load is easily measured. The uncertainty in the total bearing load for this case is solely from the measurement of the component weights and the limits of the scale that was used. The maximum uncertainty for the load cases used was ±0.005 N, or 0.023%, and the uncertainties are summarized in Table 4.13. The total bearing loads are the combined loads of the two AMBs used in this configuration. Appendix D details the calculation of these values. This level of uncertainty is up to two orders of magnitude smaller than the experimental accuracy, and does not limit the multi-point method accuracy.

Table 4.13: Static test #2 bearing load uncertainties

Load Case	Total Bearing Load (N)	% Uncertainty
1	21.73	0.023%
2	37.69	0.013%
3	53.46	0.009%
4	69.23	0.007%

4.3.2 Derating Factors

The derating factor used to generate the multi-point and single-point force predictions for static test #2 were calculated empirically. The same procedure was performed on each method in order to determine the best value for the two different approaches. For the first load case tested (load case #1), the force prediction when the rotor was centered along the controller-determined centerline was used to calculate the

derating factor. The experimental derating factor was calculated by dividing the mechanically determined bearing load by the predicted force, as shown in Equation (4.5) with the single-point values. The multi-point derating factor was calculated as 0.856, and the single-point value was 0.824. These constant derating factors were then used across all of the shaft load and rotor position combinations for this rotor configuration.

$$\varepsilon = \frac{F_{\text{det}}}{F_{pred}} = \frac{21.73}{26.36} = 0.824 \tag{4.5}$$

4.3.3 Experimental Results – Static Test #2

The multi-point and single-point predictions are presented in Tables 4.14-4.17. Each table represents a different load case, and the measured weight of the rotor is given in the table heading. The spatial location of the rotor is given in the first column of values. These values are determined by converting the controller inputs into an equivalent vertical displacement, as shown in Section 4.2.1. The multi-point predictions for bearing load and rotor position are given in each table as well. The analogous single-point force prediction for each rotor location is given to compare the two methods. Only one of the three current pairs in each set was required to determine the single-point force predictions, so the middle current pair was used in each calculation for consistency. The air gaps were determined using the measurement of shaft position from the eddy-current probe. The metrics used to quantify the quality of the measurements are the same as used in the initial tests. The percentage spread and percentage error definitions are given by Equations (4.2) and (4.3). The values for each of these metrics are given below the double line in each data table. Plots of the multi-point and single-point force predictions against calculated rotor displacement are shown below each of the data tables, in Figures 4.18-4.21. The mechanically determined bearing load is shown as a solid line in each plot. These figures graphically show the differences between the multi-point and single-point force predictions.

The results from the first load case are given in Table 4.14. The multi-point force predictions have a percent error of –0.14% and a percent spread of 2.75%. The single-

point force predictions show a higher percent error of –2.20%, and significantly higher spread of 17.35%. The single-point force prediction for the upper rotor location (0.1414 mm) is not consistent with the previous predictions, but the source of this anomaly was not determined.

Table 4.14: Data table for Case 1, F = 21.73 N (4.885 lbf)

Vertical Position	Multi-Point Algorithm Predicted Values		Single-Point Predictions
mm (mils)	X, mm (mils)	F, N (lbf)	F, N (lbf)
0.1414 (5.568)	0.125 (4.902)	21.37 (4.80)	21.99 (4.94)
0.0707 (2.784)	0.058 (2.292)	21.69 (4.88)	22.99 (5.17)
0 (0)	-0.002 (-0.072)	21.72 (4.88)	21.72 (4.88)
-0.0707 (-2.784)	-0.061 (-2.412)	21.74 (4.89)	20.33 (4.57)
-0.1414 (-5.568)	-0.119 (-4.692)	21.96 (4.94)	19.22 (4.32)
Percent Spread		**2.75**	**17.35**
Percent Error		**-0.14**	**-2.20**

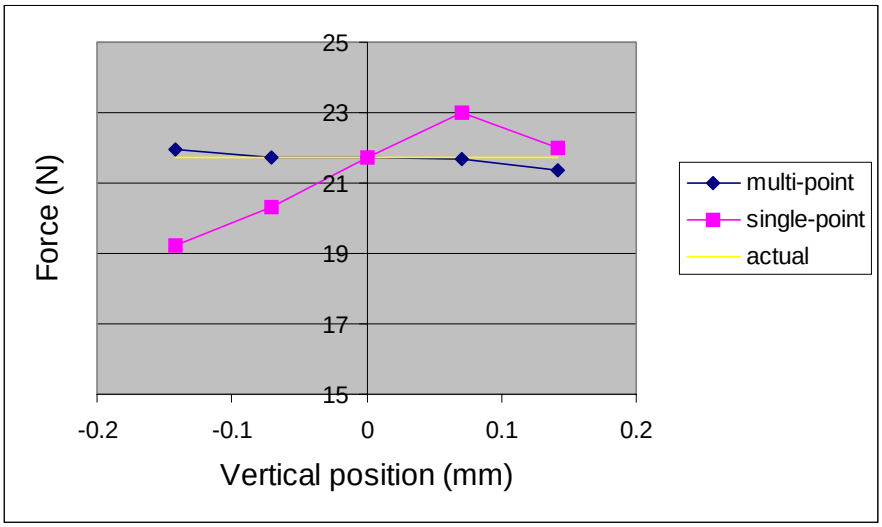

Figure 4.18: Load case 1 data plot, F = 21.73 N (4.885 lbf)

Table 4.15 presents the results of the second load case of static test #2, and the results are very similar to the first load case. The percent spread and error for the multi-point force predictions are 2.37% and 0.48%, respectively, as opposed to 20.05% and 2.63%, respectively, for the single-point predictions. The single-point force predictions for this load case appear linear when plotted against rotor position, as they did in static

test #1. The multi-point force predictions show a small reduction as the rotor is moved up or down from the centered position, but the variation is small, as shown by the percent spread value of 2.37%.

Table 4.15: Data table for Case 2, F = 37.69 N (8.474 lbf)

Vertical Position	Multi-Point Algorithm Predicted Values		Single-Point Predictions
mm (mils)	X, mm (mils)	F, N (lbf)	F, N (lbf)
0.1414 (5.568)	0.118 (4.638)	37.32 (8.39)	42.60 (9.58)
0.0707 (2.784)	0.061 (2.382)	38.18 (8.58)	40.96 (9.21)
0 (0)	0.003 (0.126)	38.22 (8.59)	38.28 (8.61)
-0.0707 (-2.784)	-0.057 (-2.226)	38.15 (8.58)	36.54 (8.21)
-0.1414 (-5.568)	-0.119 (-4.686)	37.51 (8.43)	35.05 (7.88)
Percent Spread		**2.37**	**20.05**
Percent Error		**0.48**	**2.63**

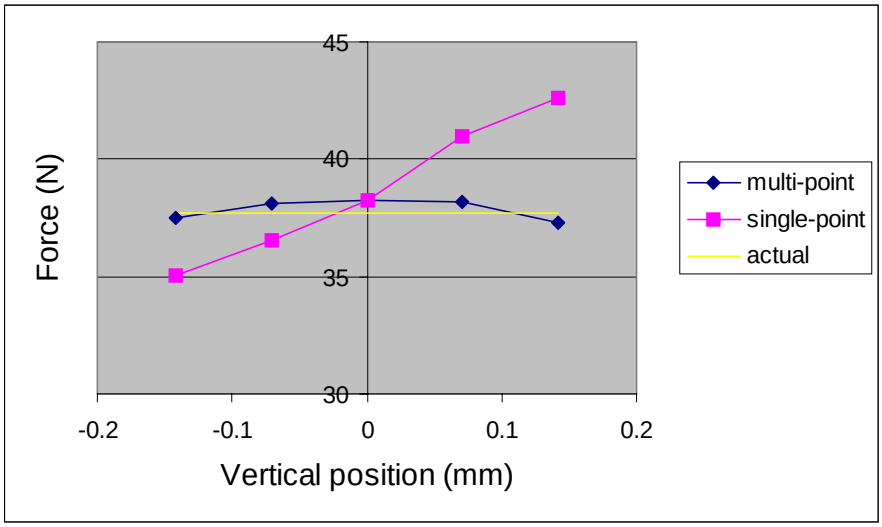

Figure 4.19: Load case 2 data plot, F = 37.69 N (8.474 lbf)

The results from the third load case are shown in Table 4.16. The percent error and spread values for both methods are similar to the previous two load cases with this configuration. The single-point percent error is less than the value for the multi-point predictions, but the percent spread is still over 15% higher than the multi-point method's. For the test case with the rotor in its uppermost position, the predictions for both methods showed a slight increase, as shown in Figure 4.20. This could be due to slight contact

with the backup bearings. As the rotor is loaded with additional weight, the shaft flexes as shown in Figure 4.16, and this could have reduced the backup bearing clearance and caused the rotor to contact one or both of them, causing the observed increase in predicted force.

Table 4.16: Data table for Case 3, F = 53.46 N (12.018 lbf)

Vertical Position	Multi-Point Algorithm Predicted Values		Single-Point Predictions
mm (mils)	X, mm (mils)	F, N (lbf)	F, N (lbf)
0.1414 (5.568)	0.133 (5.244)	55.16 (12.40)	58.86 (13.23)
0.0707 (2.784)	0.070 (2.766)	54.08 (12.16)	54.79 (12.32)
0 (0)	0.010 (0.402)	54.23 (12.19)	52.89 (11.89)
-0.0707 (-2.784)	-0.049 (-1.944)	54.16 (12.18)	50.79 (11.42)
-0.1414 (-5.568)	-0.109 (-4.272)	54.02 (12.14)	48.99 (11.01)
Percent Spread		**2.14**	**18.47**
Percent Error		**1.64**	**-0.36**

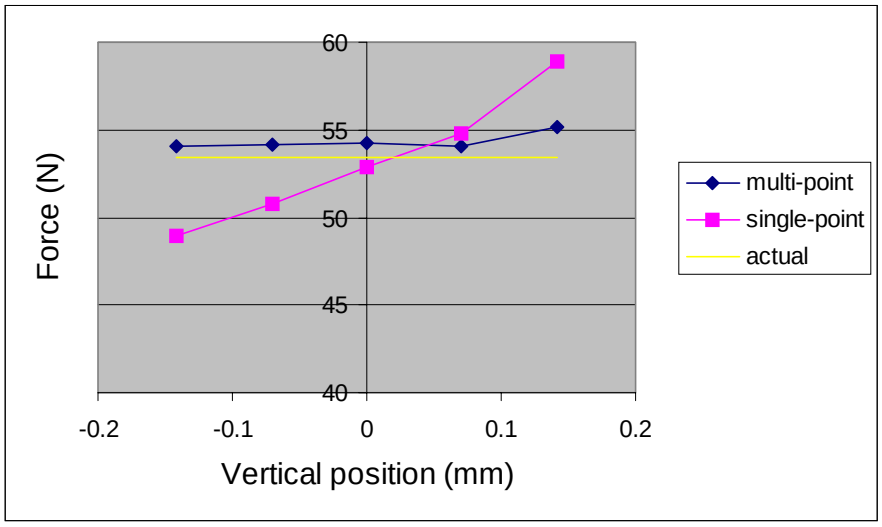

Figure 4.20: Load case 3 data plot, F = 53.46 N (12.018 lbf)

The results of the fourth load case are presented in Table 4.17. Under the full loading of 69.22 N, multi-point algorithm is able to provide very good results. The percent error and percent spread values are both less than 1%, while the single-point predictions are –5.96% and 5.76%, respectively. Only four rotor positions were used because of contact between the rotor and backup bearings in the topmost position. This

contact caused abnormally high force predictions for both the multi-point and single-point methods. Figure 4.22 shows the full set of rotor displacements as measured by an eddy-current probe plotted against the controller-requested rotor positions. The invalid data point can be seen, as it is not consistent with the others and could not reach the requested position.

Table 4.17: Data table for Case 4, F = 69.22 N (15.563 lbf)

Vertical Position	Multi-Point Algorithm Predicted Values		Single-Point Predictions
mm (mils)	X, mm (mils)	F, N (lbf)	F, N (lbf)
0.0707 (2.784)	0.078 (3.084)	69.99 (15.73)	66.96 (15.05)
0 (0)	0.017 (0.656)	69.94 (15.72)	65.93 (15.05)
-0.0707 (-2.784)	-0.044 (-1.746)	69.69 (15.67)	64.52 (14.50)
-0.1414 (-5.568)	-0.104 (-4.098)	69.47 (15.62)	62.97 (14.16)
Percent Spread		**0.75**	**5.76**
Percent Error		**0.79**	**-5.96**

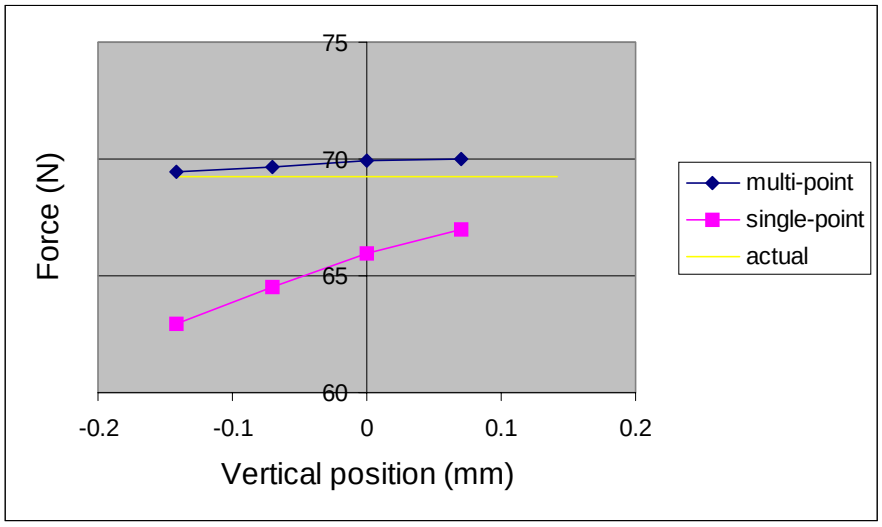

Figure 4.21: Load case 4 data plot, F = 69.22 N (15.563 lbf)

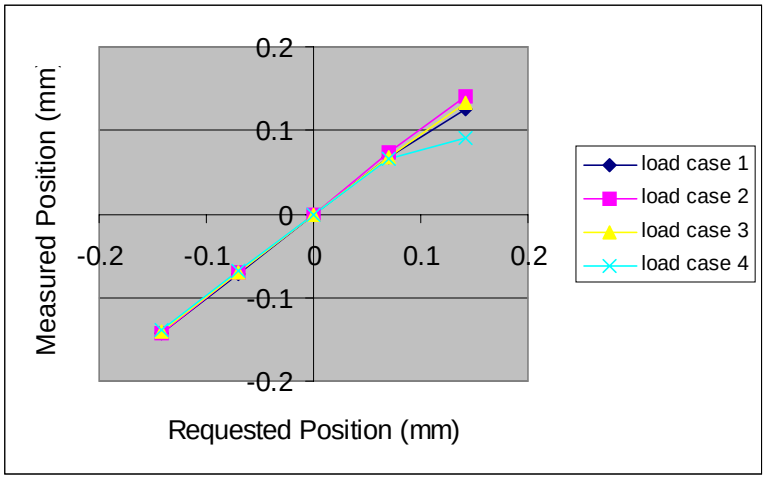

Figure 4.22: Controller-specified rotor position vs. measured position, all data

The maximum percent error of the four load cases determined by the multi-point method was 1.64%, as compared with –5.96% for the single-point method. The maximum percent spread for the multi-point method is 2.75%, while the maximum for the single-point measurements was 20.05%. The single-point percent spread values are of similar magnitude as the non-corrected single-point predictions from static test #1. While the large spread in the previous test was due to non-collocation errors, that problem is not present in the second static configuration.

There are discrepancies between the position predictions given by the multi-point code and the equivalent rotor position calculated from the controller inputs. Table 4.18 summarizes the multi-point predicted rotor displacements for each of the four load cases of static test #2.

Table 4.18: Multi-point predicted rotor displacements for static test #2

Equivalent Vertical Location	Load Case 1 21.73 N	Load Case 2 37.69 N	Load Case 3 53.46 N	Load Case 4 69.22 N
mm (mils)	X, mm (mils)	X, mm (mils)	X, mm (mils)	X, mm (mils)
0.1131 (4.454)	0.125 (4.902)	0.118 (4.638)	0.133 (5.244)	- (-)
0.0566 (2.227)	0.058 (2.292)	0.061 (2.382)	0.070 (2.766)	0.078 (3.084)
0 (0)	-0.002 (-0.072)	0.003 (0.126)	0.010 (0.402)	0.017 (0.656)
-0.0566 (-2.227)	-0.061 (-2.412)	-0.057 (-2.226)	-0.049 (-1.944)	-0.044 (-1.746)
-0.1131 (-4.454)	-0.119 (-4.692)	-0.119 (-4.686)	-0.109 (-4.272)	-0.104 (-4.098)

It is important to recall that these displacements are reference from the true bearing centerline, and that the displacements calculated from the controller inputs may not be referenced to the same position. The controller bases the rotor location on its centerline that is determined from its dedicated proximity probes, but does not necessarily have to be the true bearing centerline. The true centerline is the rotor location where all of the air gaps are equal. However, there may be some information that can be determined from the trends shown by these predictions, if not the actual values. Figure 4.23 shows the predicted rotor displacements as computed by the multi-point algorithm plotted against the requested displacement for each of the four load cases.

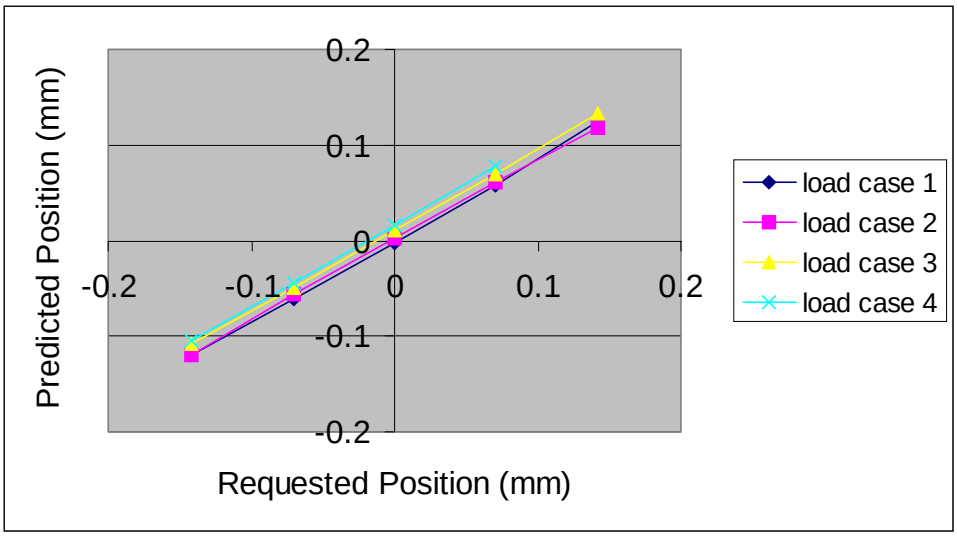

Figure 4.23: Controller-requested displacement vs.
multi-point predicted displacements

As the applied weight is increased (from load case one through four), the predicted displacement line is shifted up as well. This means that the misalignment caused by the flexing of the shaft under the weight of the additional mass (as shown in Figure 4.16) is possibly being accounted for in the "effective gap" reported by the program. A least squares regression on the data shows a slope of 0.8426 and a y-intercept of 0.0067 mm (with an r^2-value of 0.9928). The average slope of 0.84 is possibly caused by changes in the magnetic flux field in the air gaps as the rotor moves from the bottom to the top of the

actuator. Again, the program may be accounting for changes in the bearing operating conditions, such as fringing variations, by reporting changing effective gap widths.

4.3.4 Conclusions – Static Test #2

The second static trial used a rotor that was fully levitated with two AMBs. This configuration allowed for more control over mechanical parameters than the overhung, single-bearing configuration used in static test #1. In the new configuration, the multi-point method was able to produce force predictions with consistently lower spread in the predictions than the single-point method. On average, the percent spread values for the multi-point method were 13.4% lower than the single-point method. The multi-point algorithm was also able to predict the shaft forces with an average of 3.2% better accuracy. The multi-point predictions showed a maximum percent error of 1.64%, compared with –5.96% for the single-point method. The maximum percent spread for the multi-point technique was 2.75%, versus 20.05% with the single-point predictions.

Graphical representations of the accuracy and spread of the results of the multi-point and single-point force predictions are given in Figure 4.24 and 4.25. In each graph, the average predicted bearing forces for the various methods are shown plotted against the number of disk masses used. The error bars represent the maximum and minimum force predictions for each load case. The line in each plot shows the mechanically determined bearing load for reference. Figure 4.24 shows the multi-point results for static test #2. The error bars are small and the average predictions for each load are very close to the mechanically determined value.

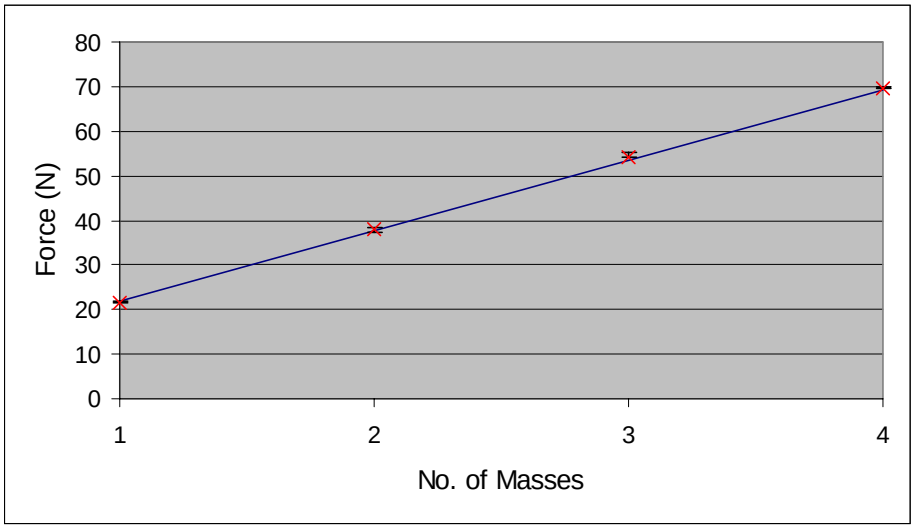

Figure 4.24: Multi-point max-min-average plot (static test #2)

The single-point results are shown in Figure 4.25. The single-point force predictions show noticeably more spread than the multi-point predictions. Additionally, the single-point prediction for the fourth load case is lower than the mechanically determined value by almost 6%. The multi-point method was able to provide force predictions that were more accurate and more precise while not requiring any rotor position measurements.

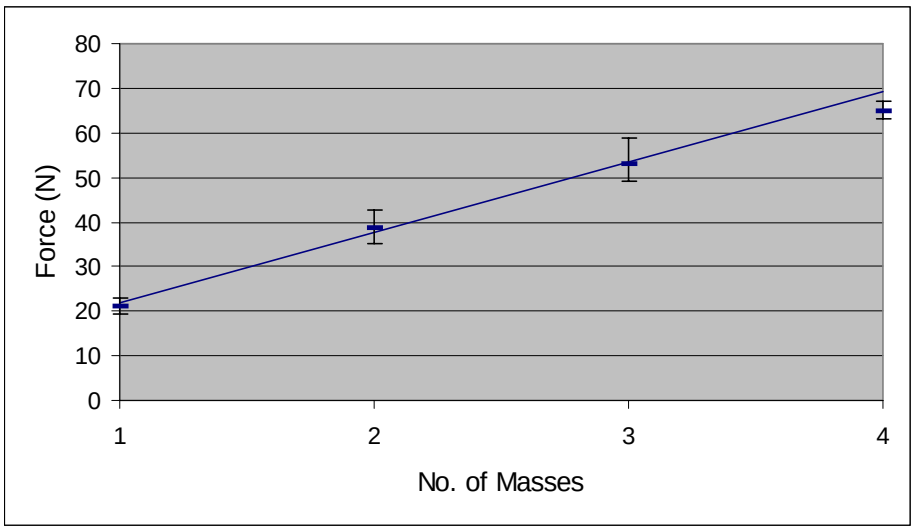

Figure 4.25: Single-point max-min-average plot (static test #2)

In addition to bearing loads, the multi-point algorithm produces rotor displacement predictions. Since rotor position was varied in these tests, the accuracies of these predictions were analyzed as well. A linear regression was performed on the predicted displacements and showed an average slope of 0.85. This same slope was observed in the predicted displacements for static test #1. Both test configurations introduced significant amounts of shaft flex and misalignment to the bearings and this may be the reason for the similar observed slope in the predicted displacement plot. As stated in Section 4.2.6, the ideal slope would be unity, but the algorithm is possibly accounting for position varying effects, such as fringing, by reporting different displacements. The complexities of the flux fields are not modeled, but the multi-point procedure may be lumping these unknowns into the reported displacement value. The force equation used in the program is based on simple magnetic circuit theory, and the displacements that the algorithm generates correspond to the correct force. An analysis into the reason for these discrepancies is beyond the scope of this project.

The multi-point predictions for static case #2 were calculated using only three current pairs. Static test #1 used five pairs for each combination of shaft load and rotor position. There is no apparent loss of accuracy or precision by using a reduced number of input current cases. This is advantageous because the number of required current pairs is directly proportional to the amount of time required to both record the data and process it. However, three current pairs is the recommended minimum number of current pairs. Since the search routine compares the forces calculated with the various current pairs, using only two sets would likely result in a loss of accuracy. Further investigation into the number of current pairs and the effect it has on the multi-point algorithm is beyond the scope of this project.

4.4 Misalignment Effects

The results of the secondary static tests implied that shaft flex, or more generally, misalignment between the rotor and stator of a magnetic bearing, could have a large effect on the multi-point displacement predictions. The version of the multi-point algorithm that was used for these static tests did not allow for independent bearing

calculations. During operation, the code generates a single vector of potential rotor displacements that is used for both bearings. This assumes that the rotor moves within the two bearings in exactly the same way. This is not ideal, but to find the limits of this assumption, a test was conducted to analyze the effects of misalignment on the multi-point calculations.

4.4.1 Test Configuration

The same setup was used for this experiment as for the second static test. Figure 4.15 shows an illustration of the apparatus, which had two AMBs that levitated a shaft with two masses inboard of the bearings. No additional disk masses were added to the rotor, leaving a rotor weight of 21.73 N (4.885 lbf). Misalignment was created by moving the rotor in different directions with the two bearings. For example, if the 13 bearing moved the shaft up 0.1 mm, then the 24 bearing would move it down 0.1 mm. This induced a misalignment of the rotor within the bearing stator. Tests in both the vertical and horizontal planes were tested. Three current pairs were recorded for each test case for use in the multi-point algorithm. The top bias currents used were 1.0 A, 1.5 A, and 2.0 A. The bottom bias current was 0.75 A for all cases. Since no single-point comparisons were required, the external eddy-current probe was not used.

4.4.2 Misalignment Results

The results of the two misalignment tests are shown in Tables 4.19 and 4.20. The controller specified rotor locations are given in columns one and two, and columns three and four give the multi-point algorithm predictions for force and displacement. The percent spread and percent error values for the predicted forces are given below the double line. These percentages were calculated in the same way as for the other static tests using Equations (4.2) and (4.3).

Table 4.19: Vertical misalignment test results, F = 21.73 N (4.885 lbf)

1-3 Bearing Position, mm (mils)	2-4 Bearing Position, mm (mils)	Multi-point Prediction	
		x, mm (mils)	F, N (lbf)
0.0424 (1.670)	-0.0424 (-1.670)	0.0288 (1.134)	21.45 (4.846)
0.0141 (0.557)	-0.0141 (-0.557)	0.0098 (0.384)	21.56 (4.870)
0.0 (0.0)	0.0 (0.0)	0.0009 (0.036)	21.73 (4.909)
-0.0141 (-0.557)	0.0141 (0.557)	-0.0070 (-0.276)	22.16 (5.005)
-0.0424 (-1.670)	0.0424 (1.670)	-0.0276 (-1.086)	21.94 (4.955)
Percent Spread			**3.24**
Percent Error			**0.18**

Table 4.20: Horizontal misalignment test results, F = 21.73 N (4.885 lbf)

1-3 Bearing Position, mm (mils)	2-4 Bearing Position, mm (mils)	Multi-point Prediction	
		x, mm (mils)	F, N (lbf)
0.0424 (1.670)	-0.0424 (-1.670)	-0.0035 (-0.138)	21.64 (4.887)
0.0212 (0.835)	-0.0212 (-0.835)	-0.0030 (-0.120)	21.54 (4.865)
0.0 (0.0)	0.0 (0.0)	-0.0012 (-0.048)	21.72 (4.905)
-0.0212 (-0.835)	0.0212 (0.835)	-0.0005 (-0.018)	21.69 (4.900)
-0.0424 (-1.670)	0.0424 (1.670)	0.0003 (0.012)	21.61 (4.882)
Percent Spread			**0.81**
Percent Error			**-0.42**

The accuracy and precision metrics for the force predictions are very similar to the values obtained for the other static tests. These results indicate that the multi-point algorithm can be exposed to misalignments and still operate as intended to provide accurate force predictions. The horizontal test did provide lower values for percent spread and error, which could indicate a directional dependence, but this is beyond the scope of this project. Figure 4.26 shows a plot of the predicted forces against the calculated 1-3 bearing location for the two tests. The r^2-values for the linear curve fits on the force data are low (0.65 and 0.02), meaning that there is very little dependence between the predicted force and the amount of misalignment. Table 4.21 summarizes the coefficients of the curve fits on the force prediction data.

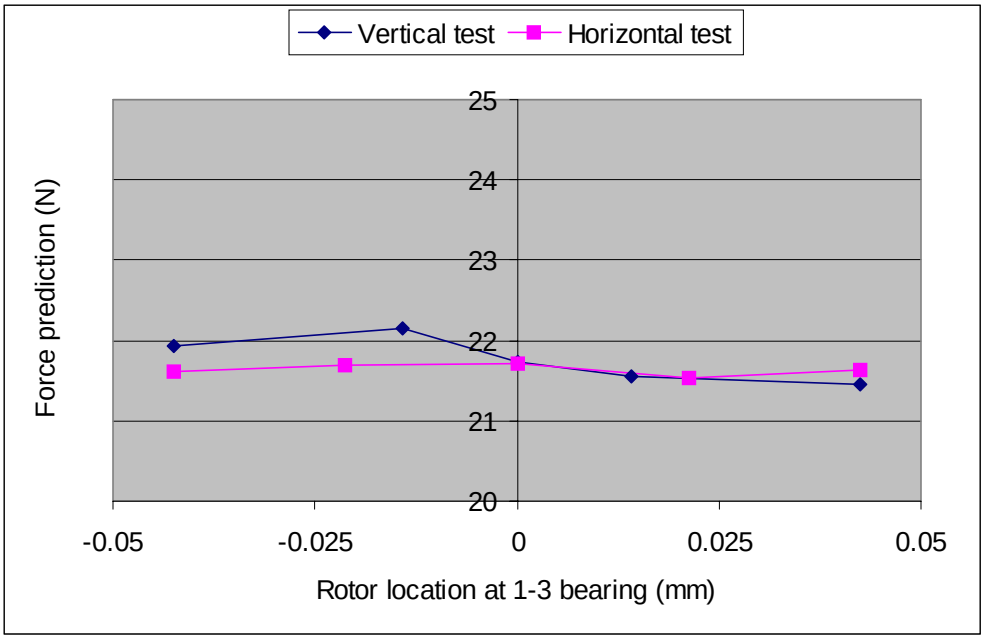

Figure 4.26: Predicted forces vs. 1-3 bearing displacement

Table 4.21: Summary of force prediction linear regressions

Test Type	Prediction	Slope (N/mm)	y-Intercept (N)	r^2
Vertical	Force	-7.2335	21.769	0.6469
Horizontal	Force	-0.3134	21.640	0.0201

The predicted displacements, however, show a different result. The multi-point algorithm predictions for rotor displacement assume that both bearings are experiencing the same displacement and that the rotor is level. This test was performed to investigate how the algorithm would react to this violation of one of its assumptions. Figure 4.27 shows a plot of the displacement predictions against the 1-3 bearing location for the vertical and horizontal tests. The linear nature of the vertical results was quite surprising. The sign of the slope is arbitrary (the data could have been plotted against the 2-4 bearing location, which would mirror the plot about the y-axis), but there is a definite relationship between predicted displacement and bearing misalignment. The results that were expected would have shown an odd function (such as y=|x|) that would reflect the symmetry of the test. Since the rotor setup is symmetric about the midpoint of the shaft, it would be expected that misaligning the rotor one way or the other should give the same results, but that does not appear to be the case.

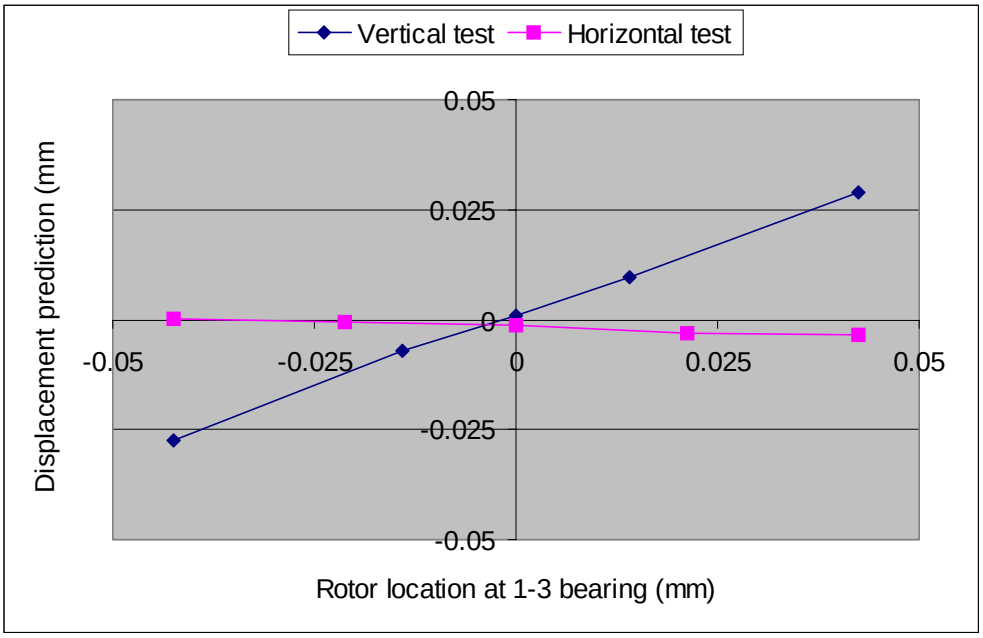

Figure 4.27: Vertical and horizontal displacement predictions vs. rotor location at 1-3 bearing

Table 4.22 gives the curve fit coefficients for the predicted displacement tests as shown in Figure 4.27. Very good correlation with misalignment is evident in the data, as shown by the high r^2-values (0.9986 and 0.9650). However, the large difference in the slopes for the two cases appears misleading. It would seem that for small misalignment angles, the program should predict the same displacement for either direction. The flux field is experiencing the same distortion regardless of the direction of misalignment, and the offset of the rotor in one bearing should cancel the offset in the other.

Table 4.22: Summary of displacement prediction linear regressions

Test Type	Prediction	Slope (mm/mm)	y-Intercept (mm)	r^2
Vertical	Displacement	0.6574	0.0010	0.9986
Horizontal	Displacement	-0.0481	-0.0016	0.9650

The difference may lie in how the axes are arranged and how the program assumes displacements. Figure 4.28 shows two rotor displacements and the effect of each on the air gaps. When the rotor is moved vertically as shown in Figure 4.28(a), the

top gaps for each axis get smaller and the bottom gaps get larger. This keeps the axes "coupled," where each axis is experiencing the same sort of change. However, when the rotor is displaced horizontally (Figure 4.28(b)), the two axes become "uncoupled." The top air gap for axis V13 becomes smaller, but the top gap for axis W13 becomes larger. Since the multi-point algorithm is trying to model the actual physical rotor displacements with purely vertical displacements, the splitting of the axes caused by a horizontal displacement could effectively cancel out the movement within the bearing and cause it to not appear in the predicted displacement.

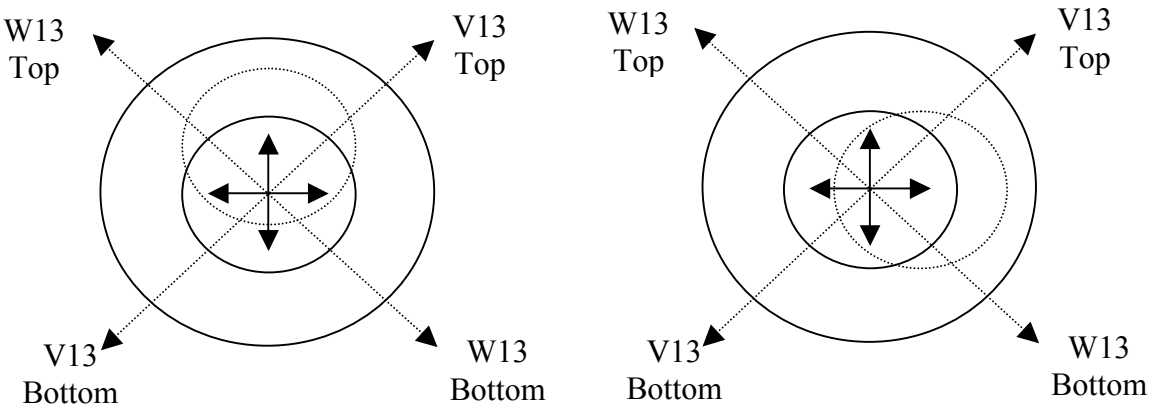

a) Vertical Displacement b) Horizontal Displacement

Figure 4.28: Rotor displacements and the effect on air gaps:
(a) vertical and (b) horizontal directions

4.4.3 Misalignment Test Conclusions

A brief misalignment test was conducted to further analyze the "effective gap" principle mentioned above. By creating a known misalignment between the rotor and stator of the bearings, the multi-point rotor displacement predictions were used to determine if the program could detect this misalignment and, if so, how the algorithm would perform despite the misalignment. The misalignments were generated in the vertical and horizontal planes to see if there was a directional dependence, and the results were mixed. The force predictions for the various misalignment settings were consistent with the previous static tests in regards to the performance metrics. The vertical

misalignment test showed a percent error and spread of 0.18% and 3.24%, respectively. The horizontal misalignment test generated percentages of -0.42% and 0.81%, respectively. The very low percentage spread for the horizontal test seems to indicate that horizontal misalignment has very little influence on the force predictions. The multi-point predicted rotor displacements were also analyzed with respect to misalignment. The vertical test results showed a very strong linear relationship between misalignment and predicted rotor position. The horizontal test showed a linear relationship, but the slope was much smaller, as shown in Figure 4.27. This may be due to an "uncoupling" of the axes when horizontal misalignment is present, but further investigation into this hypothesis is beyond the scope of this project.

Chapter 5

Dynamic Load Experimental Testing

5.1 Dynamic Testing Introduction

After successfully completing the static tests as described in Chapter 4, an initial dynamic test was performed that would assess the multi-point method's ability to predict forces in a dynamic scenario. This configuration produced mixed success, but will facilitate future work to focus on test parameters that most influence the measurement of dynamic forces. Because of interaction between unbalance loads and shaft bow, and the unknown effects of the driving motor, direct comparisons of the predicted dynamic loads were not successful. However, the trends of the multi-point predictions relative to the experimental parameters were analyzed with moderate success.

The different sections of this chapter will outline different aspects of the dynamic testing. The slight modifications required to facilitate dynamic force prediction with the multi-point algorithm are presented and the implications of the changes are discussed. The loading mechanism for the rotor is described and the different combinations for testing are presented. The amount of unbalance, the location of the additional unbalance, and the rotor speed were all varied to test the multi-point method with a wide range of rotor conditions. The multi-point method calculation technique allowed for the calculation of three different force levels. By manipulating these forces, the static rotor weight was determined as well as the dynamic forces due to the unbalance loading and shaft bow. Several methods for quantifying the dynamic loads were assessed, but none provided consistent results. The general trends of the dynamic loads in response to

different variables were examined with greater success. Comparisons could be made to the static weight predictions and they were encouraging.

5.2 Dynamic Test Configuration

After successfully completing the static tests as described in Chapter 4, an initial The dynamic test rig is described in Section 3.2.3, and a picture of the setup is shown in Figure 5.1. Both AMBs were used for levitation, and the motor was used to drive the shaft. A single mass was positioned at the midspan of the rotor so that unbalance could be added. Different combinations of unbalance and speed were used to analyze whether the multi-point method could predict these dynamic loads. The weight of the rotor components was measured as 15.63 N (3.51 lbf), and the bearing span was 241.3 mm (9.5 in).

The different combinations of unbalance mass, unbalance location, and rotor speed were tested according to the following procedure. For a given unbalance location, and a given unbalance mass, the different rotor speeds were tested from the slowest to fastest speeds. After the different speeds are tested for one level of unbalance, the amount of unbalance is increased and the different rotor speeds are tested for that condition. When all of the unbalance and speed combinations have been tested for one angular location, the process is repeated for a different location. For each of the angular locations, the first unbalance condition tested is the balanced case. By testing the rotor without any additional unbalance, the amount of shaft bow can be monitored throughout the test to determine if it is changing.

Figure 5.1: Picture of dynamic test rig

5.3 Dynamic Multi-Point Algorithm Changes

Before the tests were conducted, however, several modifications to the multi-point computer algorithm were made. In order to use the multi-point method for dynamic force predictions, a different approach had to be taken that differed from the static testing. The relationship used to predict the bearing loads is given by Equation (1.7).

$$F_{th} = \varepsilon \cdot k_{th}\left(\frac{i_1^{\,2}}{(2(g_0 - x) + b_{th})^2} - \frac{i_2^{\,2}}{(2(g_0 + x) + b_{th})^2} \right) \tag{1.7}$$

Because the rotor is rotating and the forces are dynamic, the rotor position eddy-current measurements, x, and the AMB current signals, i_1 and i_2, are changing in time, and it is difficult to use them directly for any calculations. An example waveform of rotor position is shown in Figure 5.2. The rotor was rotating at 1200 RPM and had 0.5 g of unbalance placed at 225°. Under this particular loading, the rotor was experiencing a vibration of 0.045 mm, p-p (1.77 mils, p-p) at the location of the eddy-current probe.

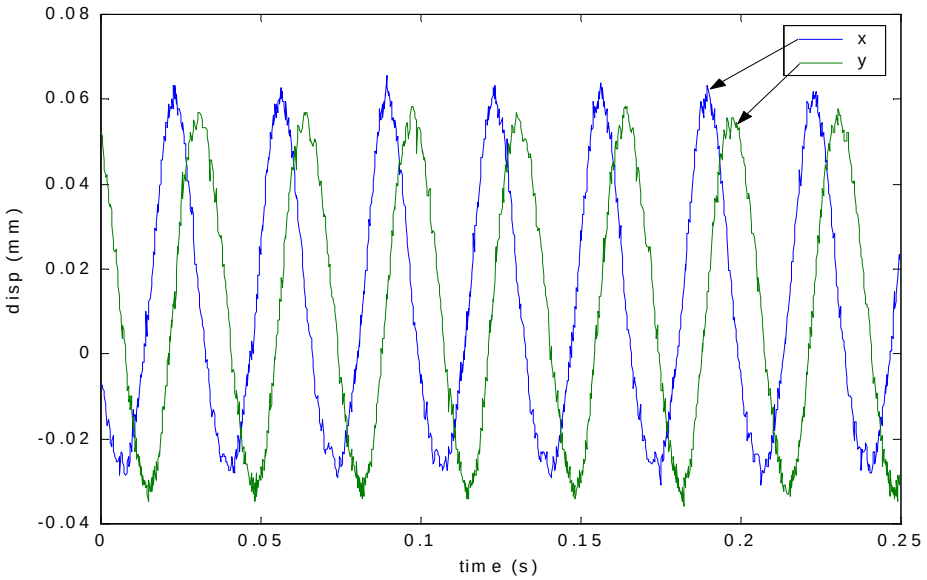

Figure 5.2: Horizontal and vertical eddy-current position measurements
(1.6 g unbalance at 90°, 1800 RPM, 1.0 A top bias)

Figure 5.3 shows the top and bottom coil currents for the two axes of one bearing. The two top current waveforms are 90° out of phase since the two axes of actuation are 90° apart. The top and bottom current waveforms for each axis are 180° out of phase, causing a maximum for the top current waveform to correspond to a minimum in the bottom current signal. Upon inspection of the position and coil current plots however, a simplification procedure was developed that would allow for the calculation of the dynamic bearing force.

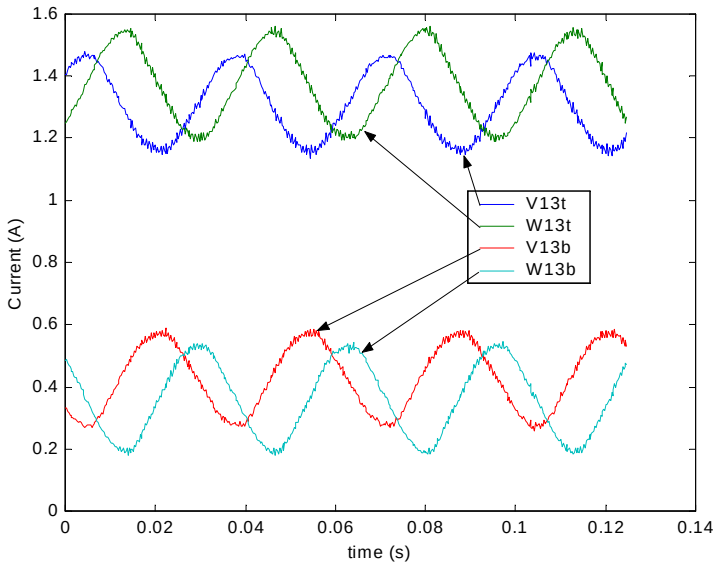

Figure 5.3: Current Waveforms
(1.6 g unbalance at 90°, 1800 RPM, 1.0 A top bias)

When the rotor is stationary and not rotating, the static weight of the rotor generates DC currents in the actuators to levitate it. When the rotor is spinning and not balanced, dynamic forces develop according to

$$F = me\omega^2 \tag{5.1}$$

where m is the amount of unbalanced mass, e is the distance of the unbalance mass from the center of rotation, and ω is the rotational speed of the rotor. Since the rotor is spinning below its first critical speed during this test, the mid-span mass is whirling in a steady orbit that is at a frequency predominantly synchronous to the running speed of the rotor. As the mass whirls through its orbit, the bearings have to support different forces. When the mass is at the bottom of the orbit, the dynamic loading is aligned with the static weight and the bearings must support loads in excess of the rotor weight. When the mass is at the top of its orbit, the rotor weight is against the dynamic load and the bearing load is less than the static weight. Because the force applied by the bearings is directly related to current, an estimate of the dynamic bearing load can be construed from the current waveforms. One of the current waveforms is shown in the left pane of Figure 5.4. The DC offset of the signal is due to the rotor weight, and the alternating component shows the dynamic loading being applied to the bearing. The autospectrum of the current waveform is presented in the right pane of Figure 5.4, and the two frequency components are 1.5 A @ 0 RPM and 0.12 A @ 1800 RPM.

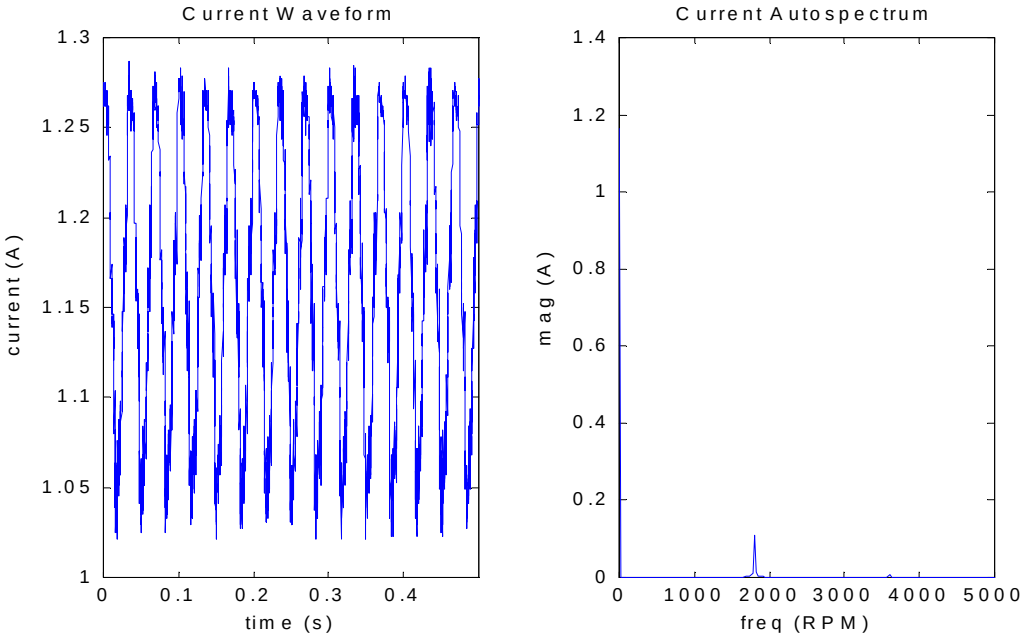

Figure 5.4: Current waveform and associated autospectrum

These two components can be manipulated in order to determine the maximum, minimum and average values of the current signal. If the AC component is added to the DC component, the maximum current value is calculated. By subtracting the AC component from the DC value, the minimum current is found. If the DC values are used for all actuators in the multi-point algorithm, the static weight of the rotor should be predicted. Additionally, by using different combinations of minimum and maximum currents for the actuators in the multi-point program, the maximum and minimum applied force can be calculated. These forces are composed of rotor whirl (unbalance), shaft bow, and static rotor weight. Below the first critical speed, the maximum calculated force is required as the rotor whirls through the bottom of its orbit, when the rotor weight is in line with the unbalance load. Since the rotor is at the bottom of the bearing, the top actuators require more current because the air gaps have been increased and the force is directly opposing them. Therefore, to predict the maximum force for a vertical axis, the maximum current is assumed for the top currents, and the minimum currents assumed for the bottom actuator. This calculation technique is performed by manually combining the various components for the different actuators. The weight of the rotor is opposite in direction to the unbalance load and the actuator force is at a minimum as the rotor reaches the top of its orbit. Half of the difference between the maximum and minimum force values will be referred to as the alternating force, and is the magnitude of the cyclical force that changes as the rotor spins.

To predict the force being applied by a two-axis bearing requires several more steps, however. For a single axis, the procedure outlined above is sufficient, but this method cannot be directly applied to a bearing with two different axes of actuation. The angular difference in the axes causes a phase shift between them and this prevents the use of the previous method because the peak current values do not occur at the same moment in time. To apply the autospectrum method blindly to a dual-axis bearing would produce erroneously high force predictions by finding the maximum and minimum forces for each axis despite the phase difference between the two axes. In order to correctly predict the maximum and minimum force applied by a multi-axis bearing, the two top current signals have to be averaged. This technique essentially combines the two axes into one, finds the

desired information, and then assigns equivalent values back to the two separate axes. By applying Equation (5.2), a weighted average signal can be generated from the two original signals. The two currents, I_1 and I_2, represent either the two top or the two bottom halves of the two actuators.

$$I_{avg} = \left(\frac{I_1^2}{2} + \frac{I_2^2}{2} \right)^{1/2} \tag{5.2}$$

This new "average" value can be used in place of the two original signals to arrive at a force prediction. Figure 5.5 shows a plot of two current signals and the calculated "average" current.

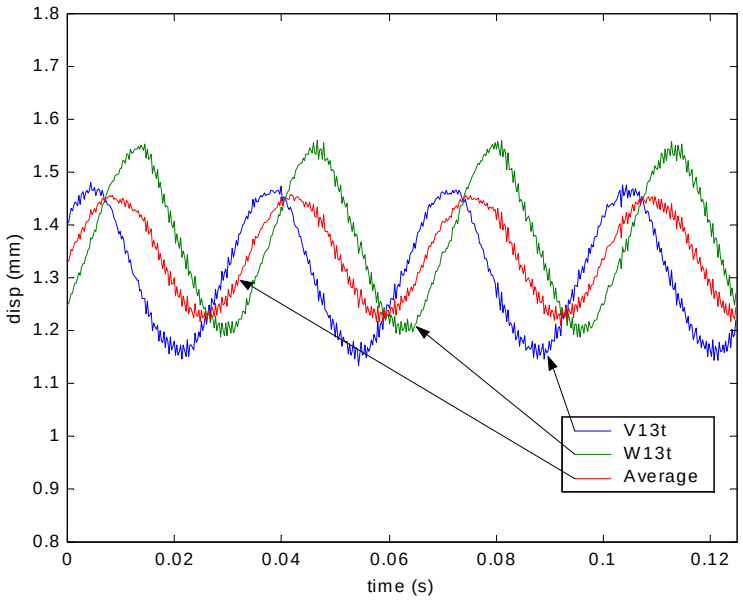

Figure 5.5: Top currents and the average waveform

When performed on a coupled set of top and bottom currents, the two average waveforms maintain the expected 180° phase shift. After performing the conversion, the autospectrum of the average waveform will yield usable information. The approach for a single-axis bearing can then be applied, using the calculated average values instead of the actual ones. The advantage of using this approach is that a single axis can be analyzed

instead of both. Equations (5.3) and (5.4) show the formulas used to test the validity of this claim. Equation (5.3) uses both axes and the associated current measurements for each. Equation (5.4), however, uses the average current values for one axis and doubles the force predicted by it since the two axes are equivalent after the averaging process.

$$F_{act} = \left(\left(1.248^2 - 0.492^2\right) + \left(1.400^2 - 0.342^2\right)\right)\sin(45^\circ) \tag{5.3}$$

$$F_{app} = 2\left(1.326^2 - 0.424^2\right)\sin(45^\circ) \tag{5.4}$$

Table 5.1 shows the current values used in this test and the predicted forces by each approach. The two methods produce force predictions within 0.05% difference, well within the current limits of the multi-point method.

Table 5.1: Current approximation test case

	Actual		Approximation	
Axis	V13	W13	V13	W13
Top (A)	1.248	1.400	1.326	1.326
Bottom (A)	0.492	0.342	0.424	0.424
Pred. Force, N (lbf)	9.933 (2.233)		9.928 (2.232)	

Figure 5.6 shows a plot comparing the predicted forces using the original single-axis autospectrum method and the new averaged current method. The data marked with points are the predictions using the old method, where the line shows the new predictions. Because the old method used current values obtained from different points in time, the predicted forces are significantly higher than the new method's predictions. Also plotted is the theoretical dynamic force that should result from the rotor speed and unbalance condition according to Equation (5.1). Notice that the old method predicts too much dynamic force for the known amount of unbalance, while the new average technique lies on top of the theoretical prediction. The dependency on unbalance location of the dynamic force predictions is due to interaction between the unbalance and shaft bow. This is discussed in detail in the following section.

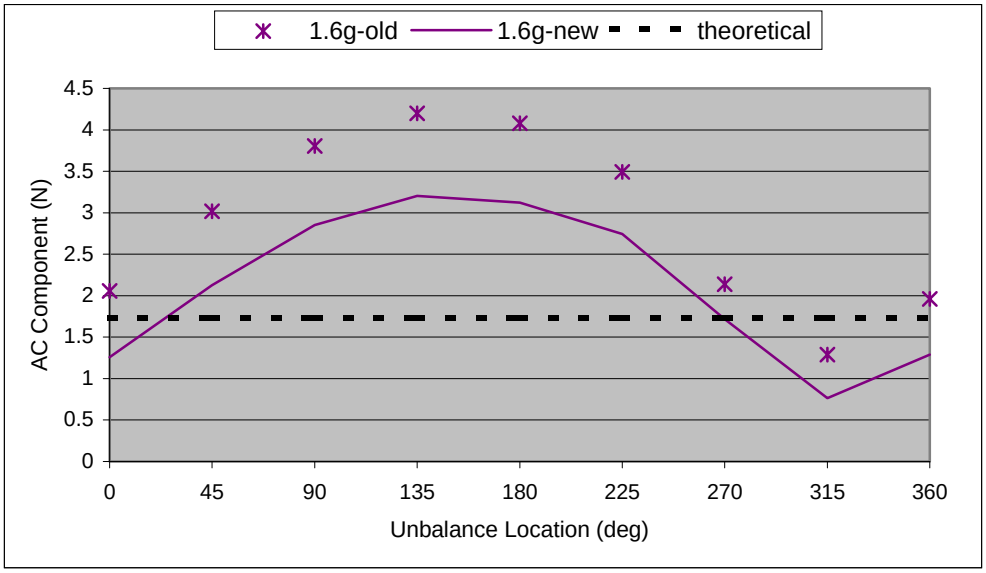

Figure 5.6: Comparison of two dynamic force prediction techniques and calculated theoretical value (1800 RPM)

One potential problem inherent with this method is that it makes use of the autospectrum of current signals. Depending on the sampling frequency and the number of samples taken by the data acquisition system, the autospectrum is broken into discrete frequency intervals. When a signal is oscillating at a well-defined frequency that corresponds to one of these intervals, the autospectrum will show a sharp peak. However, if the operating frequency is between intervals, or if it is changing, the energy is spread over several frequency bands. This causes a reduction in the magnitude of the peak, which would cause an error in the calculation of the maximum and minimum currents by the autospectrum method. During the experimental testing, the rotor speed was matched with the data acquisition parameters in order to give sharp, well-defined peaks when converted into the frequency domain. In situations where the operating frequency is changing or has significant background noise, the autospectrum method could be problematic. Most rotating machinery operates at a steady speed that will eliminate this type of error. Additionally, if the operating frequency is known, the data acquisition can be fine-tuned to provide good results. This limitation should be understood, so that its effects can be avoided.

5.4 Preliminary Tests

The dynamic testing of the AMBs entails much more difficulty than in the previous static work. Many effects do not manifest themselves when operating on a static level, but must be considered when dealing with a dynamic scenario. Hysteresis and eddy currents are both well-known complications when attempting dynamic force measurement, but are beyond the scope of this project. In addition, Nicholas, et. al. (1976) show that shaft bow can play a particularly large role in the behavior of rotating machinery and with the small shaft used in the testing, shaft bow was a problem. A series of initial trials were devised in order to determine the condition of the rotor system.

In order to quantify the shaft bow and its influence on additional unbalance, a test was conducted that measured the force due to additional unbalance added at different angular locations around the midspan disk. As expected, the forces varied as the unbalance was moved relative to the shaft bow. Figure 5.7 shows the algorithm-calculated alternating forces using the average-current autospectrum method due to 1.0 grams of unbalance while rotating at 1800 RPM.

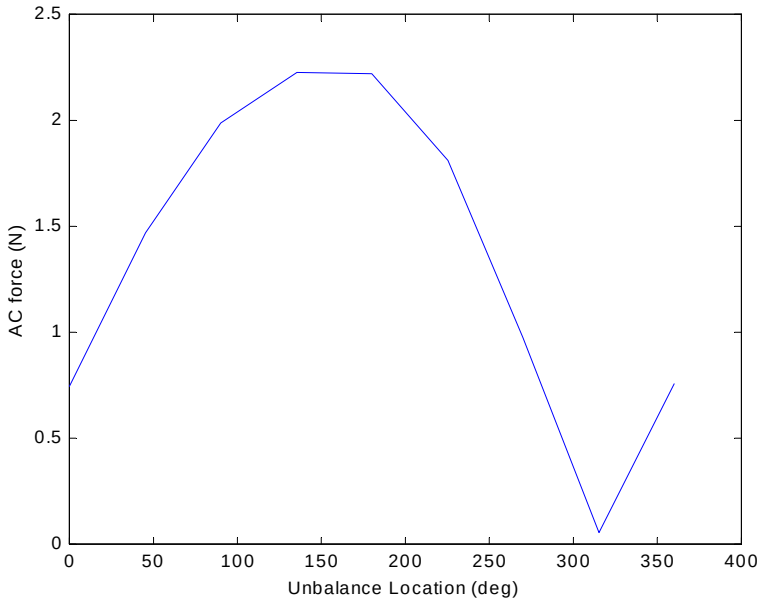

Figure 5.7: Alternating force component vs. unbalance location
(1.0 g, 1800 RPM)

From inspection, it is clear that the shaft bow is aligned with the 135° angular location mark on the rotor. When the unbalance is added to this position, it works with the shaft bow to create large bearing forces. By moving the unbalance 180°, into the 315° position, it works against the shaft bow and produces very little alternating force.

A computer program was written to separate shaft bow and unbalance effects from the data already collected. By assuming that the shaft bow imparts a certain force in a fixed direction (135°) and that the unbalance force is known and changes direction based on its angular location, the two can be added in a vector sum to create a crude model of the rotor. The force imparted by the shaft bow was calculated by taking an average of the alternating forces without any additional unbalance on the rotor. The basic formula that relates speed to force due to unbalance is given by Equation (5.1).

$$F = me\omega^2 \tag{5.1}$$

By using the known values for the parameters in Equation (5.1), the unbalance force was determined. With these values and the assumed shaft bow forces, the model was run and compared to the measured experimental values, but the two did not match well. By manually adjusting the values governing the forces due to shaft bow and unbalance within the model, the predicted rotor forces were made to match the experimentally determined forces. Table 5.2 gives the theoretical force values and the modified values that give the best fit. Figure 5.8 shows a plot of the experimental data, the theoretical model, and the model after it was modified to fit the data.

Table 5.2: Theoretical and modified force values

Unbalance Case	Theoretical (lbf)		Modified (lbf)	
	Shaft Bow	Unbalance	Shaft Bow	Unbalance
1.0 g	0.237	0.244	0.35	0.34

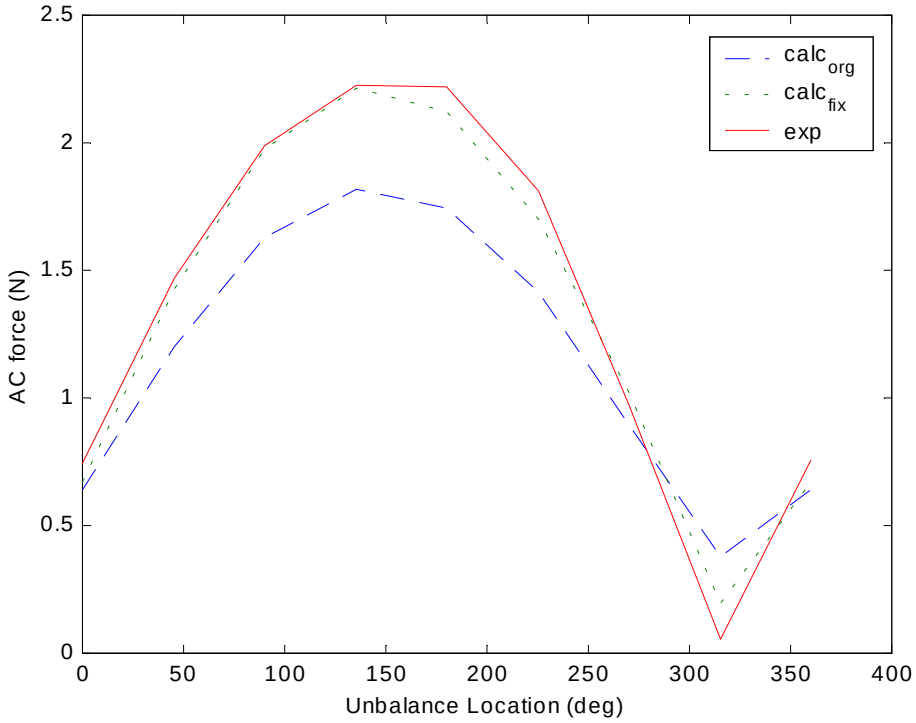

Figure 5.8: Plot of experimental forces vs. theoretical and modified models

By performing this on several data sets, there was little consistency in the modified values for the shaft bow. While this appears troubling, the shaft used during testing was small and flexible, and a change in the shaft bow would not be surprising. Since the shaft bow value was determined using a balanced rotor, adding unbalance could cause further bending of the rotor that would increase the unbalance forces. There was inconsistency in the modified unbalance values as well. More unbalance was needed in all of the trials than theoretically predicted for the model to agree with experimental data, but the amount of increase in the unbalance value was not consistent. This agrees with the previous explanation, where a portion of the additional shaft bow is being accounted for by the modified unbalance values. Ultimately, this approach was not very successful, and is presented only for completeness for future studies.

5.5 Test Configurations

The objectives of the dynamic testing were to determine if the multi-point algorithm could accurately determine the forces generated in a rotating scenario. The two

largest constituents of this force are the rotor weight (the DC component) and the unbalance forces (the synchronous component from the shaft bow and additional unbalance weights). It was desired for the program to give accurate, precise force predictions regardless of the speed of the rotor or the amount of unbalance. In order to test this, different speeds and amounts of unbalance were used to create a matrix of combinations. The rotor speeds that were analyzed were 485 RPM, 1200 RPM, 1800 RPM, and 2400 RPM. All of these test speeds are below the first critical speed of the rotor, which was near 3200 RPM. There was a structural resonance in the horizontal direction only near 2700 RPM, which further limited the speed range of the tests. The different unbalance masses that were used were 0.0 g (balanced), 0.5 g, 1.0 g, and 1.6 g. The matrix of test combinations is shown in Table 5.3.

Table 5.3: Matrix of dynamic test combinations

		Rotor Speed			
		485	1200	1800	2400
Unbalance	0.0				
	0.5				
	1.0				
	1.6				

Because of the effect of angular location on the unbalance-induced dynamic loading due to shaft bow, another parameter was added to the tests. Each of the above mentioned tests were run multiple times, and the unbalance was added to different angular locations around the disk mass. The different angular locations used were θ_u = 90°, θ_u = 225°, and θ_u = 270°. These were chosen so that the unbalance would have varying influence on the rotor. From Figure 5.7, the locations were chosen to give an amplified affect (90°), a reduced affect (270°), and a median affect (225°).

The different unbalance load and rotor speed combinations were tested in the following order. For a given unbalance location, θ_u, and a given unbalance mass, the rotor was driven at the test speeds, and the current and position measurements were recorded. The unbalance mass was then increased to the next level, and the different rotor speeds were again tested. After the maximum unbalance mass was tested, the

process was repeated with a different angular unbalance location. At the beginning of each series of angular location tests, the different rotor speeds were tested without any additional unbalance to monitor the amount of shaft bow present in the rotor. Since there was no additional mass added, any dynamic forces calculated for these trials would be due only to the shaft bow.

5.6 Dynamic Test Results

Tables 5.4-5.6 present the multi-point force predictions for the dynamic test configuration. Each of the tables summarizes the unbalance and rotor speed combinations for a particular unbalance location. For each combination of unbalance and rotor speed, three force predictions are presented. The DC force predictions utilized only the DC components of the current waveforms and represent the static weight of the rotor. The minimum and maximum force predictions were calculated using the average-current method described in Section 5.3. The AC force was calculated from the maximum and minimum force predictions and is half of the difference between the two predictions. For example, when 1.0 g of unbalance is added at $\theta_u = 90°$, the minimum and maximum predicted forces at 1800 RPM are 14.10 N and 18.17 N, respectively. The static weight prediction for that case is 16.19 N, and the dynamic force is 2.033 N. In physical terms, when the bearings are operating under these conditions, they continually support 16.19 N and there is a periodic force of 2.033 N that cycles synchronously with the rotor speed. The DC force predictions should be independent of all three test parameters, but there was some variation as the different combinations were tested.

Table 5.4 summarizes the results of the dynamic testing with unbalance placed at 90°. For each unbalance case, as speed increases, several trends are apparent. The low values predicted by the multi-point code decrease as speed increases, because as the dynamic forces increase (proportionally to rotor speed squared, as shown in Equation (5.1)), it can balance more of the rotor weight when the two forces are opposing. For the 1.0 g case, the low forces vary from 15.52 N to 12.21 N as the rotor speed increases from 485 RPM to 2400 RPM. The high values increase with speed because they are calculated when the dynamic and static forces combine. The high forces increase from 16.46 N to

20.52 N over the tested speed range. The AC force is the dynamic component of the predicted forces and is half of the difference between the high and low predicted forces. These increase with rotor speed and are the variable of interest for later analysis. The 1.0 g dynamic forces increase from 0.469 N to 4.154 N and represent the component of the force that alternates in direction as the rotor rotates.

Table 5.4: Dynamic Results, $\theta_u = 90°$

	Speed, RPM	Low-Value, N (lbf)	DC-Value, N (lbf)	High-Value, N (lbf)	AC, N (lbf)
0.0 g	485	15.71 (3.53)	16.07 (3.61)	16.40 (3.69)	0.345 (0.08)
	1200	15.70 (3.53)	16.11 (3.62)	16.48 (3.70)	0.387 (0.09)
	1800	15.60 (3.51)	16.16 (3.63)	16.71 (3.76)	0.556 (0.13)
	2400	15.37 (3.46)	16.27 (3.66)	17.14 (3.85)	0.883 (0.20)
0.5 g	485	15.63 (3.51)	16.09 (3.62)	16.54 (3.72)	0.454 (0.10)
	1200	15.29 (3.44)	16.11 (3.62)	16.87 (3.79)	0.792 (0.18)
	1800	14.64 (3.29)	16.13 (3.63)	17.53 (3.94)	1.448 (0.33)
	2400	13.81 (3.10)	16.38 (3.68)	18.78 (4.22)	2.489 (0.56)
1.0 g	485	15.52 (3.49)	16.00 (3.60)	16.46 (3.70)	0.469 (0.17)
	1200	15.29 (3.44)	16.15 (3.63)	16.96 (3.81)	0.838 (0.19)
	1800	14.10 (3.17)	16.19 (3.64)	18.17 (4.08)	2.033 (0.46)
	2400	12.21 (2.75)	16.52 (3.71)	20.52 (4.61)	4.154 (0.93)
1.6 g	485	15.67 (3.52)	16.12 (3.62)	16.54 (3.72)	0.438 (0.10)
	1200	15.11 (3.37)	16.27 (3.66)	17.36 (3.90)	1.128 (0.25)
	1800	13.69 (3.08)	16.45 (3.70)	19.00 (4.27)	2.655 (0.60)
	2400	9.93 (2.23)	17.07 (3.83)	23.87 (5.37)	6.970 (1.57)

Table 5.5 presents the results of the dynamic testing with unbalance at 225°. The trends for the low, high, and AC forces are the same as in the previous table. However, the predicted forces do not vary as much with rotor speed as in the previous case. For 1.0 g of unbalance, the dynamic forces range from 0.387 N to 3.861 N, where they varied from 0.469 N to 4.154 N when the unbalance was placed at 90°. This difference is due to the shaft bow/unbalance interaction mentioned previously and is further analyzed in later sections.

Table 5.5: Dynamic Results, $\theta_u = 225°$

	Speed, RPM	Low-Value, N (lbf)	DC-Value, N (lbf)	High-Value, N (lbf)	AC, N (lbf)
0.0 g	485	15.84 (3.56)	16.17 (3.64)	16.49 (3.71)	0.327 (0.07)
	1200	15.80 (3.55)	16.32 (3.67)	16.80 (3.78)	0.500 (0.11)
	1800	15.69 (3.53)	16.37 (3.68)	17.02 (3.83)	0.665 (0.15)
	2400	15.32 (3.44)	16.41 (3.69)	17.45 (3.92)	1.065 (0.24)
0.5 g	485	15.74 (3.54)	16.12 (3.62)	16.49 (3.71)	0.374 (0.08)
	1200	15.71 (3.53)	16.29 (3.66)	16.85 (3.79)	0.572 (0.13)
	1800	15.25 (3.43)	16.40 (3.69)	17.54 (3.94)	1.145 (0.26)
	2400	14.14 (3.18)	16.43 (3.69)	18.81 (4.23)	2.331 (0.52)
1.0 g	485	15.79 (3.55)	16.18 (3.64)	16.56 (3.72)	0.387 (0.09)
	1200	15.53 (3.49)	16.29 (3.66)	17.05 (3.83)	0.763 (0.17)
	1800	14.44 (3.25)	16.36 (3.68)	18.34 (4.12)	1.953 (0.44)
	2400	12.69 (3.85)	16.48 (3.71)	20.41 (4.59)	3.861 (0.87)
1.6 g	485	15.80 (3.55)	16.17 (3.64)	16.54 (3.72)	0.367 (0.08)
	1200	15.24 (3.43)	16.29 (3.66)	17.33 (3.90)	1.045 (0.24)
	1800	13.70 (3.08)	16.36 (3.68)	19.08 (4.29)	2.691 (0.61)
	2400	11.01 (2.48)	16.65 (3.74)	22.47 (5.05)	5.729 (1.29)

The dynamic test results with the unbalance located at 270° are presented in Table 5.6. This particular unbalance location created some interesting force trends. For the previous two cases, the dynamic forces increased with rotor speed. Although the rate of increase varied, the trend was correct. Because of the interaction between the shaft bow and unbalance in this case, however, there were unbalance cases where an increase in rotor speed caused a decrease in the predicted dynamic force. The dynamic forces predicted for the 1.0 g unbalance case were 0.320 N, 0.207 N, 1.139 N, and 3.020 N as the rotor speed increased from 485 RPM to 2400 RPM. The dip in the dynamic loads was unique to this unbalance location and is discussed in further details later in this section.

Table 5.6: Dynamic Results, $\theta_u = 270°$

	Speed, RPM	Low-Value, N (lbf)	DC-Value, N (lbf)	High-Value, N (lbf)	AC, N (lbf)
0.0 g	485	15.75 (3.54)	16.16 (3.63)	16.54 (3.72)	0.398 (0.09)
	1200	15.75 (3.54)	16.32 (3.67)	16.88 (3.80)	0.567 (0.13)
	1800	15.67 (3.52)	16.37 (3.68)	17.01 (3.83)	0.672 (0.15)
	2400	15.36 (3.45)	16.43 (3.69)	17.46 (3.93)	1.050 (0.24)
0.5 g	485	15.84 (3.56)	16.21 (3.64)	16.56 (3.72)	0.356 (0.08)
	1200	15.96 (3.59)	16.31 (3.67)	16.64 (3.74)	0.342 (0.08)
	1800	16.07 (3.61)	16.41 (3.69)	16.77 (3.77)	0.351 (0.08)
	2400	15.02 (3.38)	16.43 (3.69)	17.90 (4.02)	1.441 (0.32)
1.0 g	485	15.85 (3.56)	16.17 (3.64)	16.49 (3.71)	0.320 (0.07)
	1200	16.13 (3.63)	16.35 (3.68)	16.54 (3.72)	0.207 (0.05)
	1800	15.28 (3.44)	16.40 (3.69)	17.56 (3.95)	1.139 (0.26)
	2400	13.47 (3.03)	16.48 (3.70)	19.51 (4.39)	3.020 (0.68)
1.6 g	485	15.88 (3.57)	16.19 (3.64)	16.48 (3.71)	0.300 (0.07)
	1200	16.09 (3.62)	16.29 (3.66)	16.49 (3.71)	0.200 (0.05)
	1800	14.67 (3.30)	16.40 (3.69)	18.15 (4.08)	1.741 (0.39)
	2400	12.52 (2.81)	16.60 (3.73)	20.66 (4.65)	4.072 (0.92)

The first analysis performed on the data was done on the static weight (DC-force) predictions. The measured static rotor weight was 15.63 N (3.51 lbf). The static force predictions should not be influenced by unbalance or rotor speed. The addition of balance weights to induce the dynamic forces will change the rotor weight slightly, but this was neglected since the largest balance weight increased the total rotor weight by only 0.13%. Figure 5.9 shows a plot of the DC force predictions from the multi-point algorithm for all of the test cases against rotor speed. There appears to be some rotor speed or rotor speed squared influence, but the curve fit r^2-values of 0.54 and 0.55 proves they are only a weak dependence. When plotted against the additional unbalance magnitude, the r^2-value drops to 0.08. The variation in the force predictions is not from either of the experimental variables, meaning that it is likely random noise in the data from the trials.

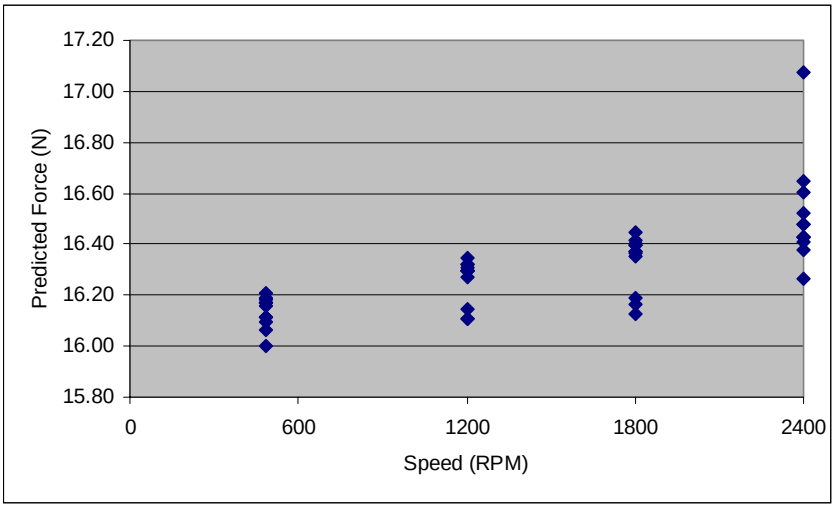

Figure 5.9: Static force predictions vs. rotor speed

The same performance metrics used in the static testing can be applied to this static weight data set to determine the effectiveness of this approach. The percent error of the overall DC prediction average was 4.35% and the percent spread of the data was 6.83%. Table 5.7 summarizes the percent error and percent spread for the dynamic tests at each unbalance location. These results were on the same order of magnitude as the other static predictions from Chapter 4 and proved that the dynamic multi-point algorithm was performing as intended. The ability of the multi-point algorithm to separate the static load from a dynamic scenario could be very useful in manufacturing applications such as micro-fiber production where the static tension in the fiber is important.

Table 5.7: Summary of percent error and spread for static weight predictions

	90°	225°	270°	Overall
Percent Error	4.00	4.48	4.57	4.35
Percent Spread	6.83	3.41	2.85	6.83

In addition to the multi-point predictions, single-point predictions of the static rotor weight were made as well. As in the static configurations, Equation (1.7) was used to generate the single-point predictions. The DC components of the coil currents were used in the force relationship. Although the shaft exhibited a strong first mode shape, the bearing rotors were assumed to remain centered in the stators. Table 5.8 presents several

examples of the single-point force predictions as well as the equivalent multi-point predictions. The derating factor from static test #2, ε=0.824, was used as the derating factor for the single-point predictions in this test, since its double bearing configuration most closely resembled the rotor arrangement used in the dynamic test.

Table 5.8: Examples of single-point and multi-point static weight predictions (weight of components = 16.17 N)

Unbalance Conditions	Multi-Point, N (lbf)	Single-Point, N (lbf)
0.5 g @ 90°, 1200 RPM	16.11 (3.62)	20.25 (4.55)
1.6 g @ 90°, 2400 RPM	17.07 (3.83)	20.40 (4.59)
1.0 g @ 225°, 1800 RPM	16.36 (3.68)	20.27 (4.56)
0.5 g @ 225°, 485 RPM	16.12 (3.62)	20.16 (4.53)
0.5 g @ 270°, 1800 RPM	16.41 (3.69)	20.40 (4.59)
1.6 g @ 270°, 1200 RPM	16.29 (3.66)	20.37 (4.58)
Percent Error	1.38	25.59
Percent Spread	5.94	1.48

The percent error and percent spread values shown in Table 5.8 are based on the mechanical weight of the rotor components used in the dynamic test. The interaction with the motor was not modeled and its influence on the static force predictions is not known. However, lacking further information, the measured weight of 16.17 N was used to illustrate the differences in the multi-point and single-point predictions. The single-point force predictions were very consistent, showing only 1.48% spread over the selected cases. The multi-point predictions showed a percent spread of 5.94%. However, the magnitude of the predictions was significantly different. The multi-point predicted average force was 16.39 N, while the single-point average was 20.31 N. The percent errors for the two averages are 1.38% and 25.59%, respectively. While the true value of the static load may not be known, the motor is probably supporting a portion of the component weight, meaning the correct prediction is likely less than 16.17N. The important feature of this table is the large difference in the predictions between the two methods, and the multi-point prediction is closer to the likely actual static weight than the single-point method.

Figure 5.10 shows a graphical representation of the multi-point static force predictions for the dynamic test. The solid line represents the weight of the rotor components, and the data points show the average static force predictions for each of the four tested rotor speeds. The error bars represent the maximum and minimum predictions for each of the test speeds. For the first three speeds, the average predictions are very close to the measured rotor weight. However, the motor interaction was not modeled and may influence the "actual" rotor weight. The error bars appear to get larger as speed increases, meaning that there is larger variation in the predictions at higher speeds.

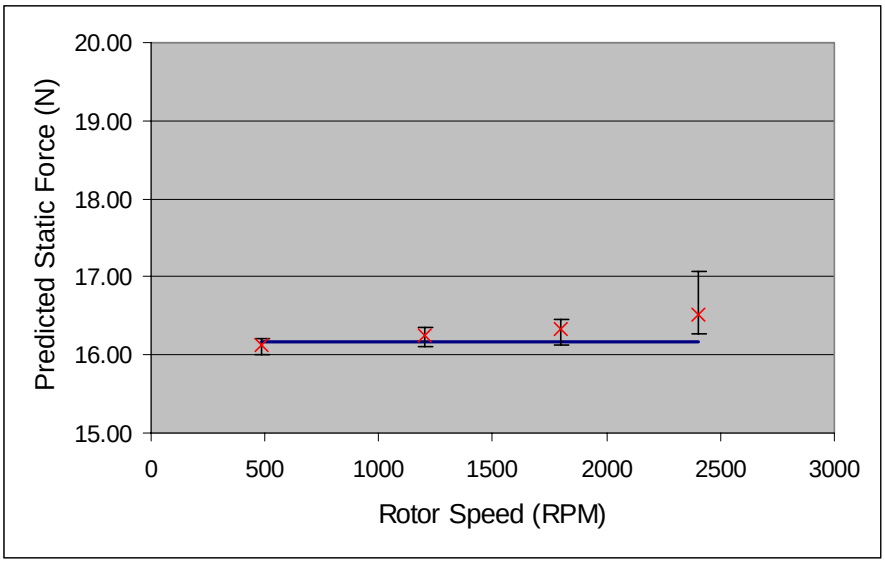

Figure 5.10: Multi-point max-min-average plot (dynamic test static predictions)

Several trends become apparent when the AC data is plotted against different axes. By plotting the AC force prediction against unbalance mass, a linear plot is expected. That is, for each distinct speed, the amount of unbalance mass should be directly proportional to the dynamic force supported by the AMB according to Equation (5.1). Figure 5.11 shows this plot for 2400 RPM. For both the 90° and 225° cases, the plots are linear, as expected. However, for the 270° case, the plot is nearly flat from 0 g to 0.5 g, then continues with the linear trend demonstrated by the other two cases. This bend in the plot is most likely due to the interaction of the unbalance with the shaft bow.

At 2400 RPM, 0.5 g of unbalance counteracts the dynamic bow effect, but the rotor responds as expected as additional unbalance is added.

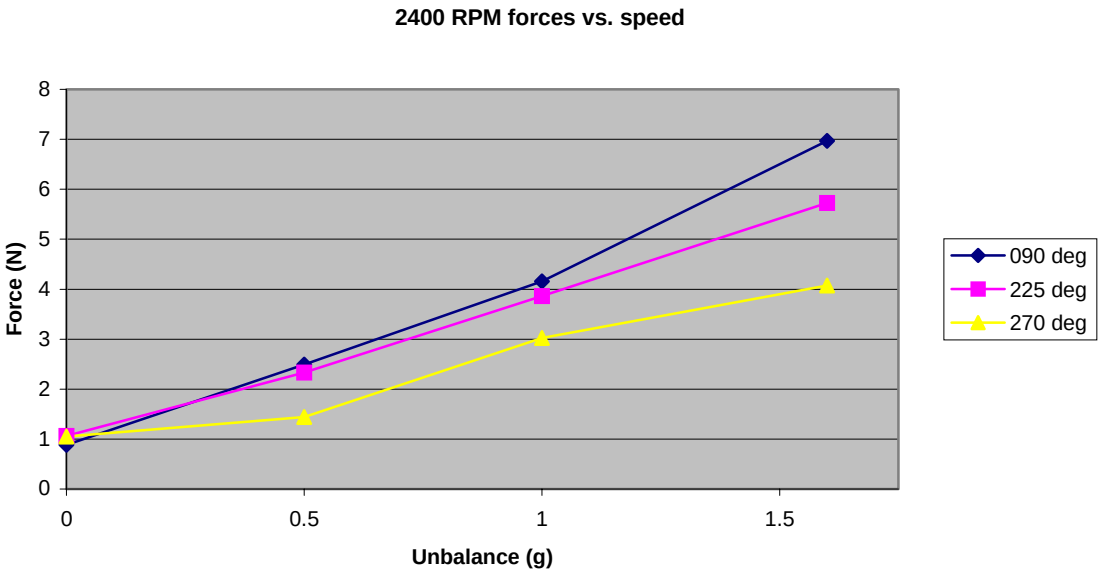

Figure 5.11: Alternating force vs. unbalance (2400 RPM)

At 1800 RPM, as shown in Figure 5.12, 0.5 g of unbalance at 270° almost completely balances the rotor with respect to dynamic forces. The rest of the data at that speed shows the same expected linear response to unbalance.

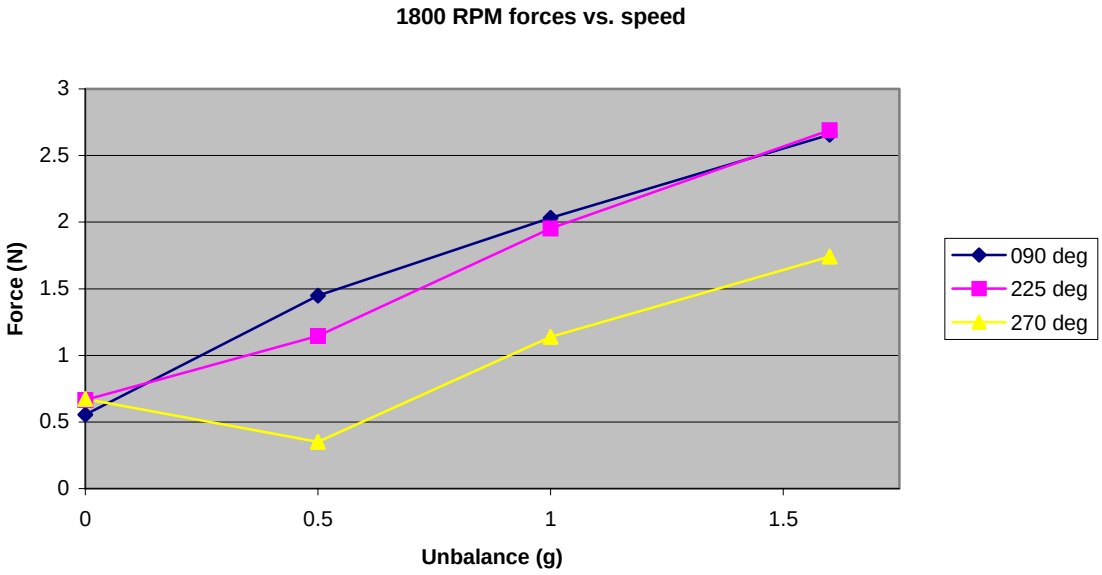

Figure 5.12: Alternating force vs. unbalance (1800 RPM)

Figure 5.13 shows the same plot for a rotor speed of 1200 RPM. At the slower speed, it requires more added unbalance to counter the shaft bow, which causes the negative slope for all of the 270° data. The 90° and 225° data do not appear to be as linear as the other plots, but this is likely random noise in the data. Since the force generated by unbalance increases proportionally to rotor speed squared, a reduction in speed greatly reduces the dynamic forces on the bearings. Because the experimental variations in the predicted forces are similar for all of the dynamic tests, the smaller dynamic forces in the 1200 RPM tests cause them to appear larger than in the other cases.

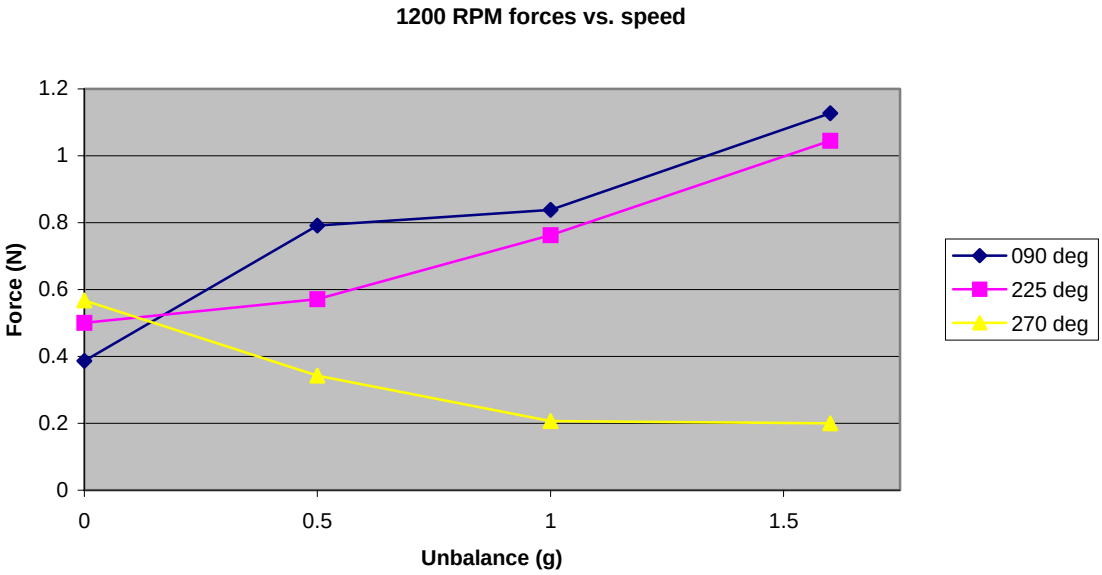

Figure 5.13: Alternating force vs. unbalance (1200 RPM)

Another trend that can be observed in the experimental data is the influence of speed on the dynamic loads supported by the magnetic bearings. According to Equation (5.1), for a given eccentric unbalance, if the rotational velocity increases by a factor of two, the dynamic load will increase by a factor of four. By plotting the dynamic forces predicted by the multi-point algorithm against the rotor speed, this quadratic relationship should be apparent.

Figure 5.14 shows the relationship between dynamic force and speed for the case with no additional unbalance. The rotor was dynamically balanced before any of the dynamic tests were conducted, and the balanced load cases were simply this balanced rotor without additional unbalance. The different data set labels (90°, 225°, and 270°) are representative of the order they were taken. As described in Section 5.5, the balanced tests were conducted as the first trial for each unbalance location. The various unbalance mass amounts were then tested at that location before continuing to the next angular location. Because of this testing order, the amount of shaft bow could have changed from test to test, and explains the variation between the sets, which should be identical. The figure also shows that there is some speed dependence in the data. This is due to the

previously mentioned shaft bow and residual rotor unbalance that is present in the experimental setup.

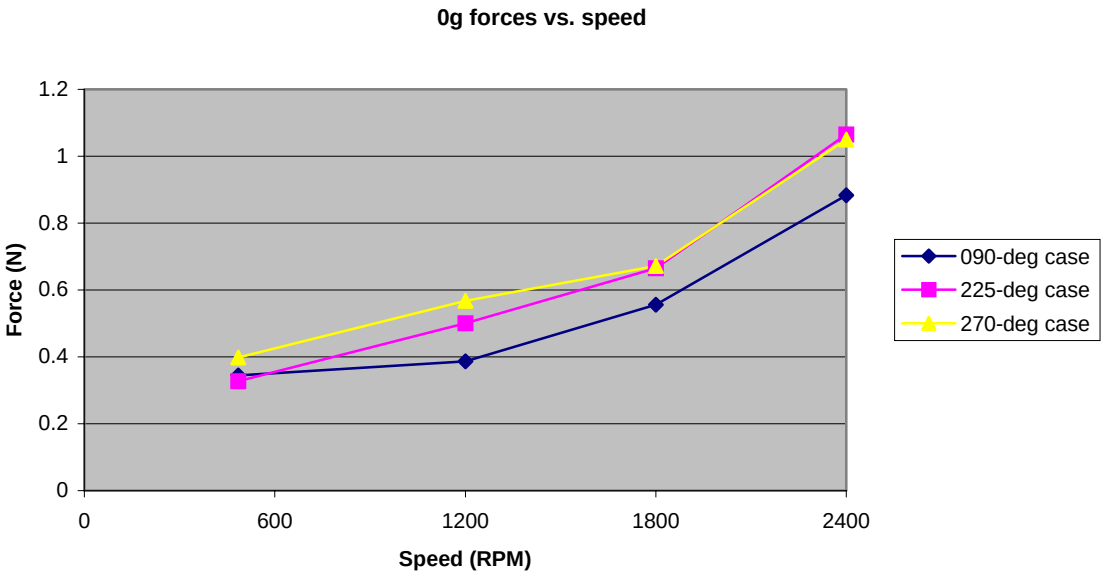

Figure 5.14: Alternating force vs. speed (0 g unbalance)

Figure 5.15 shows the force vs. speed plot when 0.5 g of unbalance is added. The three curves reflect the differences caused by adding the unbalance in different locations. For two of the cases, 90° and 225°, the curves do follow a general quadratic trend that is examined in more detail in a later section. The third case, 270°, again shows the results of the bow-unbalance interaction. At speeds below 1800 RPM, the 0.5 g unbalance mass is effectively canceled by the shaft bow, but at speeds above that the dynamic loading overpowers the shaft bow and causes additional dynamic forces.

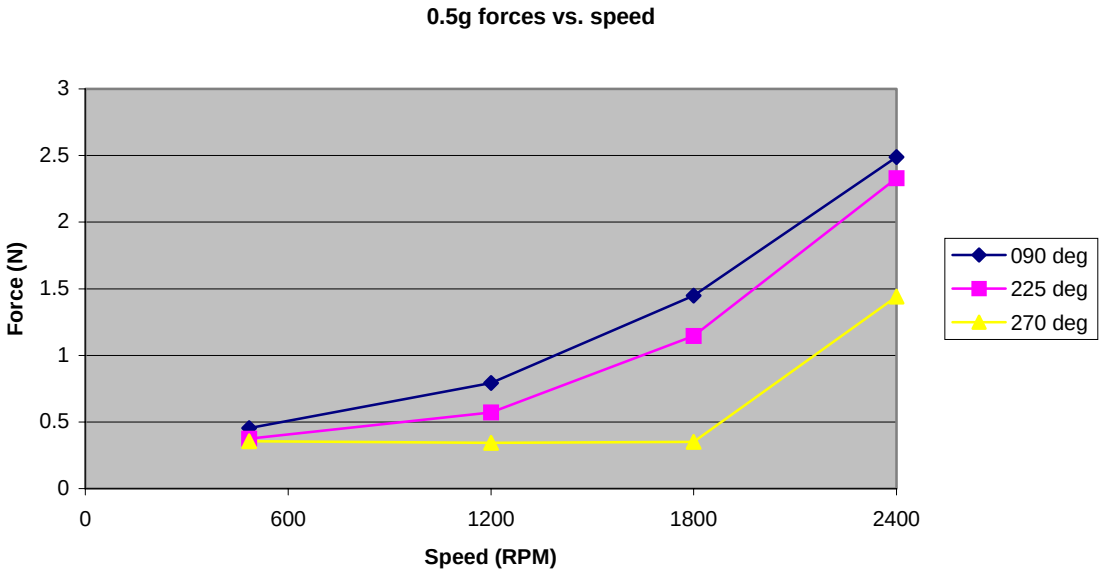

Figure 5.15: Alternating force vs. speed (0.5 g unbalance)

Figures 5.16 and 5.17 show similar results as Figure 5.15. The 90° and 225° cases follow a quadratic trend, and the 270° case shows a distinct minimum before increasing. While the trends are similar, the dynamic force values do increase as the unbalance mass is increased, as shown above. The speed at which the 270° case shows its minimum does change, however. Because of the increase in unbalance mass, the speed required to balance the shaft bow effect is reduced as per Equation (5.1).

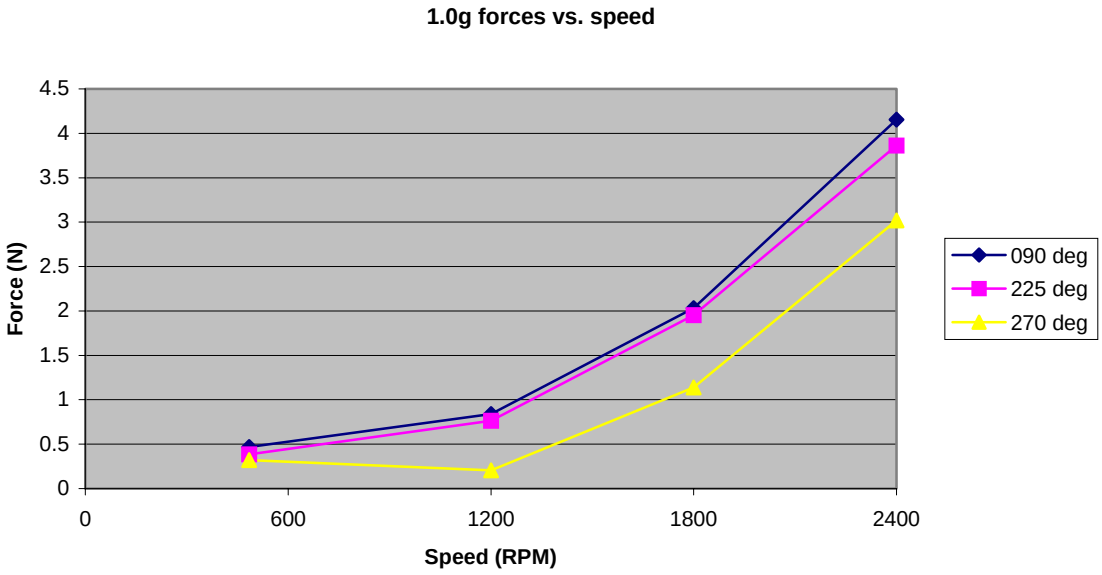

Figure 5.16: Alternating force vs. speed (1.0 g unbalance)

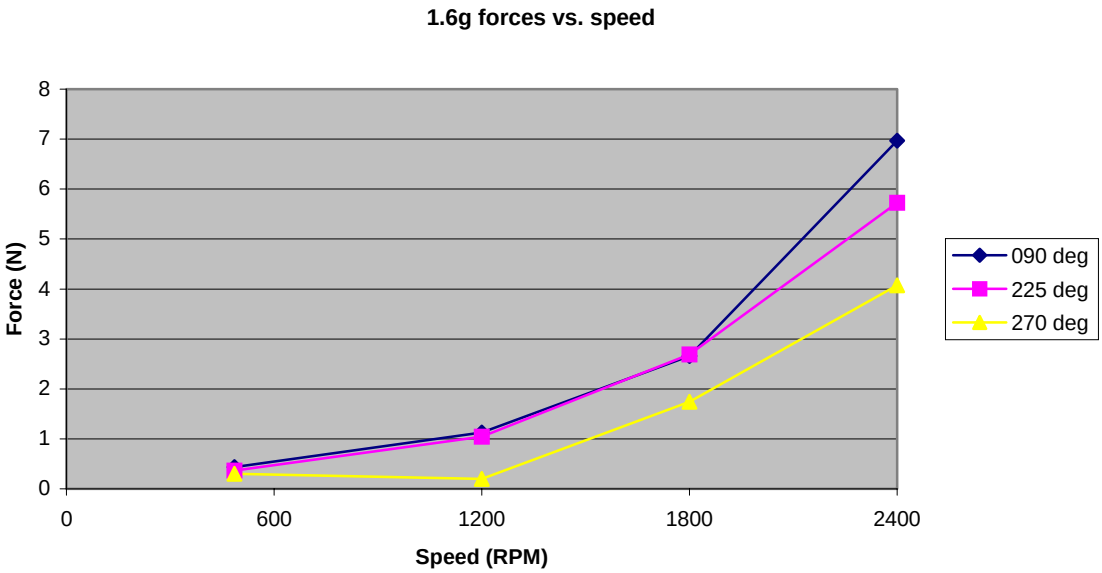

Figure 5.17: Alternating force vs. speed (1.6 g unbalance)

5.7 Quadratic Curve Fits

As discussed in the previous section, when the alternating unbalance force is plotted against the rotor speed, the resulting curve should follow a quadratic trend. To verify whether the predicted forces are following this relationship, a quadratic curve fit

was applied to the experimental data. A typical quadratic curve fit will have three variable parameters: the quadratic term, the linear term, and the constant term. However, for the data presented, only two parameters are required to model the data. If the slowest rotor speed is considered to have the minimum level of alternating force, then a simplifying assumption can be made. This "slow-roll" assumption is often made when analyzing vibration levels, and while not directly applicable to unbalance force, it is a reasonable assumption for a curve fit. Since the slow speed force is assumed to be the minimum level, it follows that the forces should grow proportionally to rotor speed squared. Under this modified quadratic model, the general curve is defined as

$$y_i = A(x_i - N_0)^2 + B \tag{5.5}$$

where A and B are parameters determined by the least-squares method; y_i is the alternating force that corresponds to the particular rotor speed, x_i; and N_0 is the slowest tested rotor speed. A small MATLAB program was written to solve the matrix equation defining the least-squares solution. For each combination of unbalance and unbalance location, this equation was solved to find the quadratic equation that best fits the experimental data. Table 5.9 summarizes the results of these fits. The first and second columns give the amount and location of unbalance added to the rotor. The third and fourth columns give the curve fit parameters, A and B, from Equation (5.5). The final column gives a measure of how well the fit matches the experimental data points. The measure that was chosen is the square root of the sum of the squares of the error ($\sqrt{SSE}$). This quantity is calculated by finding the difference between an experimental data point and the curve fit, squaring that difference, and then summing across all of the data points for each case, and then taking the square root of that value. By taking the square root of the SSE, the error units are force, and are easier to interpret. A perfect fit would give an $\sqrt{SSE}$ of zero, and the value increases as the curve deviates from the experimental data.

Table 5.9: Quadratic curve fit results

θ_u	Unbalance	A, N/RPM^2	B, N	$\sqrt{SSE}$, N
90°	0.0 g	1.494e-7	0.322	0.038
	0.5 g	5.493e-7	0.484	0.044
	1.0 g	1.017e-6	0.372	0.157
	1.6 g	1.781e-6	0.168	0.707
225°	0.0 g	1.925e-7	0.355	0.060
	0.5 g	5.380e-7	0.311	0.125
	1.0 g	9.581e-7	0.326	0.089
	1.6 g	1.464e-6	0.296	0.167
270°	0.0 g	1.672e-7	0.425	0.077
	0.5 g	2.996e-7	0.180	0.421
	1.0 g	7.812e-7	0.018	0.456
	1.6 g	1.094e-6	-0.037	0.490

The least-squares (LS) curve fits are shown plotted with the experimental data in Figures 5.18-5.20. For the plots, each particular data point style denotes a different amount of unbalance and the lines are the curve fits associated with the different unbalance tests.

The curve fits corresponding to the data taken with unbalance at 90° is shown in Figure 5.18. For the balanced case, and the 0.5g and 1.0g unbalance cases, the curve fits match the data very well. For the 1.6g set, however, it does not because the data appears to follow a trend closer to cubic than quadratic. This is not fully understood, but is possibly a result of a non-linear amplification effect due to the unbalance aligning with the shaft bow as explained in Section 5.5.

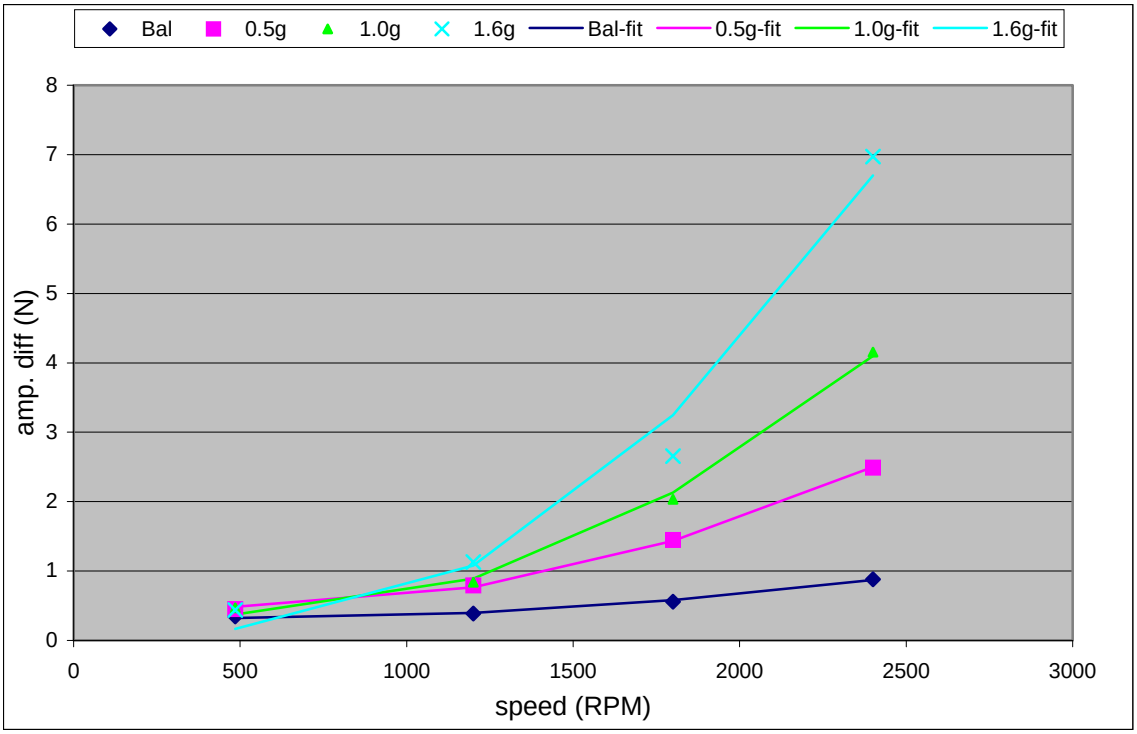

Figure 5.18: Alternating force vs. speed with LS curve fits, θ_u=90°

For the 225° data set, shown in Figure 5.19, the least-squares curve fit matched the experimental data well. It shows consistently low SSE values for all of the unbalance levels, unlike the other two sets. The maximum $\sqrt{SSE}$ for this set was 0.167 N for the 1.6 g trial, while the 90° and 270° data are 0.707 N and 0.490 N, respectively.

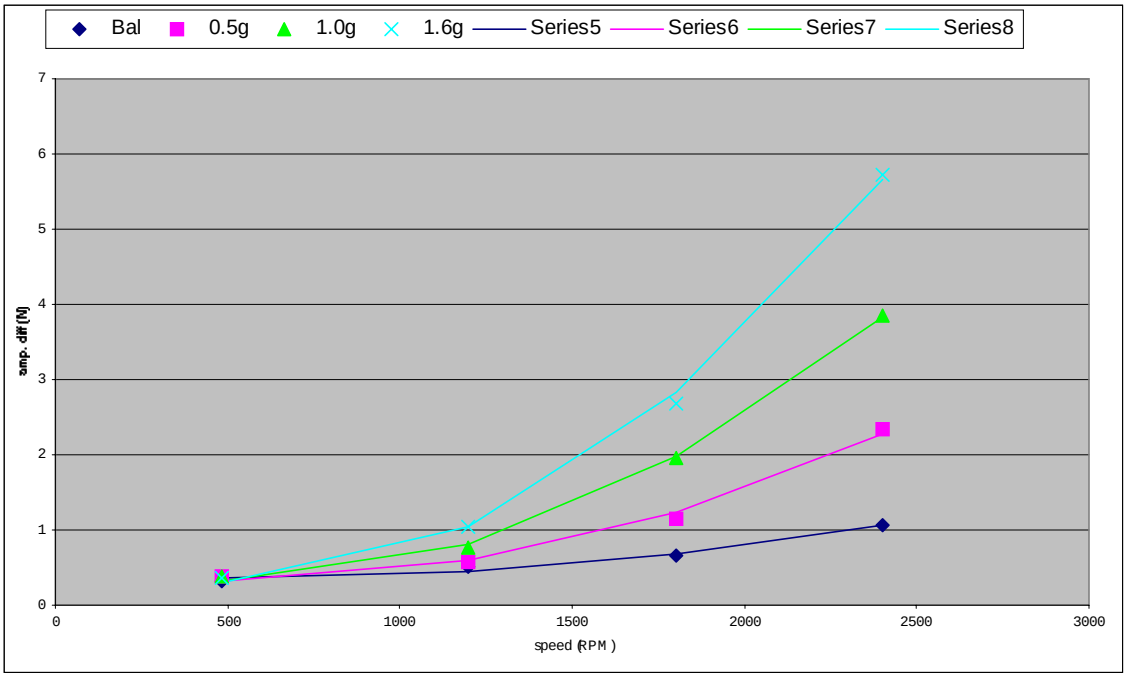

Figure 5.19: Alternating force vs. speed with LS curve fits, θ_u=225°

For the 270° set, the curve fits were not sufficient for accurate modeling of the experimental results. This is because the form of the curve used to fit the data. It assumes that the minimum force occurs at the slowest tested speed and grows proportionally to increases in speed. As shown in the plots, the interaction of the unbalance and shaft bow results in a reduction of the unbalance forces and the LS approximation used cannot model this effect. This results in poor fits and high SSE values, as shown in Table 5.9.

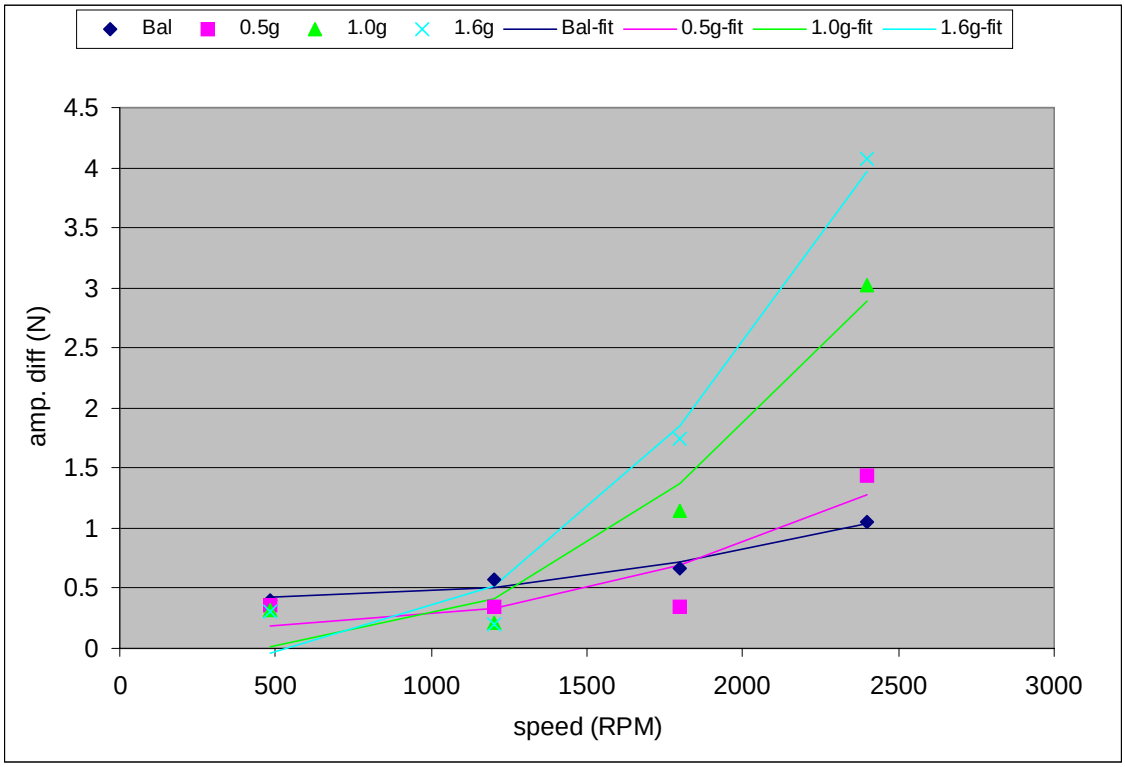

Figure 5.20: Alternating force vs. speed with LS curve fits, θ_u=270°

It is not surprising that the curve fits for the 225° data were better than the other angular location tests. While the 90° and 270° positions were tested because they provided an amplification and minimization, respectively, of the alternating force component, the 225° position was chosen because it showed a median response and had little apparent interaction with the shaft bow. The lack of shaft-bow effects allows the rotor to respond as expected and matches the expected response curves better than the other unbalance angular locations.

Since the angular location, θ_u=225°, reduced the effect of shaft bow, analyzing that data set provided further information on the performance of the multi-point code. Figure 5.21 shows a graph of the quadratic coefficients from the least squares curve fit plotted against the additional unbalance mass (0-1.6 g), and Figure 5.22 shows a similar plot for the curve fit constant coefficients. The quadratic coefficient, which is due to the unbalance loading, appears linear to the added unbalance (the r^2 value is 0.9979). The

constant terms do not appear to be strongly correlated with unbalance ($r^2 = 0.6981$), and the variation is likely due to changes in the shaft bow. The constant coefficients are believed to be representative of the amount of bow present in the shaft since they indicate the dynamic force at the slowest tested speed.

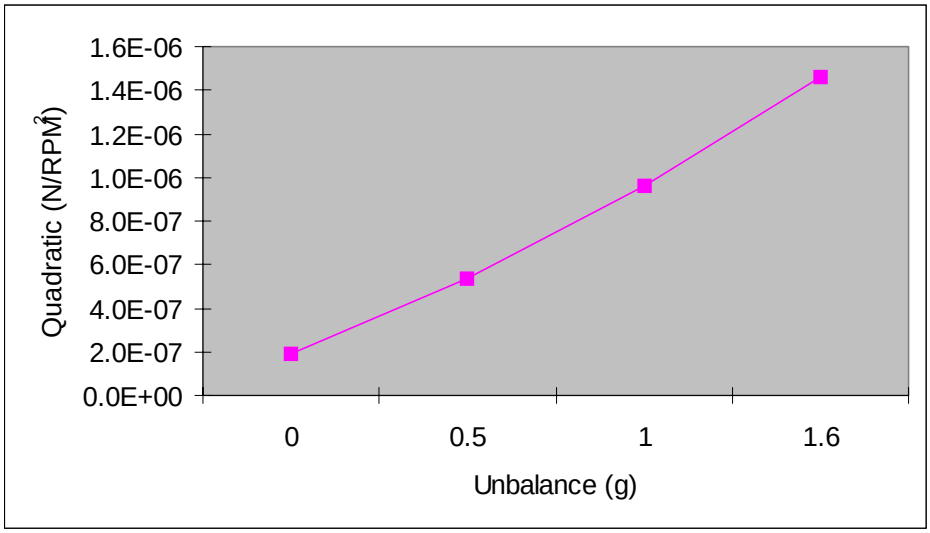

Figure 5.21: Quadratic coefficients vs. unbalance for θ_u=225°

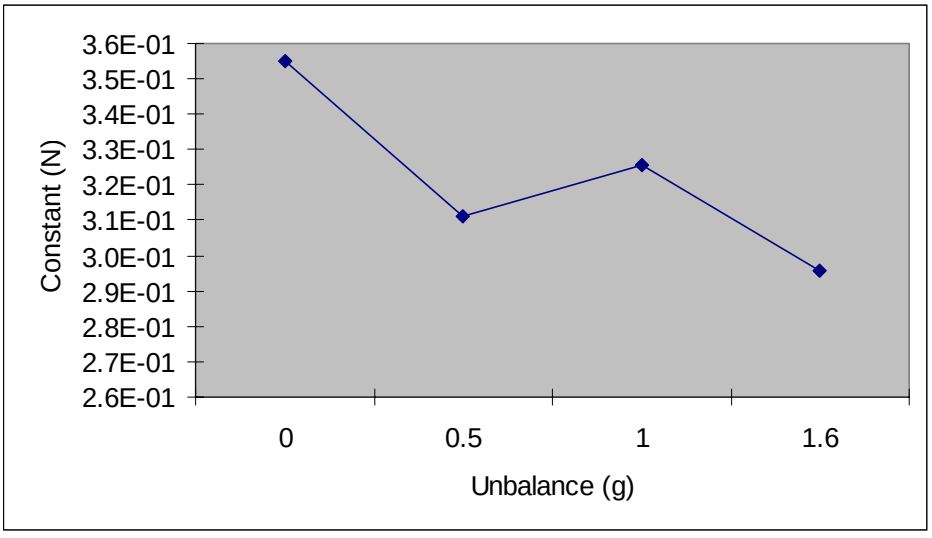

Figure 5.22: Constant coefficients vs. unbalance for θ_u=225°

The quadratic coefficients can also be calculated theoretically by using Equation (5.1). The mass of the additional unbalance is known as well as the distance from where

it is added to the shaft center. Figure 5.23 shows a plot of the experimental as well as the theoretical coefficients plotted against unbalance magnitude. The first observation is that the slopes are different (experimental = $8.002*10^{-7}$ N/RPM^2 vs. theoretical = $3.290*10^{-7}$ N/RPM^2). This appears to indicate that the added unbalance to the experimental test rig is producing more force than predicted by the theoretical model, and that there is still some bow/unbalance interaction. While the 225° case was the best of the three, there is likely still some interaction that is not modeled. For the other cases that were believed to show significant interaction, slopes were observed that differed greatly from the theoretical prediction. The 90° case for example showed a slope of $1.017*10^{-6}$ N/RPM^2 for the quadratic coefficients, as opposed to a theoretical slope of $3.290*10^{-7}$ N/RPM^2. The shaft bow also explains the non-zero value when there has been no unbalance added to the rotor. The residual shaft bow causes the rotor to respond as if there were unbalance added.

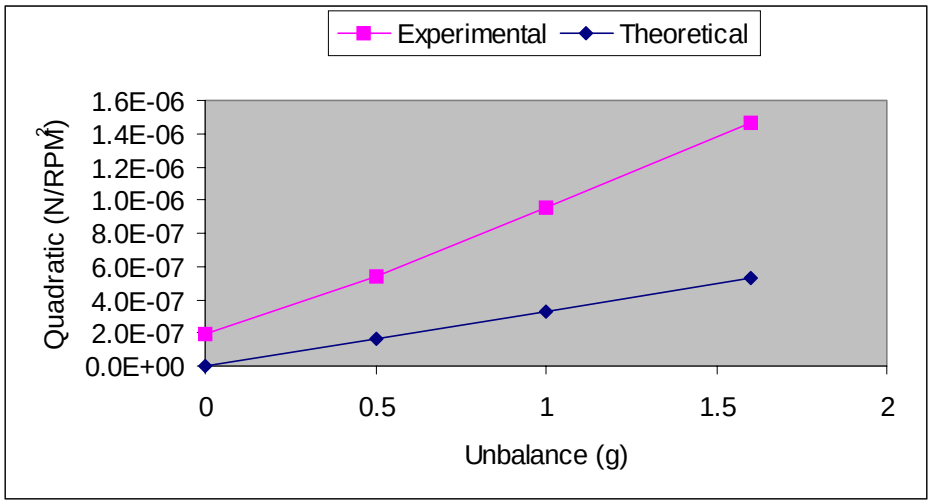

Figure 5.23: Experimental and theoretical quadratic coefficients vs. unbalance

5.8 Dynamic Test Conclusions

The dynamic testing provided some initial information into the important parameters for using magnetic bearings for force measurement. The major findings of this portion of the project are presented below.

Changes in the core program were made in order to process the dynamic current signals. These changes allow for the calculation of three different levels of force when monitoring a steady-state system: maximum, minimum, and static. These different forces result from the different combinations of the static rotor weight and the dynamic unbalance loads. When the dynamic force is opposed to the rotor weight, the bearings have to support a minimum load. When the two forces align, then the bearings experience the maximum load.

The dynamic tests were run with different combinations of unbalance and at different rotor speeds. The angular location of the unbalance mass was also varied to investigate shaft bow/unbalance interaction. Three angular locations were used (90°, 225°, and 270°) for four different levels of unbalance (0.0 g, 0.5 g, 1.0 g, and 1.6 g). The rotor speeds that were tested were 485 RPM, 1200 RPM, 1800 RPM, and 2400 RPM. All of these speeds were below the rotor's first critical speed. The predicted dynamic forces were analyzed as well as the predicted static loads. The dynamic prediction was defined as half of the difference between the maximum and minimum multi-point predicted force. The static force was predicted using the DC components of the coil currents.

The static weight predictions of the rotor while under a dynamic load were consistent with the results of the static load tests from Chapter 4. While the percent error and spread were slightly higher than in the static tests, it is obvious that the program was performing as planned for determining static non-synchronous loads. This type of measurement (the ability to accurately separate out a static load from a dynamic load) may prove useful in manufacturing scenarios such as textile roll applications where fibers may add a static load to a rotor.

Shaft bow creates significant difficulty in correlating experimental dynamic measurements with theoretical predictions. Adding unbalance to different angular locations can generate counterintuitive results depending on its relationship to the bow of the rotor. When the unbalance is aligned with the bow, excessive dynamic forces are created which do not match the expected quadratic function of speed. If the additional

unbalance is 180° out of phase with the shaft bow, the dynamic forces may be reduced or even eliminated. Since the theoretical model is the baseline for measuring the accuracy of the multi-point technique, care must be taken to provide a valid comparison. A model was created that attempted to simulate the interaction of the shaft bow with the additional unbalance. It provided insight into this phenomenon, but did not match well enough to use as a baseline for measuring the accuracy of the multi-point method.

To determine if the experimental data was following the correct trends, a method to quantify the data was necessary. Using the plots of dynamic force against speed, a custom curve-fit routine was created that used a least-squares regression to fit a curve through the experimental points. The curve fit assumes that the predicted dynamic forces at the slowest test rotor speed are the minimum force values and due to shaft bow. The dynamic forces are then assumed to grow proportionally to the rotor speed squared for speeds greater than the slowest test speed. This procedure allowed the speed dependency of the experimental data to be quantified by the quadratic and constant coefficients. The curve fits were first examined to determine if the unbalance loads grew with speed as expected. The coefficients were then analyzed to determine if the rotor was responding to unbalance in a linear fashion. The 225° unbalance location trials provided the best results for these tests because it experienced the least amount of unbalance/shaft bow interaction.

Chapter 6

Conclusions and Recommendations

6.1 Overview of Work Completed

The purpose of this work was to investigate a new methodology for concurrently utilizing AMBs as support bearings and shaft force sensors. The new methodology represents an approach that can provide equal or better accuracy than conventional techniques using AMBs for force measurement, but without the complexity of the current methods. Force measurement with AMBs provides several advantages over traditional methods of measuring applied loads. Several researchers have utilized AMBs for measuring pump impeller forces that were difficult to obtain previously. Other research topics include assembling a rocket thrust measurement system with AMBs, and using AMBs to determine labyrinth seal coefficients.

This new technique, the multi-point method, utilizes multiple current pairs in order to perform system identification to determine the shaft forces and rotor location within the bearing stator. The multiple current pairs are obtained by perturbing the AMB system and measuring the controller response. No position measurements are required, and the force equation used in the technique does not rely on complex correction factors. By not requiring position measurements, the multi-point method minimizes the instrumentation required and avoids problems such as non-collocation errors that are associated with position measurements on flexible rotors. Eliminating the correction factors reduces the amount of highly controlled calibration that is required. The multi-point method provides robust predictions of force, and is ideal for harsh environments outside of the laboratory.

A preliminary validation of the multi-point force measurement algorithm was performed using Magnetic Finite Element Analysis (MFEA). Using an E-core bearing geometry, several combinations of applied loads and target positions were modeled using MFEA. For each combination, the MFEA program generated five current pairs that were then used by the multi-point algorithm to predict the conditions used to create them.

A test rig was then constructed using a Bently-Nevada rotor kit and a Revolve MBRetro kit. These two packages provided the necessary components to perform the testing and allowed the flexibility to perform the range of tests that were conducted in this project. A National Instruments data acquisition board was used to record the pertinent data signals. The first test analyzed the multi-point code's ability to predict static loads on a single magnetic actuator. An overhung geometry was used to isolate a single bearing and masses were used to generate different loadings. The rotor was moved to different positions within the bearing stator to investigate the effect of variations in air gap lengths. An additional external eddy-current proximity probe was used to monitor shaft positions for use in the single-point predictions. These were used for comparison only and the position signals were not used in the multi-point predictions. The multi-point code provided equal or better force predictions than the analogous single-point methods. Additionally, the algorithm's displacement predictions could potentially provide further information about model uncertainties.

This initial static work was extended to a second static test configuration. For this test, the rotor was fully supported in magnetic bearings. This reduced the uncertainty in the mechanically determined bearing loads, since the previous test used a moment balance to determine the mechanical load and introduced uncertainty in the moment arm measurements. Again, disk masses were used to add weight to the rotor and different rotor positions were used within the bearing stator. For this arrangement, the multi-point method was able to provide much better force predictions than traditional single-point methods. The displacement predictions showed a trend that appeared to be load-

dependent that was determined to be due to rotor misalignment from shaft flex under the different loadings.

The misalignment finding led to a small study to analyze the effects of misalignment on the multi-point procedure. By moving the rotors within the stators in opposing directions, misalignment of the shaft can be induced. This was done in both the vertical and horizontal plane. The accuracy and precision of the force predictions for the two tests were consistent with those seen in earlier trials. However, the predicted displacements were not. The horizontal predictions showed very little influence from misalignment. The vertical position predictions showed a very strong, linear relationship with the magnitude of misalignment. This may indicate that the multi-point method is predicting an "effective gap" and in this way accounting for uncertainties in the physical system.

The ability of the multi-point program to predict dynamic loads was also tested. With the rotor fully supported with AMBs, a motor was attached to drive the shaft. Different speeds were analyzed as well as different amounts of unbalance. The different unbalance cases allowed different dynamic forces to be applied to the bearings. The multi-point calculation technique allows different forces to be predicted. It was possible to calculate the maximum, minimum, or static loading on the bearings by arranging different combinations of current measurements. The maximum load would correspond to when the unbalance load aligned with the static load (weight) of the rotor. The minimum is when the two are out of phase. The static prediction essentially DC-couples the force prediction to give only the weight of the rotor without any rotating forces.

Dynamic forces were difficult to quantify because of two reasons. Since the rotor was driven by a motor that was attached by a flexible coupling, there was some uncertainty in the true dynamic loading of the bearings. It is possible that the motor bearings could have either supported a portion of the dynamic load or contributed to it. Additionally, there was a bow in the shaft used in the tests, and because of the unbalance/shaft bow interaction, the location of the rotor unbalance played a significant

role in the dynamic loads. Due to these variables, direct comparisons with theoretical predictions of dynamic loads did not prove successful.

Unbalance masses were positioned at several different angular locations in an attempt to quantify the shaft bow/unbalance interaction. The results appeared inconsistent, and were likely due to the flexible shaft that was used in the testing. Despite not being able to make direct comparisons, the dynamic results were inspected for trends in the data. The dynamic forces were plotted against both unbalance magnitude and rotor speed and the expected trends were observed. The addition of unbalance masses created a linear increase in the predicted dynamic forces. The predicted dynamic forces also appeared to increase proportionally to the rotor speed squared. This relationship was verified by fitting a quadratic least-squares curve fit to the plots of dynamic force against rotor speed. It was determined that the shaft bow created different responses depending on where the unbalance was positioned and the amount of unbalance/shaft bow interaction greatly affected the quality of the curve fits.

6.2 Discussion of Results

The following is a list of findings from the experimental testing of the multi-point force prediction algorithm. The rest of the chapter will be devoted to summarizing the work done and outlining future work in this area.

- The multi-point method provides very good predictions of force and displacement when tested with Magnetic Finite Element Analysis (MFEA), achieving errors of less than 0.1% for both quantities. The extreme accuracy of the multi-point method in predicting MFEA generated data was partly due to the exact knowledge of bearing geometry and material properties, as well as the use of a variable derating factor.

- In experimental tests, the multi-point method provides equal or superior force predictions than analogous single-point methods with no knowledge of rotor position necessary. Static test #1 utilized an overhung configuration and only a

single AMB. Five current pairs were used for the multi-point calculations for each combination of rotor location and shaft load. Two single-point force predictions were generated, a corrected and a non-corrected prediction. The corrected predictions utilized position measurements, as measured by an eddy-current probe, that were corrected for non-collocation errors. The non-corrected predictions used position measurements taken with an eddy-current probe without any manipulation to the readings. The non-corrected predictions are more representative of field applications where problems such as non-collocation errors are likely. The maximum percent error for the multi-point force predictions was 2.25%, versus 4.58% and 14.89% for the corrected and non-corrected single-point predictions, respectively. The maximum percent spread values, which measure how tightly the predictions are banded, on the predicted forces were 8.13% for the multi-point method, 6.25% for corrected single-point and 23.67% for the non-corrected single-point predictions. However, if one data point is rejected, the multi-point percent spread drops to 3.32%. The variation between the corrected and non-corrected single-point measurements also demonstrates the susceptibility of single-point measurements to uncertainties in the gap measurements.

- Static test #2 levitated the entire rotor with two AMBs to eliminate some of the uncertainty associated with the overhung configuration and to examine the multi-point method with regards to multiple bearing systems. In this test, the two bearings are treated as a single bearing, where the predicted load is the sum of both bearing loads and the predicted rotor location is assumed for both as well. Additionally, only three current pairs were used in the multi-point calculations to investigate the accuracy of the method with reduced input data. The multi-point force predictions were consistently better than the analogous single-point predictions. The maximum percent error for the multi-point prediction was 2.11% and 7.12% for the single-point method. The maximum percent spread was 2.76% for the multi-point technique and 20.93% for the single-point method. (Note that there was no correction applied to the position measurements in the two-bearing system.) There does not appear to be an accuracy penalty for

reducing the number of current pairs used in the multi-point method, although three is the minimum number of pairs recommended from a practical standpoint.

- The multi-point method provides a prediction of rotor location in addition to bearing force. However, the multi-point rotor location predictions are referenced from the true bearing centerline, where all of the actuator air gaps are equal. The controller-determined centerline may not correspond to the true centerline, which would lead to discrepancies between the predicted and controller-specified locations. There were discrepancies between the multi-point predicted locations and the eddy-current probe position measurements that could be the result of several possibilities. The multi-point predictions may be accounting for model uncertainties such as geometry, material properties, and magnetic flux irregularities by determining the "equivalent" rotor location. Since the force equation used by the multi-point algorithm, Equation (1.7), does not have any mechanism to account for variations in the parameters mentioned above, the program may determine the rotor location that Analysis of a plot of predicted displacements vs. actual displacements may provide insight into the origins of these uncertainties. A non-unity slope indicates that there is a position-dependent variable not being modeled, and a non-zero y-intercept suggests that a constant value such as material properties, geometry, or constraints is in error. The final possibility is that the program is not performing correctly and is generating erroneous rotor locations. No concrete conclusions may be made about the implications of the multi-point algorithm location predictions at this time. A full analysis of these implications is beyond the scope of this work.

- A static misalignment investigation was performed using the rotor configuration of static test #2. This was to analyze how the program handles misalignments between the rotor and stator. By moving the two bearing rotors in opposite directions, a known misalignment between the rotor and stator was generated and the multi-point results were analyzed to determine how the misalignment affected the force and rotor displacement predictions. The misalignment test was

performed in both the vertical and horizontal planes. The force predictions showed very little dependence on the amount of misalignment present in the bearings. The vertical misalignment test showed a percent error and spread of 0.18% and 3.24%, respectively. The horizontal misalignment test generated percentages of -0.42% and 0.81%, respectively. The very low percentage spread for the horizontal test seems to indicate that horizontal misalignment has very little influence on the force predictions. The multi-point predicted rotor displacements were also analyzed with respect to misalignment. The vertical test results showed a very strong linear relationship between misalignment and predicted rotor position. The horizontal test also showed a linear relationship, but the slope was much smaller. This may be due to an "uncoupling" of the axes when horizontal misalignment is present, as described in Section 4.4.2, but further investigation into this hypothesis is beyond the scope of this project.

- A dynamic test of the multi-point algorithm produced mixed results. Predictions of the static rotor weight as well as the dynamic forces were calculated. The static load predictions were reasonably accurate with a percent error of 4.35% and a percent spread of 6.83%. An accurate measure of static loads in a dynamic environment is potentially useful in manufacturing scenarios such as monitoring fiber tension.

- The ability of the multi-point algorithm to predict dynamic forces was more difficult to quantify. Interaction between residual shaft bow and unbalance masses caused unexpected results and proved difficult to model. An investigation was performed by varying the angular location of the unbalance masses to observe the resulting dynamic forces and determine how the shaft bow and unbalance loading interacted. A model of this interaction was not successful in predicting the experimentally determined forces. This was likely due to changes in the bow of the small shaft as the unbalance and rotor speed were varied.

- Although direct comparisons between the multi-point dynamic force predictions and theoretical force predictions were not successful, general trends in the data were observed. As the dynamic parameters (unbalance mass, unbalance location, and rotor speed) were varied, the multi-point force predictions showed the expected trends in response to the variables. A linear increase in dynamic force predictions was observed with increases in unbalance magnitude, and a general quadratic growth in dynamic force predictions was observed with increases in rotor speed. A quadratic curve fit was applied to the algorithm predictions to verify the quadratic trend with varying results. For the cases with unbalance locations that interacted heavily with the shaft bow, the curve fit was not successful. The trial with the least interaction showed a very close match with the quadratic curve fit.

6.3 Conclusions

The main conclusions of the results are presented below. These final conclusions briefly summarize the results presented above.

- The theoretical (MFEA) validation produced very good results.

- Static testing provided experimental verification that the multi-point method works in physical systems.

- The multi-point technique was able to provide equal or better force predictions than equivalent single-point force measurements.

- The multi-point displacement predictions may be accounting for model uncertainties, but further work is required.

- Dynamic testing introduced more complexity into the multi-point testing, including shaft bow/unbalance interaction and program modifications.

- The predictions of static rotor weight in the dynamic configuration were reasonable, showing similar percent spread and error as previous static tests.

- The expected trends were observed in the multi-point dynamic force predictions.

6.4 Future Work

Based on the results of this project, the following topics show the most promise for improvements to the multi-point method.

- In order to allow more flexibility within the multi-point program, multiple bearings should be treated separately. Currently, the forces for each bearing are calculated using the measured current values for each bearing and a single assumed rotor location for all bearings. The predicted forces are then summed together and analyzed. Treating the bearings separately would effectively double the number of calculations and complicate the search algorithm, but would ultimately provide results for each bearing individually, which may be advantageous, if not necessary, for many scenarios. This is particularly important for dynamic scenarios where rotor mode shapes could cause the rotor to be in significantly different positions in the two bearings.

- In order to gain further insight into the multi-point predictions of rotor position, improved experimental procedures should be implemented to provide more a more accurate measurement of the actual air gaps. When the absolute rotor position is known with more confidence, the correlation between it and the multi-point predictions can be analyzed further.

- The derating factor used in the multi-point algorithm, as well as the single-point predictions, was determined empirically based on known rotor loads. Situations could arise in industrial applications where the rotor weight may not be known or available. A method for determining the derating factor a priori without the

knowledge of specific loads would allow this approach to be used in more varied applications, as well as easier to implement.

- The dynamic work presented here was performed mainly to ensure that the multi-point technique would not collapse under the additional problems associated with rotating scenarios. Even though the method confirmed this, an additional investigation into how the program handles different dynamic effects would allow for further implementation of this new technique.

References

1. ANSI/ASME, "Measurement Uncertainty," *Supplement to ASME Performance Test Codes*, ANSI/ASME PTC 19.1-1985.

2. Baun, D.O., Fittro, R.L., and Maslen, E. H., 1996, "Force Versus Current and Air Gap Calibration of a Double Acting Magnetic Thrust Bearing," presented at the *International Gas Turbine & Aeroengine Congress and Exhibition*, Birmingham, UK, June 2-5. ASME pamphlet paper no. 96-GT-121.

3. Baun, D.O., and Flack, R.D., 1999, "A Plexiglass Research Pump with Calibrated Magnetic Bearings/Load Cells for Radial and Axial Hydraulic Force Measurement," Journal of Fluids Engineering, Vol. 121, March, pp 126-132.

4. Clements, J., 2000, "The Experimental Testing of an Active Magnetic Bearing/Rotor System Undergoing Base Excitation," Master's Degree Thesis, Department of Mechanical Engineering, Virginia Polytechnic and State University, USA.

5. Fittro, R. L., Baun, D. O., Maslen, E. H., and Allaire, P.E., 1997, "Calibration of an 8-Pole Planar Radial Magnetic Actuator," presented at the *International Gas Turbine & Aeroengine Congress and Exhibition*, Orlando, FL, June 2-5.

6. Guinzburg, A., and Buse, F.W., 1994, "Axial and Radial Forces on a Pump Impeller Obtained with a Magnetic-Bearing Force Measurement Rig," *Proceedings of the Fourth International Symposium on Magnetic Bearings*, August, ETH Zurich, pp 537-545.

7. Guinzburg, A., and Buse, F.W., 1995, "Magnetic Bearings as an Impeller Force Measurement Technique," *Proceedings of the Twelfth International Pump Users Symposium*, March, pp 69-76.

8. Hope, R. W., Tessier, L. P., Knospe, C., and Miyaji, T., 1998, "Adaptive Vibration Control of Industrial Turbomachinery, 98-GT-405," *International Gas Turbine & Aeroengine Congress & Exposition*.

9. Imlach, J., Kasarda, M.E.F., and Balaji, P.A., 2000, "Enhancements to AMB Force Measurement Procedures for Application To a Rocket Thrust Measurement System," *International Gas Turbine & Aeroengine Congress and Exhibition*, Munich, Germany, May 8-11. ASME pamphlet paper no. 2000-GT-414.

10. Kasarda, M. E. F., Allaire, P. E., 1996, "Comparison of Predicted and Measured Rotor Losses in Planar Radial Magnetic Bearings," *ASME/STLE Tribology Conference*, San Francisco, CA, October 13-17.

11. Kasarda, M. E. F., 1997, "The Measurement and Characterization of Power Losses in High Speed Magnetic Bearings," Doctoral Dissertation, Department of Mechanical and Aerospace Engineering, University of Virginia, USA.

12. Kasarda, M. E., 1999, "Magnetic Bearings for Improved Process Control," 1999 NSF Grantees Conference Proceedings, Long Beach , CA, January.

13. Knopf, E., and Nordmann, 1998, "Active Magnetic Bearing for the Identification of Dynamic Characteristics of Fluid Bearings – Calibration Results," *Proceedings of the Sixth International Symposium on Magnetic Bearings*, Cambridge, MA, August, pp. 52-61.

14. Mendoza, H., 2000, "Evaluation of the Effectiveness of an Active Magnetic Damper (AMD) in Damping Subsynchronous Vibrations in a Flexible Rotor," Master's Degree Thesis, Department of Mechanical Engineering, Virginia Polytechnic and State University, USA.

15. Plonus, M. A., 1978, "Applied Electromagnetics," McGraw-Hill, New York, pp. 410, 414-416.

16. Springer, H., 1989, "Nonlinearities and Hysteresis Effects in Ferromagnetic Circuits of Electromagnetic Bearings," ROMAC Report # UVA/643092/MAE89/405, University of Virginia, June.

17. Wagner, N.G. and Steff, Klaus, 1998, "Dynamic Labyrinth Coefficients from a High-pressure Full-Scale Test Rig Using Magnetic Bearings," DEMAG DELAVEAL Turbomachinery, Duisburg, Germany.

Appendix A

Derivation of Double-Acting Force Equation

A.1 Basic Equations

The equation governing a magnetic actuator can be derived completely from first principles. Magnetic circuit theory is employed to develop the basic equations that are extended to describe the magnetic actuator. Plonus (1978) presents this derivation, and it is reproduced here for completeness. A device of simple geometry is assumed so to keep the equations of reasonable length. The toroid is a ring of material that has a circular cross-section, A, as shown in Figure A.1.

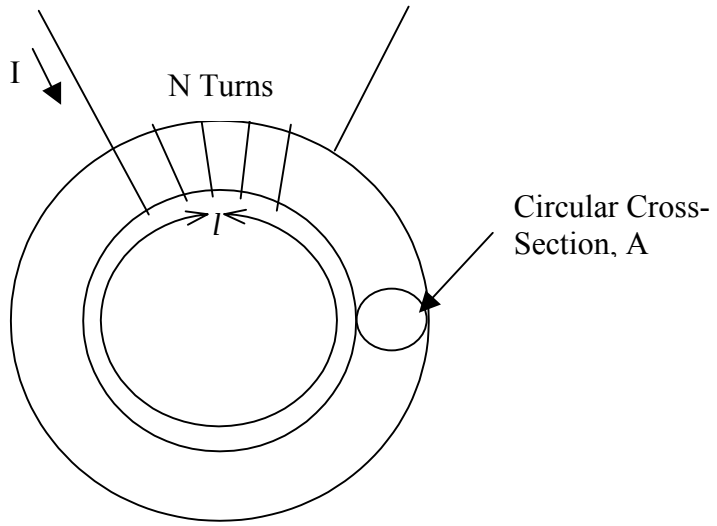

Figure A.1: Illustration of a toroid

If this toroid of length *l* is wrapped with N turns of wire that carry a current, I, Equation (A.1) governs the magnetic field strength, H, that is generated.

$$H = \frac{NI}{l} \tag{A.1}$$

This simple relationship is valid because the magnetic field and cross-sectional area are uniform. If they were not, an integral relationship would have to be solved to find the proper relationship. The relationship between magnetic field strength, H, and flux density, B, is given by Equation (A.2).

$$B = \mu H = \frac{\mu NI}{l} \tag{A.2}$$

The magnetic flux, ϕ, in the circuit is given by

$$\phi = \iint BdA = BA \tag{A.3}$$

if the area of the magnetic circuit is constant. The energy density, *w*, contained in the toroid of volume *v* is given by Equation (A.4).

$$w = \frac{W}{v} = \int_0^B HdB = \int_0^B H\mu dH = \frac{\mu H^2}{2} \tag{A.4}$$

A.2 Magnetic Force Due to Gaps

Now, if the toroid is cut in half and separated by a gap of length g as shown in Figure A.2, the magnetic field traversing the gaps will generate an attractive force between the two halves. For simplicity, the total number of Amp-turns, NI, will be concentrated on the top half of the assembly.

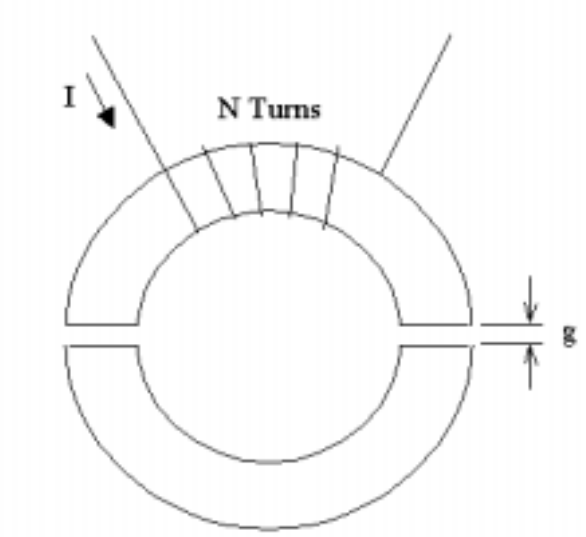

Figure A.2: Split toroid with gap length, g

The energy contained within each air gap can be calculated if the volume of the air gaps is known. For this case, the volume of the air gaps is given by

$$v_g = Ag \tag{A.5}$$

and the energy within it is defined by Equation (A.6).

$$W_g = \frac{\mu H^2 v}{2} = \frac{\mu H^2 Ag}{2} \tag{A.6}$$

If the two halves are pulled apart by an incremental amount, Δx, the energy required is ΔW, and given by Equation (A.7) if the flux is assumed to be held constant. This incremental work is the difference between the two energy states. The factor of two in the equation is because there are two air gaps in the magnetic circuit, and each is increased by Δx.

$$\Delta W = 2\left(\frac{\mu H^2 A(g + \Delta x)}{2} - \frac{\mu H^2 Ag}{2} \right) = \mu H^2 A \Delta x \tag{A.7}$$

The magnetic force required to move an object over a distance x is defined as the energy expended in the move divided by the distance of the move. By substituting the known quantities into this relationship, Equation (A.8) is found.

$$F = \left.\frac{-\partial W}{\partial x}\right|_{\phi=Const.} \approx \frac{-\Delta W}{\Delta x} = \frac{-\mu H^2 A \Delta x}{\Delta x} = -\mu H^2 A \tag{A.8}$$

If Equations (A.2) and (A.3) are substituted into the above relationship, the magnetic force can be expressed in terms of different quantities. The negative sign can be dropped since only the magnitude of the force is of interest.

$$F = \mu H^2 A = \frac{B^2 A}{\mu} = \frac{\phi^2}{\mu A} = \frac{\mu A (NI)^2}{l^2} \tag{A.9}$$

In the above equation, *l* is the total length of the magnetic circuit. These expressions give the exact force between the two halves of the toroid assembly if the exact values of the parameters are known. The difficult parameter to define is μ, since it is the permeability of the entire magnetic path, which includes the magnetic material and air in the gaps. However, a simplification can be made that will allow the magnetic force to be expressed in terms of the air gap length only and eliminate this complication.

A.3 Simplification of the Force Equation

The path of the magnetic flux through the toroid assembly can be separated into four separate sections. Section 1 is the upper half of the toroid, section 2 is one air gap, section 3 is the lower half of the toroid, and section 4 is the second air gap. The definition of magnetomotive force is given by Equation (A.10). If the closed loop integral is broken into the four segments described above, it can be rewritten as Equation (A.11).

$$MMF = NI = \oint Hdl \tag{A.10}$$

$$NI = \int_1 Hdl + \int_2 Hdl + \int_3 Hdl + \int_4 Hdl \tag{A.11}$$

If the magnetic field strength is assumed constant across each section, this equation can be rewritten as Equation (A.12).

$$NI = H_1 l_1 + H_2 l_2 + H_3 l_3 + H_4 l_4 \tag{A.12}$$

The magnetic field strength, H, can be expressed in terms of flux density, B, according to Equation (A.13). If the actual permeabilities in this equation are replaced with relative permeabilities as defined in Equation (A.14), then Equation (A.12) can be expressed as Equation (A.15).

$$H = \frac{B}{\mu} \tag{A.13}$$

$$\mu = \mu_0 \mu_r \tag{A.14}$$

$$NI = \frac{B_1 l_1}{\mu_0 \mu_1} + \frac{B_2 l_2}{\mu_0 \mu_2} + \frac{B_3 l_3}{\mu_0 \mu_3} + \frac{B_4 l_4}{\mu_0 \mu_4} \tag{A.15}$$

The relative permeabilities of a ferromagnetic material and air are drastically different. Most magnetic materials have a relative permeability on the order of 3000, where air is very close to unity. Because of the large difference in these values, the terms where the flux is traveling through magnetic material (1 and 3) can be neglected, and only the air gaps considered. If the lengths of the air gaps and the flux density in them are assumed equal, then Equation (A.15) becomes

$$NI = \frac{2Bg}{\mu_0} \tag{A.16}$$

where g is the length of the air gaps and μ_0 is the magnetic permeability of a vacuum. Rearranging this equation to define the flux density, B, and substituting into Equation (A.9) gives the relationship governing the magnetic force between the two halves of a toroid in terms of the Amp-turns of the circuit, the pole-face area, and the air gap width.

$$F = \frac{\mu_0 A(NI)^2}{4g^2} \tag{A.17}$$

A.4 Double-Acting Actuator Force Equation

The net force on an object suspended between two magnetic actuators (a double-acting actuator) is simply the difference of the force generated by the bottom actuator subtracted from the force generated by the top. Figure A.3 shows an example of a double-acting actuator.

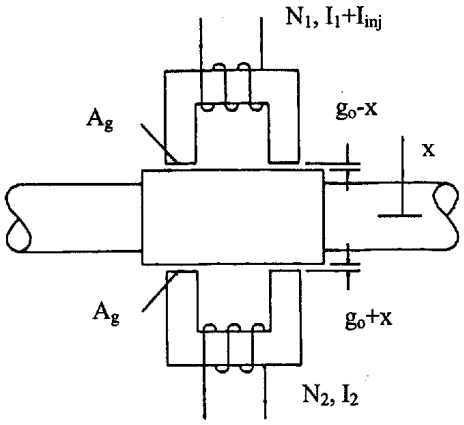

Figure A.3: Double-acting magnetic actuator

The net force on the suspended rotor is given by Equation (A.18). (The top actuator is considered actuator 1, and the bottom actuator is considered as 2.)

$$F_n = F_1 - F_2 = \left[\frac{\mu_0 A(NI)^2}{4g^2}\right]_1 - \left[\frac{\mu_0 A(NI)^2}{4g^2}\right]_2 \tag{A.18}$$

If the two actuators are identical (where the number of coils and pole-face area is the same), this can be reduced to

$$F_n = \frac{\mu_0 A N^2}{4}\left[\frac{I_1^2}{g_1^2} - \frac{I_2^2}{g_2^2}\right] \tag{A.19}$$

The control scheme that is used for magnetic bearings breaks the coil currents into two components, as in Equation (A.20). There is a constant bias current, i_b, and a perturbation current, i_p. The bias current is assumed equal for the two bearings. The perturbation current, which is actually the control signal, is the same for both bearings, but different in sign. This is defined in Equations (A.21) and (A.22).

$$i = i_b + i_p \tag{A.20}$$

$$i_{b1} = i_{b2} \tag{A.21}$$

$$i_{p1} = -i_{p2} \tag{A.22}$$

Additionally, the gaps, g_1 and g_2, can be simplified. There is a nominal air gap that is defined as half of the difference between the stator outer diameter and the rotor inner diameter. As the rotor moves up or down, the deflection is either added or subtracted from this nominal gap. By using this method, there is only one unknown, rotor deflection from the center point, instead of two, g_1 and g_2. Equation (A.23) defines these new gap definitions.

$$g_{1,2} = g_0 \pm \Delta y \tag{A.23}$$

By substituting Equations (A.20) and (A.23) into Equation (A.19), the following relationship is found.

$$F_n = \frac{\mu_0 A N^2}{4}\left[\frac{(i_b + i_p)^2}{(g_0 + \Delta y)^2} - \frac{(i_b - i_p)^2}{(g_0 - \Delta y)^2}\right] \tag{A.24}$$

By expanding this equation out, several more assumptions may be made. If the perturbation (correction) currents are assumed much smaller than the bias currents, and that the shaft deflection assumed much smaller than the nominal gap, then the higher order terms of these parameters may be neglected. By making this approximation, the linearized form of the double-acting actuator force equation, Equation (A.25), is generated.

$$F_n = \mu_0 A N^2\left[\frac{g i_b i_p - i_b^2 \Delta y}{g^3}\right] \tag{A.25}$$

A.5 Double-Acting Actuator Stiffness Equations

The stiffness of the magnetic actuators is defined as the rate of change of force with respect to a single variable, while holding all other variables constant, as shown in Equation (A.26). The two main variables in the forces equation presented above are the rotor position, Δy, and the perturbation current, i_p. This implies that there are two bearing stiffness values of interest: the position stiffness that is related to Δy, and the current stiffness that is related to i_p. These stiffness values are defined in Equations (A.26) and (A.27).

$$K_y = \left.\frac{\partial F}{\partial \Delta y}\right|_{ip=0} = \frac{-\mu_0 N^2 A_g i_b^2}{g^3} \tag{A.26}$$

$$K_i = \left.\frac{\partial F}{\partial i_p}\right|_{\Delta y=0} = \frac{\mu_0 N^2 A_g i_b}{g^2} \tag{A.27}$$

Appendix B

Multi-Point Algorithm Source Code

The actual multi-point algorithm is broken into several programs. The main program acts as somewhat of a front-end and contains the bearing geometry and important variables that drives the other sections. The main program calls a subroutine that performs all of the calculations to generate the force matrix. Options within that subroutine allow for the calculation of the maximum, minimum, or static forces for dynamic situations. A further subroutine can be used with the dynamic version that checks the current autospectrums to ensure that the peak used for the calculations corresponds to the synchronous frequency.

Dynamic Main Program

```
clear
format compact

global go width alpha beta gamma bth kth Npoints NTEST list nsamp
scanrt core

%% Parameter Definitions %%
%% Can be hard-coded or user-prompted %%
uo=4*pi*1e-7;
bth=3.2/3000;  %input('Enter the value of "bth" in mm ');
kth=uo*.2248*228^2*.102672;  %input('Enter the proportionality constant
"kth" in N-sqmm/sqAmpere ');
alpha=.525;  %input('Enter the value of alpha: ');
beta=3.45;  %input('Enter the value of beta: ');
gamma=5;  %input('Enter the value of gamma: ');
width=.496;  %input('Enter the width of the magnet pole in mm: ');
go=.015;  %input('What is the nominal value of the gap "go" in mm of
the actuator? ');
nsamp = 8192;  %input('How many samples per channel? ');
scanrt = 4096;  %input('What was the sample rate? ');

%% Define the data files to use %%
core = 'c:\my documents\data\dynamic tests\1.6g_2400_';
list = ['100.txt';'150.txt';'200.txt'];

%% Set the number of test cases to use %%
length = size(list);
NTEST=length(1);

%% Set the number of points to use in the displacement vector %%
Npoints=2500;

%% Initialize the force matrix to zero %%
force(2*Npoints,NTEST)=0;

%% Loop to generate the force matrix %%
for jj=1:1:NTEST
   [dist,frce]=radial(jj);
   frce=frce';
   force(:,jj)=frce;
   clear frce
end

%% Generate a matrix of the standard deviations of each row %%
for kk=1:1:2*Npoints
   stnddev(kk) = std(force(kk,:));
end

%% Search routine to find the row with the smallest variation %%
index = 1;
for kk=1:1:2*Npoints-1
   if stnddev(kk+1)<stnddev(kk);
      index = index+1;
```

```
   else
   end
end

%% Assign the displacement and force values for output to user %%
xvalue = dist(index);
fvalue = mean(force(index,:));

disp('DISPLACEMENT(inch)       FORCE(Pounds)')
disp('---------------------------------------')
format long e
values=[xvalue' fvalue']
```

Force Subroutine

```
function [dist,frce]=radial(ii)
global go width alpha beta gamma bth kth Npoints NTEST list nsamp
scanrt core

%% Report to user which test is being calculated %%
format long;
D='PROCESSING TEST CASE #  ';
B=num2str(ii);
E=strcat(D,B);
disp(E)

%% Load the test case of interest %%
pth = strcat(core,list(ii,:));
clear data;
data = load(pth);

%% Assign the data to variable names %%
V13t = data(:,3); % top current for 13 bearing, V axis
W13t = data(:,4); % top current for 13 bearing, W axis
V13b = data(:,7); % bottom current for 13 bearing, V axis
W13b = data(:,8); % bottom current for 13 bearing, W axis
V24t = data(:,5); % top current for 24 bearing, V axis
W24t = data(:,6); % top current for 24 bearing, W axis
V24b = data(:,9); % bottom current for 24 bearing, V axis
W24b = data(:,10); % bottom current for 24 bearing, W axis

%% Calculate data acquisition sampling variables %%
dt = 1/scanrt;
T = nsamp*dt;
df = 1/T;
i = 0:nsamp-1;
t = dt*i;
freq = df*i;

%% Generate average top and bottom current signals %%
avg13top = (V13t.^2./2.+W13t.^2./2).^.5;
avg24top = (V24t.^2./2.+W24t.^2./2).^.5;
avg13bot = (V13b.^2./2.+W13b.^2./2).^.5;
avg24bot = (V24b.^2./2.+W24b.^2./2).^.5;

%% Generate autospectrums of average current signals %%
mag13top = abs(fft(avg13top))/nsamp;
mag24top = abs(fft(avg24top))/nsamp;
mag13bot = abs(fft(avg13bot))/nsamp;
mag24bot = abs(fft(avg24bot))/nsamp;

%% Loop to scale the autospectrums %%
for i=2:1:nsamp/2
   mag13top(i) = 2*mag13top(i);
   mag24top(i) = 2*mag24top(i);
   mag13bot(i) = 2*mag13bot(i);
   mag24bot(i) = 2*mag24bot(i);
end
```

```
freq = freq(1:nsamp/2);
mag13top = mag13top(1:nsamp/2);
mag24top = mag24top(1:nsamp/2);
mag13bot = mag13bot(1:nsamp/2);
mag24bot = mag24bot(1:nsamp/2);

%% Perform synchronous checks %%
[mag1,loc] = peakpick(freq,mag13top,df);
[mag2,loc] = peakpick(freq,mag24top,df);
[mag3,loc] = peakpick(freq,mag13bot,df);
[mag4,loc] = peakpick(freq,mag24bot,df);

%% Calculate the top and bottom current values for the force equation
%% The combination of the 2 dictates which force will be predicted,
%% either the maximum, minimum, or average %%
clear V13t V13b W13t W13b V24t V24b W24t W24b
V13t = mag1(1)+mag1(2);
V13b = mag3(1)-mag3(2);
W13t = mag1(1)+mag1(2);
W13b = mag3(1)-mag3(2);
V24t = mag2(1)+mag2(2);
V24b = mag4(1)-mag4(2);
W24t = mag2(1)+mag2(2);
W24b = mag4(1)-mag4(2);

%% Set step size for displacement vector %%
delg=go/Npoints;

%% Initialize the first value of displacement vector %%
x=-go;

%% Loop to calculate force vector for this test case %%
for ii=1:1:2*Npoints;
   dist(ii)=x;
   gap1=(2*go-x*(sin(22.5*pi/180)+sin(67.5*pi/180)))/2;
   gap2=(2*go+x*(sin(22.5*pi/180)+sin(67.5*pi/180)))/2;
   rat1=gap1/width;
   rat2=gap2/width;
   eps1=1;%(alpha+beta*(1-exp(-gamma*rat1)))^2;
   eps2=1;%(alpha+beta*(1-exp(-gamma*rat2)))^2;
   den1=(2*gap1+bth)^2;
   den2=(2*gap2+bth)^2;

   first=kth*eps1*(V13t^2)/den1;
   second=kth*eps1*(W13t^2)/den1;
   third=kth*eps2*(V13b^2)/den2;
   fourth=kth*eps2*(W13b^2)/den2;
   fifth=kth*eps1*(V13t^2)/den1;
   sixth=kth*eps1*(W13t^2)/den1;
   seventh=kth*eps2*(V13b^2)/den2;
   eighth=kth*eps2*(W13b^2)/den2;

   force1 = (first+second-third-fourth)*cos(45*pi/180);
   force2 = (fifth+sixth-seventh-eighth)*cos(45*pi/180);
   frce(ii)=0.5*(force1+force2);
   x=x+delg;
end
```

Check Subroutine

```
function [mag,loc]=peakpick(x,y,df)

j=1;

for i = 1:length(x)-1
   if i == 1
      if y(i)>.01
         mag(j) = y(i);
         loc(j) = x(i)*60;
         j = j+1;
      end
   else
   if y(i)>y(i-1)
      if y(i)>y(i+1)
         if y(i)>.005
            mag(j) = y(i);
            loc(j) = x(i)*60;
            j = j+1;
         end
      end
   end
   end
end

if loc(2)~=2400
   disp('Warning: AC Component not syncronous (press Enter)')
   pause
end
```

Appendix C

System Transfer Function

C.1 General Controller Transfer Function

The MB350 controller contains the microprocessor responsible for AMB control as well as the power amplifiers to drive the actuator coils. Each of these has a unique transfer function that governs its action when given an input. The entire control system including controller, amplifier, and proximity probes was modeled by Josh Clements (2000). The transfer function is dependent on the controller gains chosen by the user. Figure C.1 illustrates the components of the control system for a single axis that were modeled by Clements.

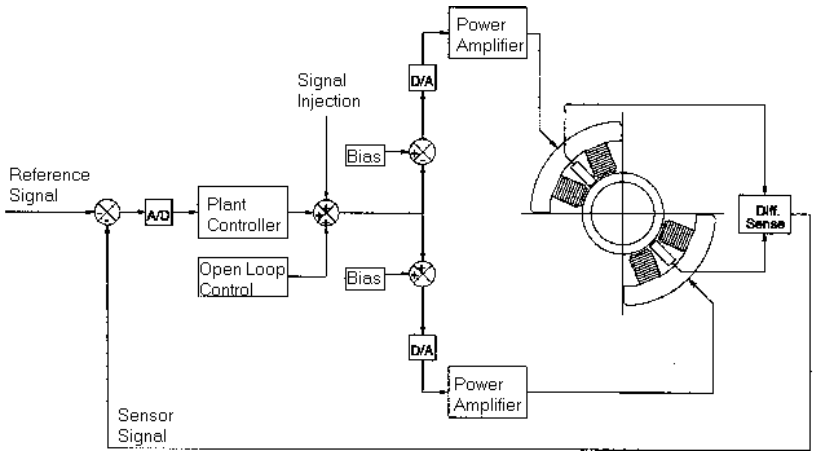

Figure C.1: Illustration of control components for a single axis

The system of Figure C.1 can be expanded into a block diagram showing the individual components as seen in Figure C.2. Each of the components shown has an associated transfer function that can be combined to arrive at the system transfer function.

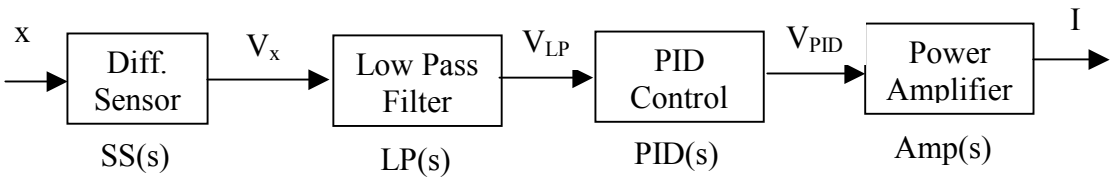

Figure C.2: Open loop block diagram of control

The differential sensor for each axis of the bearings was a variable reluctance type. The sensor was assumed to behave linearly and its transfer function is given by Equation (C.1).

$$SS(s) = \frac{V_x}{x} = 0.1572(Volts/mil) \tag{C.1}$$

The low pass filter is necessary in order to filter out any high frequency noise that could drive the controller into instability. Filtering high frequency signals also allows the bearings to operate more quietly, at the expense of the loss of some high frequency control. The unit was modeled as a second order low pass with user-adjustable parameters. Equation (C.2) gives the form of the filter where the variables available for modification are ω_{LP}, the cut-off frequency, and ξ_{LP}, the damping ratio. The values used for the variables are given in later sections for each case. The complex frequency variable is denoted by s.

$$LP(s) = \frac{V_{LP}}{V_x} = \frac{\omega_{LP}^2}{s^2 + 2\xi_{LP}\omega_{LP} + \omega_{LP}^2}(Volt/Volt) \tag{C.2}$$

The PID (Proportional-Integral-Derivative) controller is a very common algorithm for AMBs and dynamic systems in general. It is powerful in that the speed of response,

damping, overshoot, and steady-state error characteristics are easily modified by the filter variables. A continuous form of the PID model was used, although the actual controller is digital. A digital approximation could be applied to the system, but was not performed in the previous work. Equation (C.3) gives the form of the control transfer function. The variables used are K_P, the proportional gain, K_D, the derivative gain, K_I, the integral gain, and K_T, the overall gain. These gains are user-adjustable and the values used for each test are given in later sections.

$$PID(s) = \frac{V_{PID}}{V_{LP}} = \frac{K_T\left(K_D s^2 + K_P s + K_I\right)}{s}\left(Volt/Volt\right) \tag{C.3}$$

The power amplifiers used in the MB350 are switching amplifiers operating at a frequency of 20 kHz. They were modeled as Butterworth low pass filters, the form of which is given by Equation (C.4). The filter cutoff value, ω_A, was taken to be the switching frequency and the filter gain, K_A, was experimentally determined to be 760.

$$AMP(s) = \frac{I}{V_{PID}} = K_A \frac{\omega_A^2}{s^2 + \sqrt{2}\omega_A s + \omega_A^2}\left(Amp/Volt\right) \tag{C.4}$$

By combining these five transfer functions the system transfer function can be approximated. For a more complete derivation and the experimental validation of this model, see Clements (2000).

C.2 Experimental Controller Transfer Functions

Because of the different rotor configurations and load types used in the experimental testing, different controller settings were required. The first test was static and used only the 1-3 AMB. The settings used for this test are given in Table C.1. The 2-4 bearing was completely disabled for this test.

Table C.1: Controller settings for initial static testing (1-3 bearing only)

Parameter	Value
Proportional Gain	90.0
Integral Gain	100.0
Derivative Gain	0.1
Total Gain	0.0008
Low Pass Breakpoint	1500 Hz
Low Pass Damping	0.707

Using Clements's model, the transfer function for this system is given by Equation (C.5).

$$\frac{I_c(s)}{X(s)} = \frac{2.779e20s^2 + 2.501e23s + 2.779e23}{s^5 + 1.91e5s^4 + 1.825e10s^3 + 2.262e14s^2 + 1.403e18s} \tag{C.5}$$

For the second static tests, the shaft was fully levitated with the AMBs, which employed both bearings. The controller gains were modified to provide the desired performance. Table C.2 gives the controller settings used for this configuration. The resulting controller transfer function is given by Equation (C.6).

Table C.2: Controller settings for secondary static testing (both bearings)

Parameter	Value
Proportional Gain	90.0
Integral Gain	100.0
Derivative Gain	0.08
Total Gain	0.0008
Low Pass Breakpoint	1500 Hz
Low Pass Damping	0.707

$$\frac{I_c(s)}{X(s)} = \frac{2.223e20s^2 + 2.501e23s + 2.779e23}{s^5 + 1.91e5s^4 + 1.825e10s^3 + 2.262e14s^2 + 1.403e18s} \tag{C.6}$$

Since the bearings were now supporting a rotating shaft, both were used and the control gains were modified to better handle this scenario. The new settings were applied to both bearings and are given in Table C.3. Equation (C.7) gives the new open-loop controller transfer function.

Table C.3: Controller settings for dynamic testing

Parameter	Value
Proportional Gain	90.0
Integral Gain	100.0
Derivative Gain	0.07
Total Gain	0.0009
Low Pass Breakpoint	1500 Hz
Low Pass Damping	0.707

$$\frac{I_c(s)}{X(s)} = \frac{2.188e20s^2 + 2.814e23s + 3.126e23}{s^5 + 1.91e5s^4 + 1.825e10s^3 + 2.262e14s^2 + 1.403e18s} \qquad \text{(C.7)}$$

Appendix D

Uncertainty Analysis

D.1 Bearing Load Uncertainty

The calculated bearing loads for the two static tests all have some degree of uncertainty associated with them. Depending on how they are calculated, this could be due to uncertainties in length or mass measurements. The equation for calculating the uncertainty in the bearing loads is given by

$$\frac{U_F}{F} = \left(\sum_{i=1}^{n} \left(\frac{U_i}{X_i} \right)^2 \right)^{1/2} \tag{D.1}$$

where U_F/F is the percent uncertainty in the force measurement, U_i are the various measurement uncertainties, X_i are the associated measurements, and n is the number of components in the force equation. As an example, the equation used for calculating the bearing load for static test number 1 is given by

$$F = \frac{F_m r_m}{r_b} \tag{D.2}$$

where F is the calculated bearing load, F_m is the measured force using a load cell, r_m is the distance from the pivot to the measurement point, and r_b is the distance from the pivot to the bearing. The uncertainty for this measurement would be

$$\frac{U_F}{F} = \left(\left(\frac{U_F}{F_m} \right)^2 + \left(\frac{U_r}{r_m} \right)^2 + \left(\frac{-U_r}{r_b} \right)^2 \right)^{1/2} \tag{D.3}$$

where U_F is the uncertainty in the force measurement and U_r is the uncertainty in the distance measurements. The uncertainty in the force measurement was taken as 0.102% from manufacturer's specifications. For the distance measurements, the uncertainty was taken as 1.588 mm (0.0625 in) because a tape measure with 1/16 in graduations was used to take length measurements. With the measured values, Equation (D.3) can be rewritten as

$$\frac{U_F}{F} = \left((0.00102)^2 + \left(\frac{1.588}{330.2} \right)^2 + \left(\frac{-1.588}{266.7} \right)^2 \right)^{1/2} = 0.0077 = 0.77\% \tag{D.4}$$

for load case #4. The percent uncertainties for the various loadings for the first static tests are given in Table D.1.

Table D.1: Static test #1 bearing load uncertainties

Load Case	Bearing Load (N)	% Uncertainty
1	16.73	0.72%
2	26.82	0.70%
3	37.94	0.75%
4	48.49	0.77%

For the second static tests, the rotor was fully supported with AMBs. This eliminates the moment calculations, and the simple rotor weight can be used. Each component was weighed on a mass scale with a resolution of 1g. This gives a resolution of ±0.5g. For the heaviest load case in the second set, the uncertainty equation can be written as

$$\frac{U_F}{F} = \left(\left(\frac{0.5}{7059.5} \right)^2 \right)^{1/2} = 7.08 \cdot 10^{-5} = 0.007\% \tag{D.5}$$

The percent uncertainties for the various loadings for the second static tests are given in Table D.2.

Table D.2: Static test #2 bearing load uncertainties

Load Case	Total Bearing Load (N)	% Uncertainty
1	21.73	0.023%
2	37.69	0.013%
3	53.46	0.009%
4	69.23	0.007%

D.2 Measurement Uncertainty

All experimental measurements contain a certain amount of uncertainty. There are two main categories of measurement error: random precision errors and fixed bias error (ANSI/ASME, 1985). Random precision errors are those that are observed in repeated measurements of fixed quantities. Ideally, the errors will follow a normal, Gaussian distribution, but this assumption must be validated for any test.

For a normal population, the data can be fully described by two parameters. The mean, μ, represents the true population average. The standard deviation, σ, is a measure of the spread of the data. The interval $\mu \pm 2\sigma$ encompasses approximately 95% of the data for a measurement of μ. The experimental measure of the true population average is called $\overline{X}$ and is calculated using Equation (D.6).

$$\overline{X} = \frac{1}{n}\sum_{i=1}^{n} X_i \tag{D.6}$$

where n is the number of measurements, and x_i are the individual measurements. The statistic, S, gives a measure of the spread in the experimental data. It is calculated using Equation (D.7).

$$S = \left(\frac{\sum_{i=1}^{n} \left(X_i - \bar{X} \right)^2}{n-1} \right)^{1/2} \tag{D.7}$$

Bias errors are systematic and do not change during the testing. Since they are constant, non-statistical methods are typically employed to determine the magnitude of the error. Bias errors can be categorized into those that are known and can be eliminated by calibration, those that are known and negligible, and those that can be estimated and included in the uncertainty analysis.

Once the bias and precision errors are determined, they can be combined to arrive at a general uncertainty value that encompasses the experimental error in the measurements. Typically, data is presented with an accompanying interval to account for this uncertainty. Equation (D.8) shows an example of a measurement and uncertainty interval.

$$x \pm U \tag{D.8}$$

The accepted procedure for calculating the uncertainty, U, is to use statistical methods. The equation for a two-tailed uncertainty is given by (D.9).

$$U = \left(B_e^2 + \left(t_s S \right)^2 \right)^{1/2} \tag{D.9}$$

where B_e is the bias error, S is the precision error, and t_s is the 95% value for the two-tailed Student t-distribution.

To determine the uncertainty interval associated with the experimental predictions for the bearing-applied force, Equation (D.9) was used in a simplified form without bias error. Since it is desired to determine the uncertainty of the multi-point method, the standard deviation of the predictions and the Student t-value were used to calculate the

error band. Multiple tests were performed for each test case and this additional data was used to determine the error in the method. Table D.3 summarizes the calculation of the uncertainty values for the multi-point force predictions for static test #1. The force prediction uncertainty values for the two single-point methods are presented in Tables D.4 and D.5.

Table D.3: Uncertainty calculations for multi-point force predictions (static test #1)

Supported Load	n	S	t_s	U
16.73 N (3.76 lbf)	5	0.9762	2.571	2.5097
26.82 N (6.03 lbf)	5	0.7824	2.571	2.0116
37.94 N (8.53 lbf)	5	0.4712	2.571	1.2114
48.49 N (10.90 lbf)	5	0.4744	2.571	1.2196

Table D.4: Uncertainty calculations for corrected single-point force predictions (static test #1)

Supported Load	n	S	t_s	U
16.73 N (3.76 lbf)	5	1.7159	2.571	4.4116
26.82 N (6.03 lbf)	5	2.4584	2.571	6.3205
37.94 N (8.53 lbf)	5	2.8643	2.571	7.3641
48.49 N (10.90 lbf)	5	3.5439	2.571	9.1113

Table D.5: Uncertainty calculations for non-corrected single-point force predictions (static test #1)

Supported Load	n	S	t_s	U
16.73 N (3.76 lbf)	5	0.4021	2.571	1.0337
26.82 N (6.03 lbf)	5	0.6359	2.571	1.6349
37.94 N (8.53 lbf)	5	0.3182	2.571	0.8780
48.49 N (10.90 lbf)	5	0.1988	2.571	0.5112

Tables D.6 and D.7 present the uncertainty results for static test #2. The multi-point uncertainties are given in Table D.6. The single-point force prediction uncertainties are shown in Table D.7.

Table D.6: Uncertainty calculations for multi-point force predictions (static test #2)

Supported Load	n	S	t_s	U
16.73 N (3.76 lbf)	21	0.0453	2.08	0.0943
26.82 N (6.03 lbf)	13	0.1353	2.16	0.2923
37.94 N (8.53 lbf)	17	0.1638	2.11	0.3457
48.49 N (10.90 lbf)	21	0.2967	2.08	0.6172

Table D.7: Uncertainty calculations for single-point force predictions (static test #2)

Supported Load	n	S	t_s	U
16.73 N (3.76 lbf)	5	0.3979	2.571	1.0229
26.82 N (6.03 lbf)	5	0.6881	2.571	1.7690
37.94 N (8.53 lbf)	5	1.5698	2.571	4.0359
48.49 N (10.90 lbf)	4	1.9591	2.776	5.4383

Appendix E

Example Data Summaries

E.1 Static Test #1

Sample Case

X-Value V13-top	Y-Value W13-top	Blank V13-bottom	Blank W13-bottom
Load Case #1, x = -80, i_b = 1.0, 1.1, 1.2, 1.3, 1.4 A			
-6.9662140e+000 1.5236610e+000	-4.4025000e-002 1.5852100e+000	0.0000000e+000 2.0054600e-001	0.0000000e+000 1.5214000e-001
-6.9664860e+000 1.5431770e+000	-4.3988000e-002 1.5984500e+000	0.0000000e+000 2.7897700e-001	0.0000000e+000 2.3717100e-001
-6.9670100e+000 1.5676190e+000	-4.4059000e-002 1.6174810e+000	0.0000000e+000 3.5240000e-001	0.0000000e+000 3.1555300e-001
-6.9670250e+000 1.5957820e+000	-4.4054000e-002 1.6409220e+000	0.0000000e+000 4.2527400e-001	0.0000000e+000 3.9148300e-001
-6.9670970e+000 1.6251950e+000	-4.4035000e-002 1.6673650e+000	0.0000000e+000 4.9165200e-001	0.0000000e+000 4.6372300e-001
Load Case #1, x = -40, i_b = 1.0, 1.1, 1.2, 1.3, 1.4 A			
-6.4462460e+000 1.4391540e+000	-3.9010000e-002 1.4912790e+000	0.0000000e+000 2.8473100e-001	0.0000000e+000 2.4577700e-001
-6.4463980e+000 1.4602200e+000	-3.8957000e-002 1.5070260e+000	0.0000000e+000 3.6295200e-001	0.0000000e+000 3.2819500e-001

-6.4462030e+000	-3.8954000e-002	0.0000000e+000	0.0000000e+000
1.4837910e+000	1.5267080e+000	4.3652400e-001	4.0662200e-001
-6.4465820e+000	-3.8951000e-002	0.0000000e+000	0.0000000e+000
1.5102540e+000	1.5496290e+000	5.0728200e-001	4.8234200e-001
-6.4467900e+000	-3.8963000e-002	0.0000000e+000	0.0000000e+000
1.5386750e+000	1.5755100e+000	5.7770200e-001	5.5523600e-001

Load Case #1, x = 0, i_b = 1.0, 1.1, 1.2, 1.3, 1.4 A

-5.9287700e+000	-3.4489000e-002	0.0000000e+000	0.0000000e+000
1.3503360e+000	1.3913540e+000	3.7270900e-001	3.4429500e-001
-5.9296220e+000	-3.4448000e-002	0.0000000e+000	0.0000000e+000
1.3706430e+000	1.4078140e+000	4.5096900e-001	4.2594100e-001
-5.9299720e+000	-3.4569000e-002	0.0000000e+000	0.0000000e+000
1.3935810e+000	1.4276390e+000	5.2605600e-001	5.0470300e-001
-5.9307040e+000	-3.4510000e-002	0.0000000e+000	0.0000000e+000
1.4192140e+000	1.4508370e+000	5.9852900e-001	5.8064600e-001
-5.9308410e+000	-3.4529000e-002	0.0000000e+000	0.0000000e+000
1.4464170e+000	1.4758720e+000	6.7097900e-001	6.5639700e-001

Load Case #1, x = 40, i_b = 1.0, 1.1, 1.2, 1.3, 1.4 A

-5.4205880e+000	-3.0953000e-002	0.0000000e+000	0.0000000e+000
1.2601700e+000	1.2943270e+000	4.6313400e-001	4.4022700e-001
-5.4204170e+000	-3.0788000e-002	0.0000000e+000	0.0000000e+000
1.2795190e+000	1.3103480e+000	5.4151200e-001	5.2268000e-001
-5.4211150e+000	-3.0949000e-002	0.0000000e+000	0.0000000e+000
1.3021990e+000	1.3302060e+000	6.1729300e-001	6.0240100e-001
-5.4216220e+000	-3.0917000e-002	0.0000000e+000	0.0000000e+000
1.3265260e+000	1.3519250e+000	6.9264700e-001	6.8123600e-001
-5.4217910e+000	-3.0904000e-002	0.0000000e+000	0.0000000e+000
1.3524280e+000	1.3757290e+000	7.6643700e-001	7.5883100e-001

Load Case #1, x = 80, i_b = 1.0, 1.1, 1.2, 1.3, 1.4 A

-4.9241230e+000	-2.8080000e-002	0.0000000e+000	0.0000000e+000

1.1671830e+000	1.1913460e+000	5.5434200e-001	5.4123300e-001
-4.9251450e+000	-2.8102000e-002	0.0000000e+000	0.0000000e+000
1.1860080e+000	1.2075460e+000	6.3399100e-001	6.2453400e-001
-4.9257620e+000	-2.8170000e-002	0.0000000e+000	0.0000000e+000
1.2078570e+000	1.2266150e+000	7.1248600e-001	7.0723600e-001
-4.9263570e+000	-2.8100000e-002	0.0000000e+000	0.0000000e+000
1.2308170e+000	1.2473540e+000	7.8876800e-001	7.8789800e-001
-4.9270410e+000	-2.8182000e-002	0.0000000e+000	0.0000000e+000
1.2547870e+000	1.2700520e+000	8.6299500e-001	8.6637900e-001

E.2 Static Test #2

Sample Case

X-Value	Y-Value	Blank	Blank
V13-top	W13-top	V13-bottom	W13-bottom
V24-top	W24-top	V24-bottom	W24-bottom

Load Case #1, x = -100, i_b = 1.0, 1.5, 2.0 A

-7.1801990e-001	-1.0367780e+000	0.0000000e+000	0.0000000e+000
1.3862866e+000	1.4888324e+000	3.4911926e-001	2.4081787e-001
1.4599093e+000	1.4228971e+000	2.6845850e-001	2.7469592e-001
-7.1412561e-001	-1.0400216e+000	0.0000000e+000	0.0000000e+000
1.5870769e+000	1.6806783e+000	6.4501453e-001	5.4728967e-001
1.6723483e+000	1.6159030e+000	5.5086914e-001	5.8136768e-001
-7.1036914e-001	-1.0518070e+000	0.0000000e+000	0.0000000e+000
1.8243983e+000	1.9228021e+000	9.0800867e-001	8.0772559e-001
1.9321855e+000	1.8562694e+000	7.9559070e-001	8.4305188e-001

Load Case #1, x = -50, i_b = 1.0, 1.5, 2.0 A

-7.2753625e-001	-4.7996130e-001	0.0000000e+000	0.0000000e+000
1.2931913e+000	1.3896024e+000	4.4107947e-001	3.4041663e-001
1.3681807e+000	1.3234414e+000	3.6045837e-001	3.7564124e-001
-7.2649048e-001	-4.8233679e-001	0.0000000e+000	0.0000000e+000
1.4779120e+000	1.5686664e+000	7.5408118e-001	6.6075476e-001
1.5651913e+000	1.4999751e+000	6.5972681e-001	6.9804407e-001

-7.2620605e-001	-4.9381592e-001	0.0000000e+000	0.0000000e+000
1.6948989e+000	1.7912417e+000	1.0372372e+000	9.4041418e-001
1.8021923e+000	1.7167780e+000	9.2620142e-001	9.8362708e-001

Load Case #1, x = 00, i_b = 1.0, 1.5, 2.0 A

-7.4670129e-001	8.0290161e-002	0.0000000e+000	0.0000000e+000
1.1975942e+000	1.2856981e+000	5.3629980e-001	4.4377966e-001
1.2702378e+000	1.2198845e+000	4.5854443e-001	4.8035876e-001
-7.4637158e-001	7.2993042e-002	0.0000000e+000	0.0000000e+000
1.3668752e+000	1.4516466e+000	8.6574744e-001	7.8025415e-001
1.4519727e+000	1.3823317e+000	7.7599841e-001	8.1776013e-001
-7.4649377e-001	6.4598511e-002	0.0000000e+000	0.0000000e+000
1.5616866e+000	1.6509133e+000	1.1692312e+000	1.0811257e+000
1.6654268e+000	1.5751683e+000	1.0629828e+000	1.1254353e+000

Load Case #1, x = 50, i_b = 1.0, 1.5, 2.0 A

-7.7295508e-001	6.1993994e-001	0.0000000e+000	0.0000000e+000
1.0979602e+000	1.1762047e+000	6.3629211e-001	5.5406299e-001
1.1647964e+000	1.1115468e+000	5.6379419e-001	5.8834180e-001
-7.7137537e-001	6.1213538e-001	0.0000000e+000	0.0000000e+000
1.2485284e+000	1.3273586e+000	9.8382800e-001	9.0620532e-001
1.3304106e+000	1.2586937e+000	8.9895105e-001	9.4323059e-001
-7.7047314e-001	6.0702173e-001	0.0000000e+000	0.0000000e+000
1.4223955e+000	1.5045751e+000	1.3069805e+000	1.2263975e+000
1.5222738e+000	1.4296903e+000	1.2053182e+000	1.2693816e+000

Load Case #1, x = 100, i_b = 1.0, 1.5, 2.0 A

-6.8038196e-001	1.0726967e+000	0.0000000e+000	0.0000000e+000
9.7505823e-001	1.0503103e+000	7.5919958e-001	6.8163879e-001
1.0726378e+000	9.9006641e-001	6.5732593e-001	7.1072400e-001
-6.7263611e-001	1.0593138e+000	0.0000000e+000	0.0000000e+000
1.1082974e+000	1.1813314e+000	1.1239305e+000	1.0527277e+000
1.2250436e+000	1.1189900e+000	1.0057336e+000	1.0841702e+000
-6.6785034e-001	1.0529772e+000	0.0000000e+000	0.0000000e+000
1.2610193e+000	1.3368413e+000	1.4679338e+000	1.3937546e+000
1.4008623e+000	1.2671284e+000	1.3259385e+000	1.4309164e+000

E.3 Misalignment Study

Sample Case

X-Value	Y-Value	Blank	Blank
V13-top	W13-top	V13-bottom	W13-bottom
V24-top	W24-top	V24-bottom	W24-bottom

Vertical Test Case, 13Brg = -30, 24Brg = 30, i_b = 1.0, 1.5, 2.0 A

-9.5052271e-001	1.7302222e+000	0.0000000e+000	0.0000000e+000
1.2549048e+000	1.3225626e+000	4.7889050e-001	4.0685547e-001
1.2347896e+000	1.1943950e+000	4.9471399e-001	5.0602563e-001
-9.5003259e-001	1.7220962e+000	0.0000000e+000	0.0000000e+000
1.4331324e+000	1.4919213e+000	8.0041492e-001	7.3969971e-001
1.4112170e+000	1.3534214e+000	8.1744739e-001	8.4782129e-001
-9.4982727e-001	1.7151283e+000	0.0000000e+000	0.0000000e+000
1.6389753e+000	1.6979838e+000	1.0928163e+000	1.0342646e+000
1.6179147e+000	1.5408406e+000	1.1114576e+000	1.1599447e+000

Vertical Test Case, 13Brg = -10, 24Brg = 10, i_b = 1.0, 1.5, 2.0 A

-9.5038025e-001	1.6232363e+000	0.0000000e+000	0.0000000e+000
1.2262701e+000	1.2913676e+000	5.0819385e-001	4.3877783e-001
1.2660896e+000	1.2275591e+000	4.6519348e-001	4.7363770e-001
-9.4963306e-001	1.6166447e+000	0.0000000e+000	0.0000000e+000
1.3957207e+000	1.4531049e+000	8.3782373e-001	7.7897461e-001
1.4493304e+000	1.3932772e+000	7.7896143e-001	8.0682104e-001
-9.5001025e-001	1.6082086e+000	0.0000000e+000	0.0000000e+000
1.5950798e+000	1.6520885e+000	1.1364606e+000	1.0800475e+000
1.6620261e+000	1.5890118e+000	1.0667313e+000	1.1114736e+000

Vertical Test Case, 13Brg = 00, 24Brg = 00, i_b = 1.0, 1.5, 2.0 A

-9.6312439e-001	1.5732490e+000	0.0000000e+000	0.0000000e+000
1.2062566e+000	1.2687548e+000	5.2845764e-001	4.6159619e-001
1.2823225e+000	1.2470908e+000	4.4650452e-001	4.5333289e-001
-9.6010010e-001	1.5674910e+000	0.0000000e+000	0.0000000e+000
1.3767341e+000	1.4312260e+000	8.5626807e-001	8.0059961e-001
1.4656232e+000	1.4132275e+000	7.6180603e-001	7.8584924e-001

-9.5857678e-001	1.5577256e+000	0.0000000e+000	0.0000000e+000
1.5722950e+000	1.6275819e+000	1.1586038e+000	1.1042024e+000
1.6823750e+000	1.6128632e+000	1.0455714e+000	1.0873757e+000

Vertical Test Case, 13Brg = 10, 24Brg = -10, i_b = 1.0, 1.5, 2.0 A

-9.5520081e-001	1.5175127e+000	0.0000000e+000	0.0000000e+000
1.1879177e+000	1.2502804e+000	5.4667334e-001	4.7985144e-001
1.3002576e+000	1.2671433e+000	4.2814612e-001	4.3311475e-001
-9.5527185e-001	1.5107607e+000	0.0000000e+000	0.0000000e+000
1.3571732e+000	1.4121042e+000	8.7590686e-001	8.2008118e-001
1.4852856e+000	1.4341001e+000	7.4195288e-001	7.6508276e-001
-9.5428967e-001	1.5017004e+000	0.0000000e+000	0.0000000e+000
1.5499581e+000	1.6047711e+000	1.1810905e+000	1.1271664e+000
1.7056045e+000	1.6368406e+000	1.0229215e+000	1.0633422e+000

Vertical Test Case, 13Brg = 30, 24Brg = -30, i_b = 1.0, 1.5, 2.0 A

-9.4930444e-001	1.4033495e+000	0.0000000e+000	0.0000000e+000
1.1549398e+000	1.2144203e+000	5.7984229e-001	5.1606177e-001
1.3336732e+000	1.3025631e+000	3.9522449e-001	3.9727075e-001
-9.4793970e-001	1.3969335e+000	0.0000000e+000	0.0000000e+000
1.3188109e+000	1.3717318e+000	9.1431433e-001	8.6122632e-001
1.5243885e+000	1.4756520e+000	7.0351160e-001	7.2435962e-001
-9.4757495e-001	1.3893608e+000	0.0000000e+000	0.0000000e+000
1.5051379e+000	1.5577407e+000	1.2260267e+000	1.1740383e+000
1.7509341e+000	1.6851323e+000	9.7746436e-001	1.0149515e+000

Vita

Jeremy T. Marshall was born on September 27, 1977 in Greensboro, North Carolina and was raised in Liberty, North Carolina. He graduated from Eastern Randolph High School in May 1995 and enrolled at North Carolina State University. While obtaining his undergraduate degree, he performed two internships with Pratt & Whitney. He was a member of the Military Engines High Compressor Group in West Palm Beach, Florida, as well as the Large Commercial Engine Externals Group in East Hartford, Connecticut. In May 1999, he graduated Summa Cum Laude in Mechanical Engineering. He came to Virginia Polytechnic Institute and State University in August 1999 to pursue a Master of Science degree in Mechanical Engineering. He presented a paper summarizing his research at the 2001 ASME IGTI conference held in New Orleans, Louisiana. He defended his Master's thesis on May 8, 2001, completing his graduate education with a 4.0 GPA. He will return to Pratt & Whitney to begin his post-graduate career.